Field Quality Change of Superconducting Accelerator Magnets Due to Re-Magnetization of Superconductor

SUGITA Kei

DOCTOR OF PHILOSOPHY

Department of Accelerator Science
School of Mathematical and Physical Science
The Graduate University for Advanced Studies

2004

Synopsis

Superconducting accelerator magnets are fundamental components of high-energy particle accelerators. Very high field quality and stability of the magnets are required in order to operate an accelerator to minimize beam instability and beam loss. Particularly, time-varying magnetic field quality during a period of a beam injection is an important subject to be understood. A possible reason of the time-varying magnetic field is a change of superconductor magnetizations due to local magnetic field change induced by redistribution of imbalance current in superconducting cables. In order to clarify and to evaluate the mechanism, experimental studies and their evaluations with simulations were performed.

Magnetic field measurements of the superconducting quadrupole magnets (MQXAs) developed by the KEK for the CERN/LHC interaction regions were carried out. The measurements at the beam injection current were performed with a set of rotating harmonic coils after pre-excitation of the magnet. The periodic patterns of the magnetic field along the magnet axis, of which pattern length is equal to the twist pitch of the superconducting cable, was observed. The amplitude of the periodic pattern was decreased with time. The average magnetic field over the periodic patterns corresponding to the effective field quality was also changed with time. It was thought that the decrease of the amplitude is caused by equalization of imbalance currents in the cables, and the change of the average is caused by re-magnetization of superconducting filament. From the measurements of eighteen magnets, it was clarified that the behaviors of the amplitude and the average indicate strong dependences on the pre-excitation.

A change of superconductor magnetization due to an external field change was experimentally evaluated. With a Vibrating Sample Magnetometer (VSM), the magnetization of superconductor used in the MQXAs was measured. The behavior of re-magnetization of superconductor filament induced by external magnetic field with arbitrary direction was clarified.

In order to evaluate the mechanism of time-varying magnetic field, simulation codes were developed. At first, a numerical model of superconductor re-magnetization was developed. In this model, persistent current was assigned as “nested cosine theta” current distribution in coaxial shells in which a superconductor filament is divided. Magnetization behavior calculated with the “nested cosine theta model” indicated good agreement with the results measured with the VSM. As the next step, a numerical model of imbalance currents in a cable was developed. The imbalance currents were ascribed as zigzag currents given randomly. The amplitude of a periodic magnetic pattern induced

by the zigzag currents was evaluated by means of the Monte Carlo method. To reproduce the measured periodic pattern amplitudes, current imbalance with a level of 100 A was required in calculation.

A three-dimensional full coil model based on the MQXA was developed as extension of the above codes. Imbalance currents in cables were assigned as the zigzag current models on each cable position of MQXA. The magnetic field in the magnet bore induced by the zigzag currents was computed, and a sinusoidal field pattern along the longitudinal axis was given. The local magnetic field at the strand in the coils was also computed. Magnetizations of the superconductor filaments in the coils were computed with the "nested cosine theta model", in which the local magnetic field was taken into account. Finally, the magnetic field in the bore induced by each magnetization of the superconductor filaments in the coils was calculated. The simulation reproduced the magnetic field change in the magnet bore by assuming the change of the zigzag currents required to induce the periodic pattern consistent with measurement results. It has been understood that re-magnetization due to the local magnetic field change induced by imbalance current equalization causes the time-varying magnetic field during a period of the beam injection in an accelerator operation.

In conclusion, the field measurements of the magnets showed the strong dependencies of the periodic pattern amplitude and that of average on the pre-excitation history. The "nested cosine theta model" for a superconductor magnetization was developed, and the computation results agreed with the VSM measurements. The simulation for the imbalance currents in the cables has shown the periodic pattern similar to that observed in the measurements. The consequence of three-dimensional simulation is in consistent with with the results of the magnetic field measurements. It has been understood by the experiments and the simulations that the superconductor re-magnetization owing to the equalization of the imbalance currents is origin of field quality change of superconducting accelerator magnets during beam injection.

Contents

Chapter 1

Introduction

High energy physics experiments requires very high energy particles. For the high energy frontiers, accelerators to produce high energy particles with sufficient intensity have been developed. Superconducting magnets providing the high magnetic field that needed for the accelerator are very important fundamental components. In order to minimize beam instability and beam loss, the very high quality and stability of the magnetic field are required for the magnets. The field quality change has been observed, however, during beam injection period in which the magnet is excited by a constant current. This thesis presents the experimental studies and their analyses with numerical simulations in order to clarify the mechanism of the field quality change.

1.1 Superconducting accelerator magnets

Why superconducting accelerator magnets are essentially important in high energy particle accelerators? The superconducting magnets can produce very high magnetic field beyond 2 T of the iron saturation, because the magnetic field can be generated by high density current in superconductor within the critical surface, which is determined by three critical values of temperature, magnetic field and current density as shown in Fig. 1.1. The magnet has to be designed to keep superconducting state, e.g. in case of the CERN[1]/LHC[2] main dipole magnet, the magnet operation temperature is 1.9 K and maximum magnetic field is 8 T in a coil.

How does induce very high quality magnetic field? High quality magnetic field is induced by the current flow in superconducting cables of the magnet. In order to

[1]Centre Européen pour la Recherche Nucléaire/European Organization for Nuclear Research, Geneva, Switzerland.

[2]The Large Hadron Collider (LHC) is under construction at CERN for the operation from 2007.

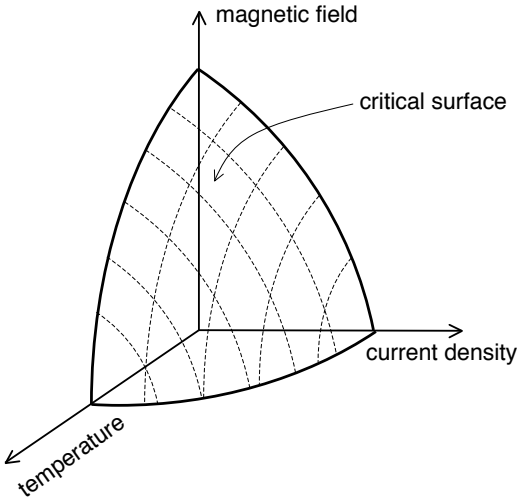

Figure 1.1: Schematic view of a critical surface of superconductor, determined by temperature, current density, and magnetic field. A superconductor is in a superconducting state within the surface.

minimize error of the magnetic field in the bore of the magnet in which high energy particles flow, the cables are arranged to the optimized positions by computations.

The magnetic field in the bore is expanded to multipole fields as follows.

$$\boldsymbol{B} = B_y + i\,B_x = \sum_{n=1}^{\infty}(B_n + i\,A_n)\left(\frac{x+i\,y}{r_0}\right)^{n-1}, \tag{1.1}$$

here r_0 is reference radius of a circle where the magnetic field quality is evaluated. B_n and A_n are normal and skew $2n$-pole components, respectively. Generally multipole fields are evaluated in comparison with the main field of a magnet as

$$\boldsymbol{B} = B_k^{main}\sum_{n=1}^{\infty}(b_n + i\,a_n)\left(\frac{x+i\,y}{r_0}\right)^{n-1} \times 10^{-4}. \tag{1.2}$$

Here B_k^{main} is a main field of a $2k$-pole magnet, e.g. $k = 1$ is dipole, $k = 2$ is quadrupole, b_n and a_n are normal and skew multipole coefficients which are normalized by $B_k^{main} \times 10^{-4}$. Fig. 1.2 shows magnetic field flux lines of normal or skew of dipole or quadrupole.

Figs. 1.3(a) and 1.3(b) show ideal current distribution for pure magnetic dipole field. The superimposed cylindrical currents with the opposite directions induces pure dipole field in the current free region, as shown in Fig. 1.3(a). The cosine theta current distribution in a coaxial cylindrical shell also induces the pure dipole field in the circular current free region[3] , as shown in Fig. 1.3(b). A pure quadrupole field is similarly

[3]Although the both ideal current distribution induces pure dipole field, the current distribution called the cosine theta type should be described as Fig. 1.3(b).

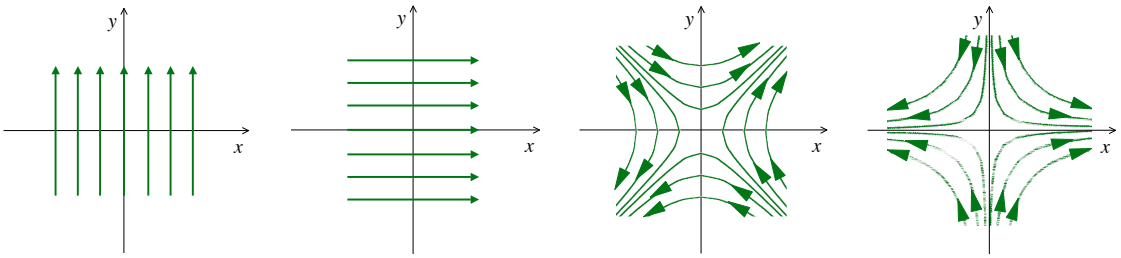

(a) (b) (c) (d)

Figure 1.2: Flux lines of (a) normal, (b) skew dipole fields, and (c) normal, (d) skew quadrupole fields.

induced by cosine two-theta distribution, as shown in Fig. 1.3(c). In reality, a current distribution of practical superconducting accelerator magnets is determined by arrangement of superconducting cables as an approximation of the ideal current distribution.

The quadrupole magnet for the CERN/LHC interaction regions are described as an example of practical superconducting accelerator magnet, of which cross section is shown in Fig. 1.4. An important goal of the LHC is the discovery of the Higgs particle by collision of two protons of 7 TeV. The LHC, of which schematic view is shown in Fig. 1.5(a), is under construction at CERN by international collaboration. The KEK[4] Cryogenics Science Center has responsibility both for the development and the production of the quadrupole magnets for the LHC beam interaction regions, as shown in Fig. 1.5(b).

Initially, to verify the performance of the magnet and to optimize the design, five model magnets of 1 m in length were fabricated and tested at the KEK Cryogenics Science Center since 1996. The last magnet was fabricated by engineers from TOSHIBA Co., in order to the transfer technology and know-how. After that, two full size (6 m long) prototype magnets were fabricated by TOSHIBA and tested at KEK. Slight changes of the design were performed in order to complete its optimization and then the production was started. By summer of 2004, eighteen magnets including two spares have been completed for fabrication and test. The magnets have been shipped to FNAL[5], and will be at CERN after the various tests for the interaction region magnet string at FNAL.

The mechanical structure of the magnet is indicated in Fig. 1.6(a). Four coils are assembled to generate the quadrupole field. The coil having saddle shape ends is wound with superconducting cables. It is so called the Rutherford cable which consists of some tens of twisted strand and is usually used in accelerator magnets, as shown in Fig. 1.6(b).

[4]High Energy Accelerator Research Organization, Tsukuba, Japan.
[5]Fermi National Accelerator Laboratory, Chicago, USA

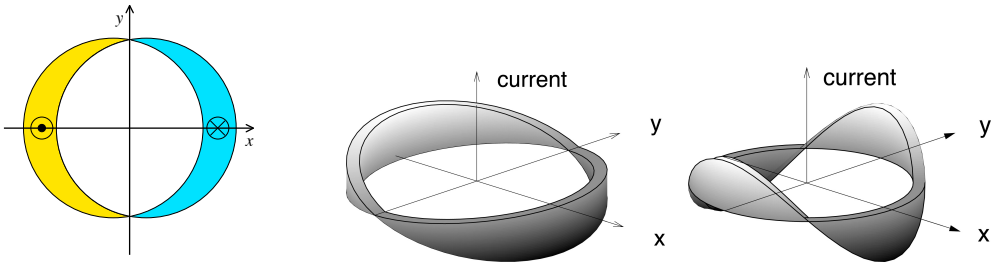

(a) (b) (c)

Figure 1.3: Current distributions for pure dipole magnetic field by (a) superimpose of cylindrical currents, (b) cosine theta, and for pure quadrupole field by (c) cosine two-theta current distribution. The vertical axis of (b) and (C) is relative current density. In the case of (a), the dipole field is induced by the constant density current flow in the crescent region. The current inside the circular shell, of which density distribution is determined by cosine k-theta, induces $2k$-pole field in current free region inside the shell, as shown in (b) and (c).

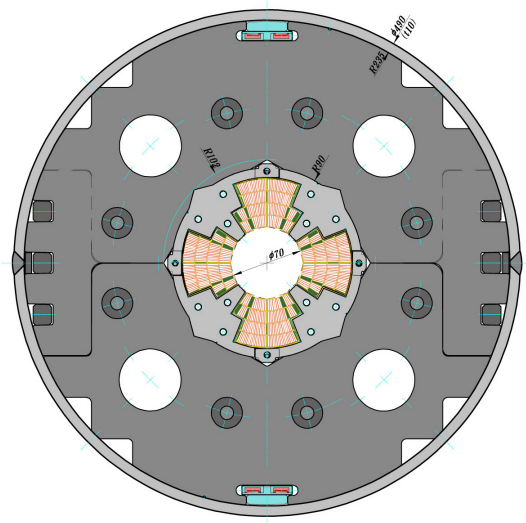

Figure 1.4: Cross section of the quadrupole magnet developed by KEK for the LHC interaction regions.

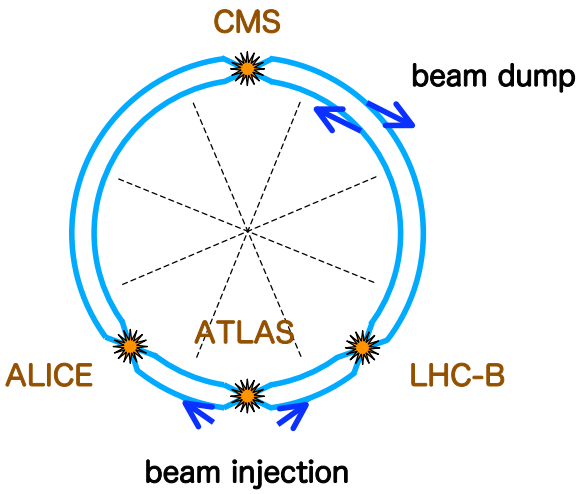

(a)

(b)

Figure 1.5: (a) Schematic view of the CERN/LHC. For final focussing of the counter rotating beam at the four collision points, where the experimental detectors ATLAS, ALICE, CMS, LHCb are installed, superconducting magnets have been developed by KEK and FNAL, respectively. (b) Conceptual arrangement of interaction regions quadrupole magnets. The magnet named as the MQXA have been developed by KEK. The MQXB have been developed by FNAL.

The several thousand superconductor filaments embedded in copper matrix of the strand transport the magnet excitation current, as shown in Fig. 1.6(c). The collars maintain the coil in its fixed designed position. The iron yoke supports the position of collar and coil against the deformation by huge magnetic force and also enhances the magnetic field.

Generally, a superconducting accelerator magnet is excited according to a well defined cycle, as shown in Fig. 1.7. After cool-down to the operational temperature, the magnet is excited before the beam injection, because the magnet at the first excitation behaves differently from successive excitation by the hysteresis of the superconductor. This process is called pre-excitation. After the pre-excitation the current is reduced to below the excitation current of the beam injection period. The current is increased to

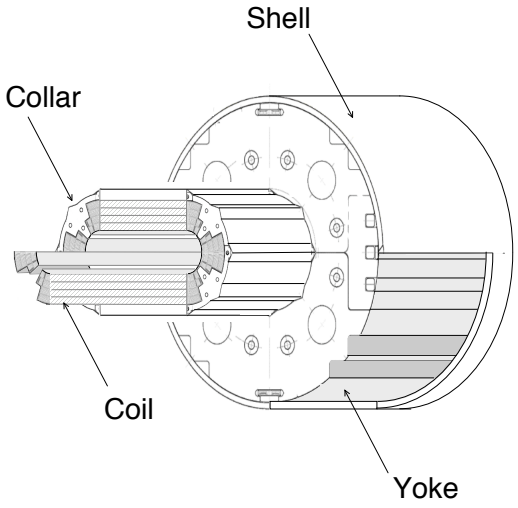

(a)

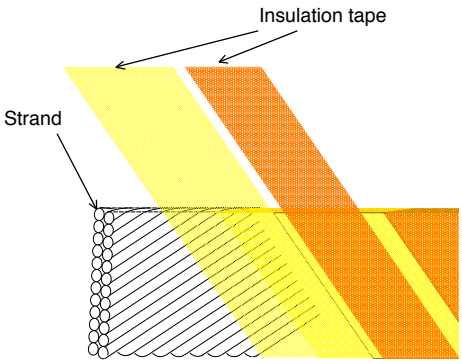

(b)

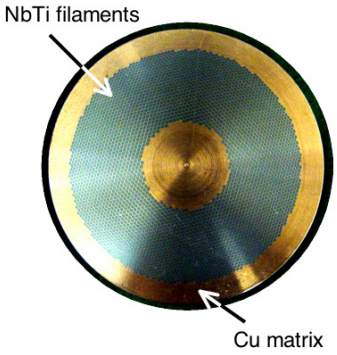

(c)

Figure 1.6: Schematics of the quadrupole magnet for the LHC interaction regions; (a) mechanical structure, (b) superconducting cable with insulation tapes, (c) cross section of the strand.

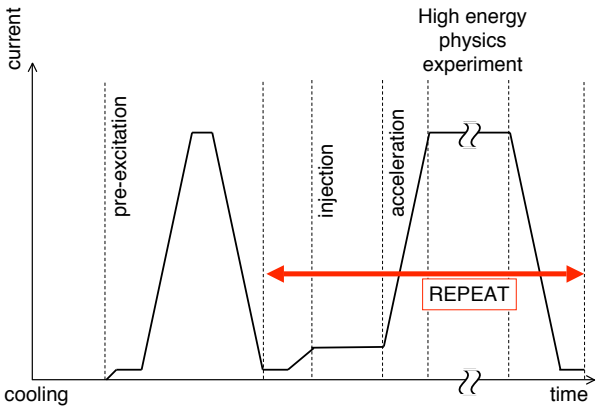

Figure 1.7: Schematic view of the magnet excitation procedure for high energy experiments.

the injection current again. In the beam injection period, it is important to keep the constant magnetic field in order to store low energy particles with keeping the beam stability. After the injection period, particles are accelerated. During the acceleration, the current is increased together with rise of particle energy. The flat top current reaches the value needed for induction of magnetic field corresponding to the required energy for the high energy particle experiment. The high energy physics experiment can then be started. At the end of a run, particles are dumped and the magnet current is reduced down to below the injection current. For the next run, the magnet is excited to induce the magnetic field for injection, and the process is repeated.

1.2 Magnetic field error

1.2.1 Allowed multipole field

Magnetic multipole field is classified into allowed and non-allowed multipole fields, as summarized in Fig. 1.8. If the current distribution of the magnet keeps symmetry of coil arrangement, only the allowed multipole fields may be induced. A dipole magnet with current distribution of $(2k-1)$-fold rotational symmetry, allows dipole, sextupole, decapole, ..., and $2\times(2k-1)$-pole field, except skew components. A quadrupole magnet with current distribution of $2\times(2k-1)$-fold rotational symmetry, allows quadrupole, 12-pole, 20-pole, ..., and $2\times2\times(2k-1)$-pole field without skew components. On the other hand, non-allowed multipole components are induced when the symmetry of the current distribution is broken. The magnetic field errors is classified by the characteristics, as described in the following section. In any case, if the cause of the error has the coil arrangement symmetry, the allowed multipole fields only are induced. In addition, the non-allowed multipole fields observed in measurement is an important information to

search for the cause of the error.

1.2.2 Static magnetic field error

Magnetic field error caused by geometrical distortion is classified as “static magnetic field error”. The error does not change both with excitation current and during accelerator operation.

In a magnet design, optimization of arrangement of conductors and of other parts is performed by a computation code, such as ROXIE[6]. As the next step, research and analysis of the mechanical structure are carried out in order to fix the coils on the designed position, because the forces are introduced in a magnet at accelerator operation by following mechanism.

- Thermal shrinkage
  The parts of a magnet have different thermal shrinkage property. The differences cause forces inside the magnet at the operation temperature.

- Electromagnetic forces
  Superconducting cables of the coils transport the excitation current. Therefore, the Lorentz force arises in the coil by interaction between the current and its own magnetic field.

It is necessary that the stress for the coil fixation remains inside the coils during accelerator operation in order to avoid the coil moving. Therefore, the coils are made slightly larger than quarter-circle cross section in quadrupoles, and are assembled so that the coil is not away from the collars even if it is shrunk by the forces.

However, the parts in a magnet have mechanical size error and slight differences in the physical property. It is important to select the materials which are used in the parts, having very good magnetic/non-magnetic characteristics and their uniformity and stability. In addition the magnet design has to be carried out with consideration of size tolerances.

In mass production, the deviation of the properties correlates to the deviation of multipole fields of the magnets. The deviation of multipole fields due to tolerance error should be random. Therefore, it may be averaged and can be reduced by using many magnets in accelerator. In contrast, if the average of the deviation differs from the design value, the average of the multipole fields by the magnets can not be canceled. The magnetic field errors have to be canceled e.g. by using correction magnets. By analyzing the average multipole components, the cause of the error can be presumed. Correlation between multipole fields and deformations of coils is reported in [1], [2].

[6] “The Routine for the Optimization of magnet X-sections, Inverse field computation and coil End design”, developed at CERN.

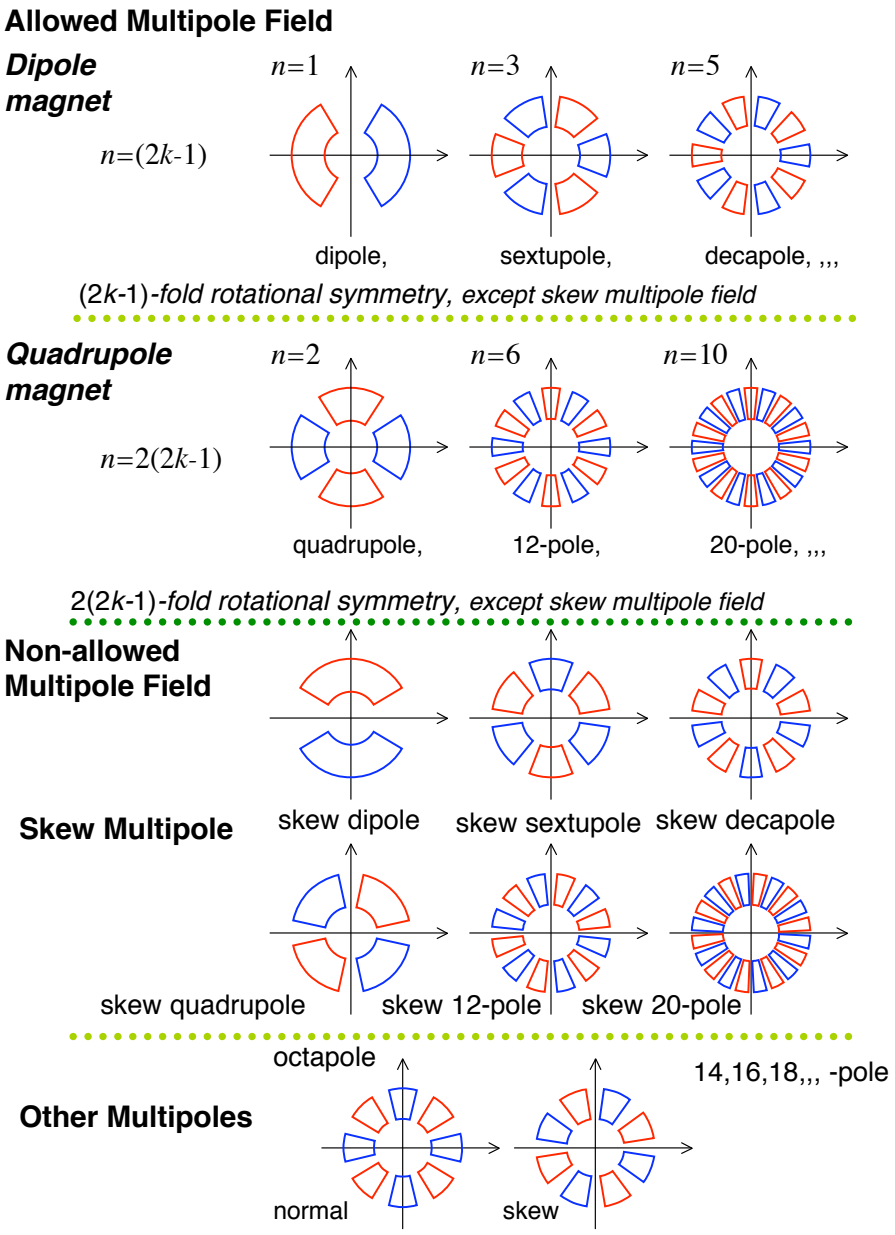

Figure 1.8: Schematic view of allowed and non-allowed multipole fields of dipole and quadrupole magnets. The sector described by the red line indicates the region where current flows from behind to front of paper. The blue one indicates the current flow region with opposite direction.

1.2.3 Dynamic magnetic field error

Current dependent magnetic field error

Magnetic field error which changes with current or time is named “dynamic magnetic field error”. The error magnetic field is induced by magnetization of superconductors in the magnet.

The superconductors in cables of the magnet are magnetized by its own magnetic field. The magnetization of a superconductor is explained by the Bean model. In this model, the shielding current flows with critical current density. Schematic view of shielding current distribution and penetrated magnetic field inside a superconductor with circular cross section is shown in Fig. 1.9. The magnetization curve based on this model is shown in Fig. 1.10. In this calculation, dependence of the critical current density on external magnetic field was taken into account.

The magnetizations distribute symmetrically in the magnet cross section, because the magnetic field in the coils is symmetric, as shown in Fig. 1.11(a). Therefore, only allowed multipole fields arise. The magnetic field due to magnetization can be computed as magnetic field induced by a pair of line currents at filament positions, as shown in Fig. 1.11(b). The multipole field induced by a magnetization $\boldsymbol{M} = (M_x, M_y)$ at (a, φ) is written by

$$B_n = \frac{n\mu_0}{2\pi a^2} \cdot \pi r_f^2 \left[-M_y \cos(n+1)\varphi + M_x \sin(n+1)\varphi \right] \left(\frac{r_0}{a} \right)^{n-1}, \tag{1.3}$$

$$A_n = \frac{n\mu_0}{2\pi a^2} \cdot \pi r_f^2 \left[M_x \cos(n+1)\varphi + M_y \sin(n+1)\varphi \right] \left(\frac{r_0}{a} \right)^{n-1}. \tag{1.4}$$

Here r_f is filament radius, and r_0 is reference radius.

The magnetizations vary with external magnetic field as a function of the excitation current. Therefore, the magnetic field error due to the magnetization changes with the excitation current. The schematics of correlation between a magnet excitation cycle for accelerator operation and magnetic field error is shown in Fig. 1.12.

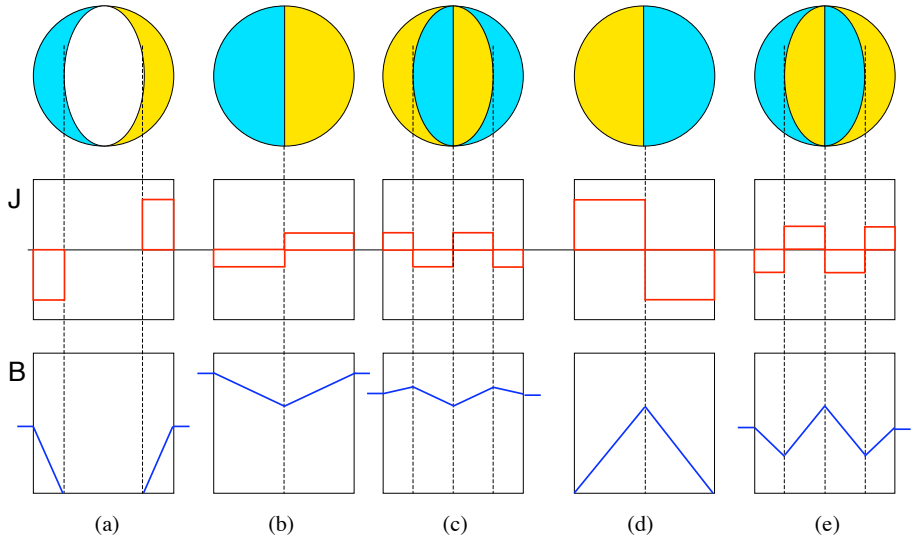

Figure 1.9: Shielding current distribution and penetrated magnetic field in a circular cross section superconductor based on the Bean model.

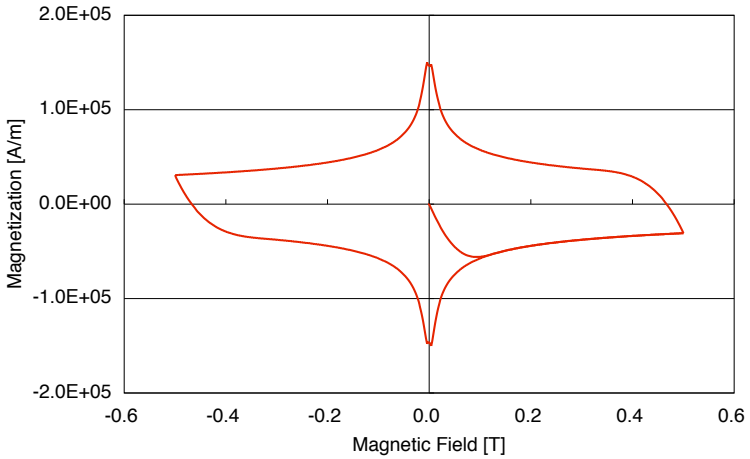

Figure 1.10: Magnetization curve of the circular cross section NbTi superconductor computed by using the bean model. The critical current density of the NbTi is adopted by approximate equation by L. Bottura[3]

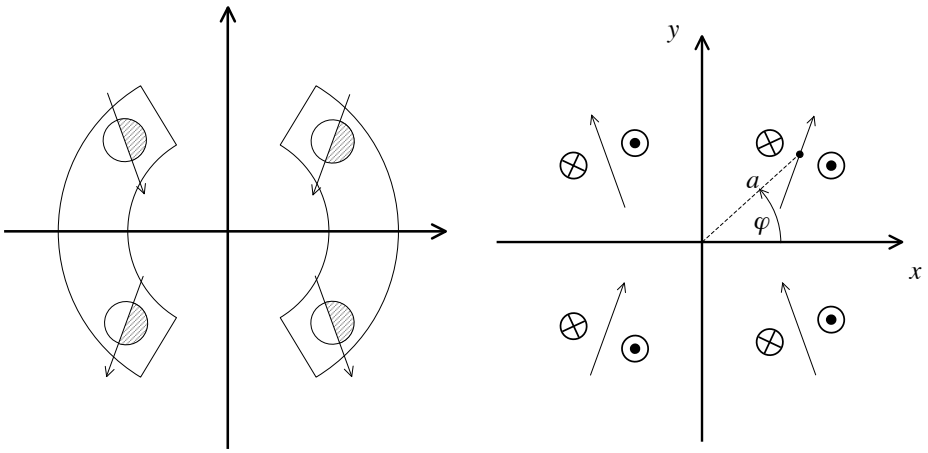

(a) (b)

Figure 1.11: Schematic view of (a) superconductor magnetization in a dipole magnet, and (b) current pairs assigned as the magnetizations.

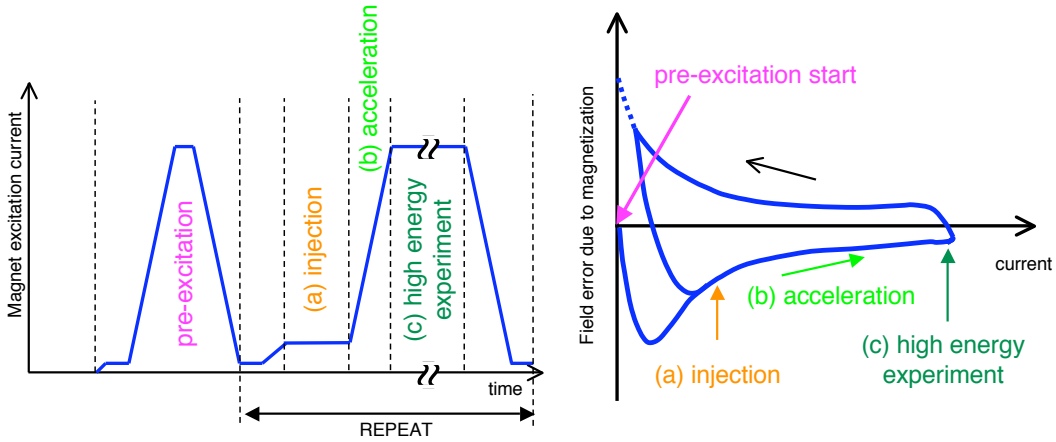

Figure 1.12: Correlation between a magnet excitation cycle and field error due to superconductor magnetization. The graph of "Field error" is corresponding to the right side half of Fig. 1.10. Before the beam injection period, the magnet experiences the pre-excitation cycle. Therefore, the magnetic field error due to the magnetization is positioned at (a) on the hysteresis curve during the injection. In the acceleration period, the magnetic error changes with the excitation current along the hysteresis curve (b). After particle energy reaches to the required energy, the experiments are carried out at (c). At the end of experiment, the particles are dumped and the magnet current is decreased down to below injection current. This process is repeated for each experiment.

Time dependent magnetic field error

A superconductor magnetization decays with time. According to Kim[4] and Anderson[5], the decay is caused by thermal activation of magnetic flux, and has time logarithmic dependence. The time-varying magnetic field error was observed in the superconducting magnet of the Tevatron. The Tevatron was the first accelerator by using superconducting magnets. At the beginning, in the injection phase, particles could not be stored in the accelerator. From the beam profile measurement, a chromaticity change was observed[6].

The chromaticity of beam is influenced by magnetic sextupole field. Fig. 1.13 shows the measured results of time dependent sextupole field at injection field in the Tevatron dipole magnet. It was evident that the chromaticity change was caused by sextupole field change of the superconducting dipole magnet.

The sextupole field is the first component of the error field induced by superconductor magnetizations in a dipole magnet. Therefore, it was thought that the origin of the error is superconductor magnetization decay explained by Kim and Anderson. However, from following experiments, it was obtained that sextupole field exhibits very complicated behavior. Fig. 1.14 shows different behavior of magnetization of cable and magnet for the HERA accelerator. Cable magnetization indicates logarithmic time decay independent of previous magnetic field. On the other hand, the sextupole magnetic field decay depends on pre-excitation, and behaves in a more complicated manner.

In order to understand the time dependent behavior of the sextupole magnetic field, the magnetic field measurements were carried out on various accelerator magnets. The parameters for the various excitation studies are shown in Fig. 1.15.

Summary of the previous studies on Tevatron, HERA, SSC and LHC magnets can be described as follows.

Pre-Excitation Current Dependence

- Larger pre-excitation current induced larger decay at injection.
  Tevatron[9], HERA[8], SSC[10], LHC[11]
- For a large pre-excitation current, strong correlation between b_3 and b_5 was observed in the dipoles.
  LHC[11]

Pre-Excitation Duration Dependence

- Longer pre-excitation flat top induced larger decay at injection.
  Tevatron[12], LHC[11]
- The initial value of multipole fields varied.
  LHC[11]

Dependence of Number of Pre-excitation Cycles

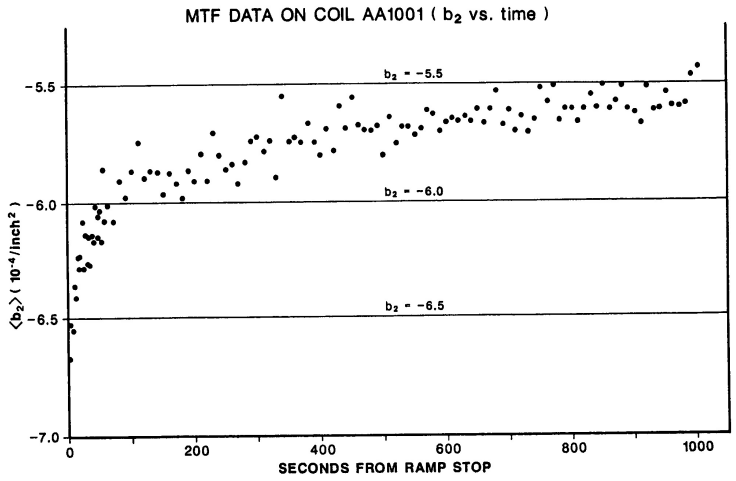

Figure 1.13: Time decay of sextupole field of a test magnet similar to the magnet of Tevatron[6]

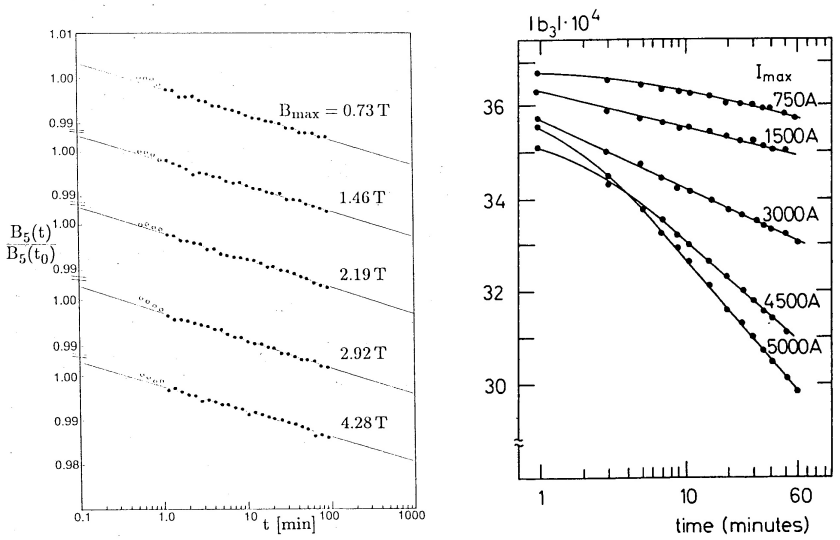

(a) (b)

Figure 1.14: (a) Time dependence of magnetic field induced by the superconducting cable sample used in the HERA dipole magnet[7]. (b) Time dependence of sextupole coefficient of the HERA dipole magnet[8].

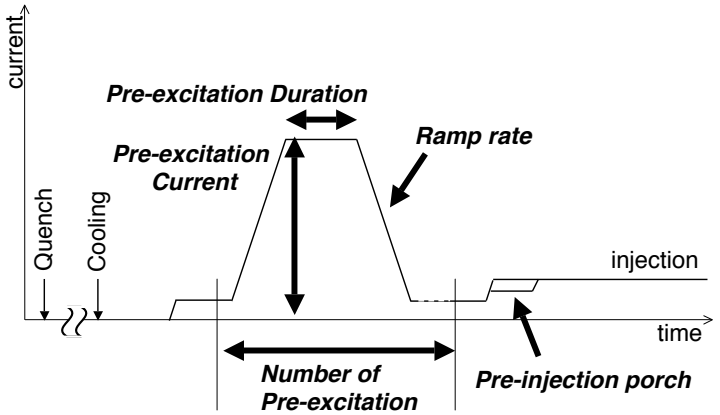

Figure 1.15: Typical parameters of a magnet excitation for study of the field quality change at injection.

– Increase of number of pre-excitations caused larger decay.

Tevatron[12]

– However an intermediate stop at ramp down in the last pre-excitation reduced the time decay rate.

HERA[13]

– Lower flat top current after previous higher flat top current cycle did not influence the decay.

HERA[13]

Influence of Pre-injection Porch

– Amount of current at the pre-injection porch did not affect the time decay. However, the duration of the porch reduced the decay. A longer duration was more effective.

SSC[10], LHC[11]

Influence of Temperature Variation

– Temperature change at injection influenced time decay. In measurement without pre-excitation, the decay stoped at the point of temperature change. However, at injection field after the pre-excitation, the decay did not stop.

SSC[10]

– Increase of temperature caused further decay.

LHC[11]

Others

– Time decay of multipoles in magnets using cables made by different manufactures indicated different behavior.

HERA[13]

– Ramp rate of current to injection influenced the decay. Higher ramp rate caused rapid decay.

Tevatron[12]

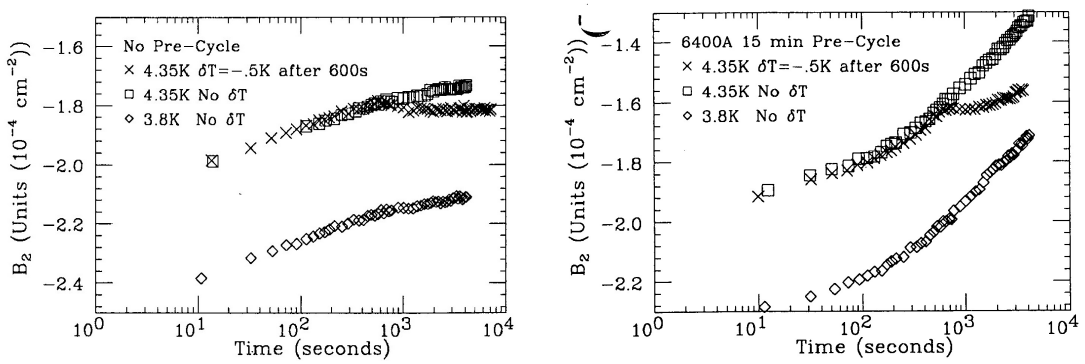

(a) (b)

Figure 1.16: Influence of temperature change on time decay of sextupole component of SSC magnets[10]; (a) without pre-excitation results, (b) with pre-excitation. In the case of (a), the decay stops at point of temperature change. It can be explained as the flux creep effect with temperature dependence. In contrast, the decay does not stop after changing of temperature in the case of (b). These results suggest the existence of another mechanism of the decay except flux creep effect.

From the previous studies, very important information of the cause of time dependent multipole field was obtained. For example, the temperature dependence of sextupole field time decay of the SSC dipole model magnet is shown in Fig. 1.16. The result suggests that another mechanism, which does not depend on temperature.

In addition, when the magnet current is increased after the beam injection period, the sextupole field goes back to its original value rapidly, as shown in Fig. 1.17. The phenomena, so-called “snapback”, is difficult to correct, and is one of the issues for accelerator operation.

Periodic magnetic field pattern

A fluctuation of magnetic field in the bore along the magnet axis was observed in magnetic field measurement of the HERA dipole model magnet at injection field, as shown in Fig. 1.18. The fluctuation is called “periodic magnetic pattern”.

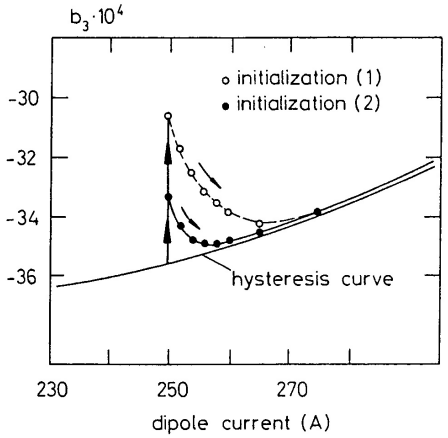

Figure 1.17: Decay and snapback of sextupole coefficient of the HERA dipole magnet with different excitation history[8].

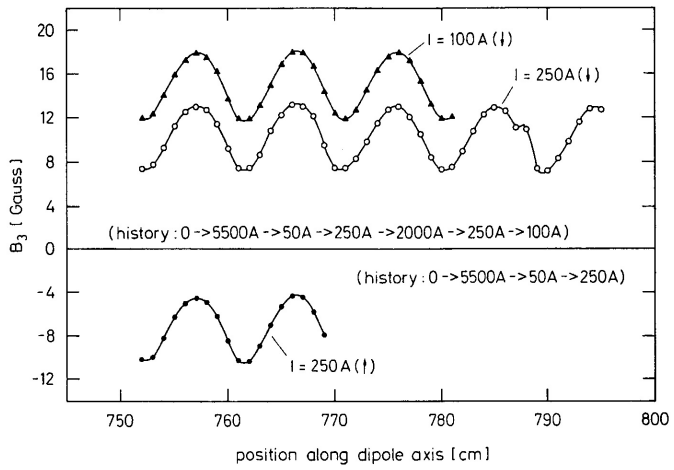

Figure 1.18: Sextupole field along the axis of the HERA dipole model magnet[14].

The periodicity of the pattern is equal to the twist pitch of the superconducting Rutherford cable. From this point, it was thought that the transport current of the magnet flows with imbalance among strands in the cable, and that the fluctuation of magnetic field as superposition of magnetic field due to current imbalance among strands was observed in the magnet bore. This is consistent to observation of the periodic patterns in all the multipole fields.

Periodic patterns were also observed in various accelerator magnets. Generally, a periodic pattern amplitude decreases with time constant of several hours. It may mean that the current imbalance is prone of equalization. Further, the behavior of the periodic pattern amplitude depends on the magnet excitation history, similar to the time decay of multipole fields. The longer or higher pre-excitation current induces larger initial amplitude of periodic pattern. These facts imply that the current imbalance is originated by electromagnetic induction accompanying with magnet excitation and equalizes during several hours under a constant current.

The electromagnetic induction current in superconducting magnets are considered as follows. By excitation of the magnet, the magnetic field also is induced in the magnet parts, namely the coil, collar and yoke. During rump-up of the excitation current, the variation of magnetic field occurs in the magnet, and causes induction currents in the material with conductivity. Especially, induction current through a path of superconductors may have long time constant.

As the path of superconductor, there is an inter-strand or an inter-filament coupling current, as shown in Fig. 1.19. In order to reduce the coupling currents, studies of a contact resistance between strands and of the twist of the strand were carried out, because the coupling currents influence the AC losses during acceleration. Consequently, these induction currents have a time constant of the order of a few milli-seconds.

In contrast, the periodic pattern amplitude decreases with several hours of time constant. Therefore, very long loops with less resistance for induction current are required. A very long loop path was assumed for this induction current such as a loop connected at soldered parts at the ends of a coil. The current is called “Boundary Induced Coupling Current”, as shown in Fig.1.20.

Behavior of the periodic pattern depends on the previous excitation of magnet, similar to time decay of multipole fields. Generally, periodic pattern, after pre-excitation with longer or higher current of flat top, tends to indicate a larger initial amplitude. However, ramp rate of pre-excitation hardly influences the periodic pattern amplitudes. The behavior has been explained by various theoretical and experimental studies of mechanism of the imbalance current. According to the studies, the imbalance currents are induced due to inhomogeneity of magnetic field change (dB/dt), e.g. due to distortion of the twisted cable or soldering at the end part of the coil. The hypothesis is consistent with results of experimental studies with short cables[15].

The imbalance current behavior is summarized in Fig. 1.21. During the current ramp of the first stage of the pre-excitation, the imbalance current is induced by any

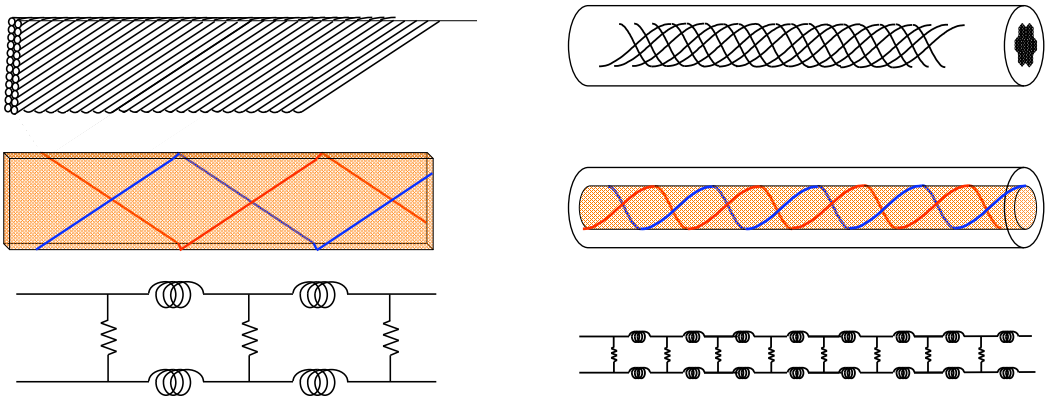

(a) (b)

Figure 1.19: Schematics of (a) inter-strand current, and (b) inter-filament current. Lowest parts indicate equivalent electrical circuit with two strands or with two filaments.

inhomogeneity. After the flat top, during decrease of the current, the imbalance current is reduced, because the dB/dt is opposite sign to ramp up of the current. However, the imbalance current is not completely vanished, because the imbalance current, which is induced during the first ramp-up, decays during the flat top. Therefore, at the beam injection period, only imbalance current, which is not canceled by pre-excitation ramp-up/-down, remains. The qualitative hypothesis can explain the behavior of periodic pattern depends on pre-excitation.

In this thesis, in order to simplify the subject, mechanisms of the induction or the decay of the imbalance current are not treated.

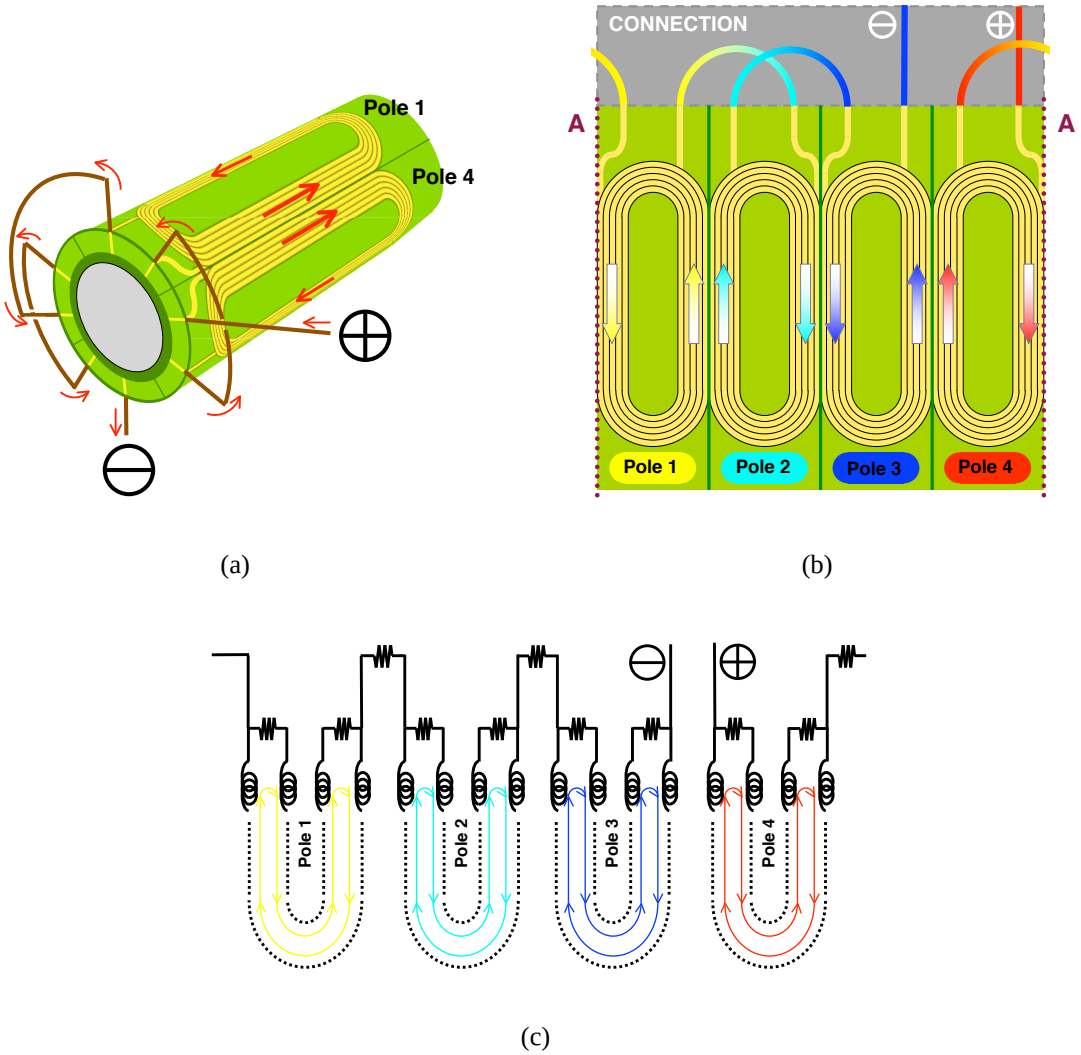

(a) (b)

(c)

Figure 1.20: Schematics of quadrupole magnet coils and their connection; (a) bird's-eye view, (b) development opened up between pole-1 and pole-4, and (c) electric circuit simplified to two strand system. The superconducting cables used in each coil are connected at the ends of coils by means of soldering, typically. The electrical circuit loop closed at the soldering parts having very low resistance less than 1 nΩ, has a very long time constant in comparison with a loop of inter-strand coupling current.

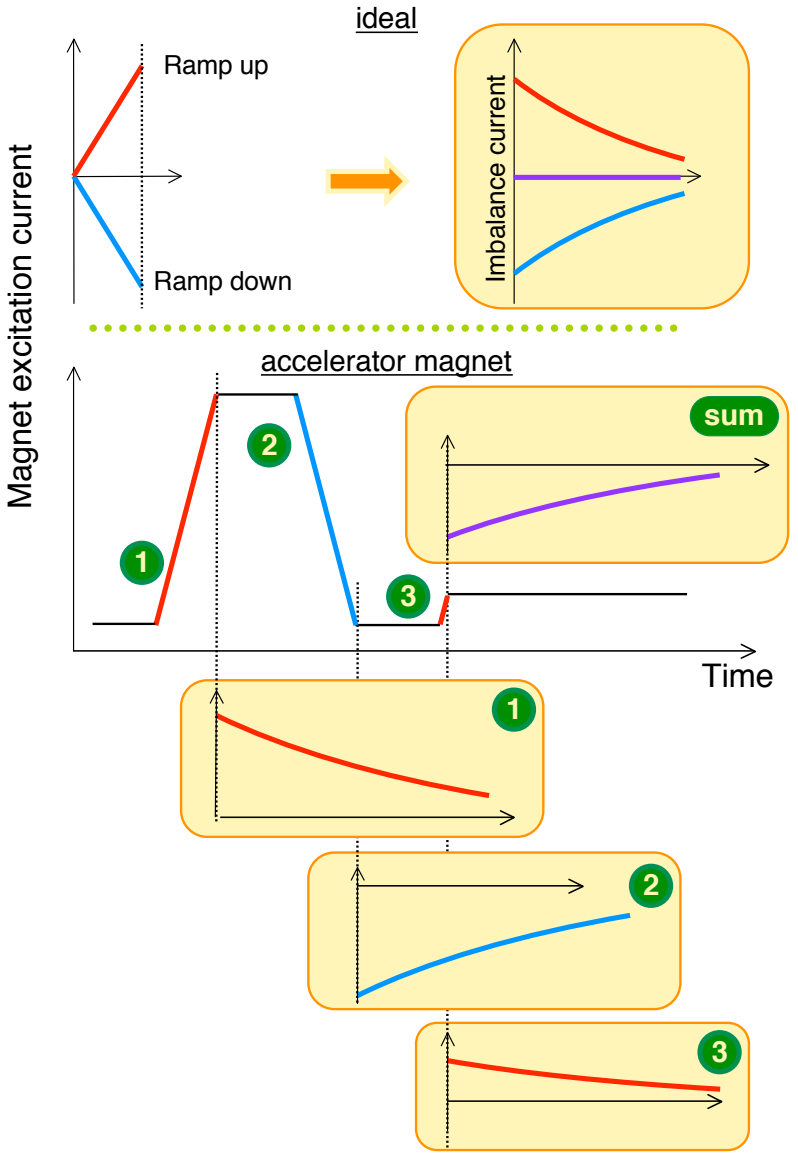

Figure 1.21: Schematics of correlation between magnet excitation and an imbalance current. Ideally, imbalance currents induced by two identical ramps with opposite direction would tend to mutually cancel, as shown in the upper figures. In a practical magnet, imbalance currents induced by ramps are not canceled, because the imbalance currents decay during flat top or other ramps. The number in the schematics are corresponding to the ramp-up/-down and the imbalance current induced by them.

1.3 Scope of the thesis

In the last section, observations of dynamic change both of average multipole field and of periodic magnetic pattern, and the imbalance current suspected as cause of those were described. Since there exists similarity in pre-excitation dependence between dynamic changes, mechanism of multipole field change due to imbalance current, which may be a cause of the periodic magnetic pattern, has been studied. R. Stiening first reported the possibility of magnetization change due to imbalance current change[16]. Further theoretical studies were carried out by R. Wolf[17]. According to the paper, the superconductor magnetization, which is along the magnetic flux line initially, is changed by local magnetic field change due to imbalance current change, as shown in Fig. 1.22.

In summary of the mechanism; Initially, although imbalance currents among the superconducting cable are induced, the direction of superconductor magnetizations is along the magnet's own magnetic flux line. The imbalance currents are equalized with time. Simultaneously, local magnetic field in the coil varies. Due to the local magnetic field change, the magnetization direction is changed, although there is a large background field. Therefore, allowed multipole field induced by magnetization with a regular direction is drifted, and non-allowed multipole is induced.

Fig. 1.23 shows conceptual sketch of the mechanism. In this thesis, the studies performed to cover all the subjects of the sketch are described as follows.

- **Magnetic Field Measurement of Beam Injection Field**
  The magnetic field measurements were carried out on superconducting quadrupole magnets for the LHC interaction regions at injection field. Eighteen magnets with the identical design were measured by means of a rotating harmonic coil set, systematically.

  2-1[7]

- **Measurement of Superconductor Magnetization**
  Magnetization of the superconductor filament in a strand was measured with vibrating sample magnetometer (VSM). The superconductor was exposed in an external magnetic field with arbitrary direction, and its magnetization could be detected.

  2-2

- **Modeling of Superconductor Filament Magnetization**
  A computation code of the superconductor filament magnetization was developed. The model introducing the nested cosine theta current distribution in the coaxial shells dividing filament cross section, represents the magnetization be-

[7]The numbers indicate Chapter-Section corresponding to Fig. 1.23.

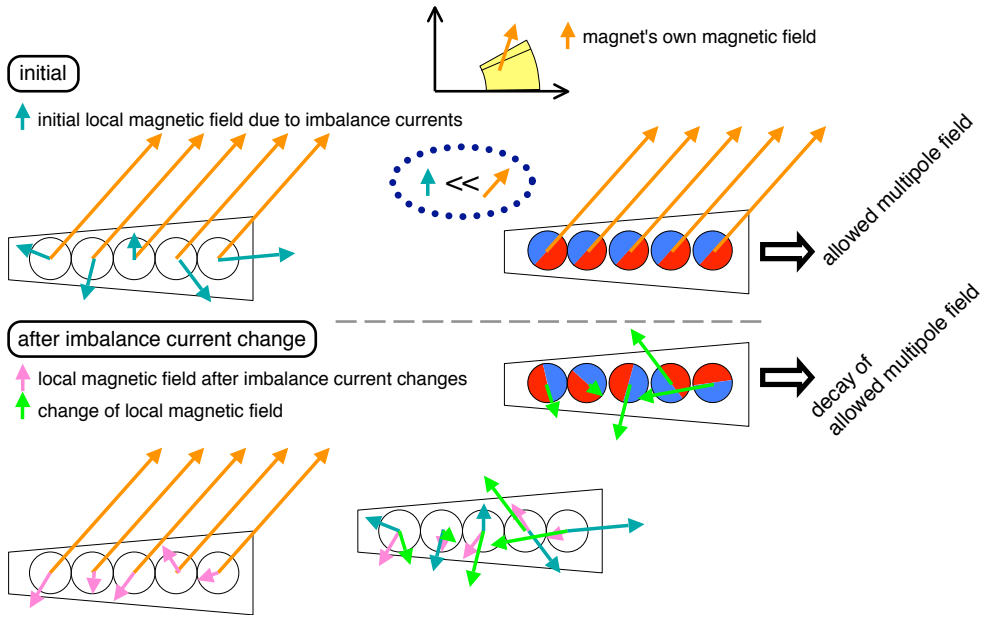

Figure 1.22: Schematics of mechanism of superconductor re-magnetization due to imbalance current change. Initially, superconductor filaments are magnetized along its own magnetic flux lines, although there exist local magnetic field distortions due to imbalance currents. The imbalance current change induces local magnetic field changes. Since the magnetization varies due to amount of magnetic field change even in large background magnetic field, the filament magnetizations are changed by the local field changes.

havior induced by arbitrary angle change of external field.

3-1

- **Modeling of Imbalance Current in Cable**
  The imbalance currents in a cable was estimated which were required to induce the periodic magnetic pattern being consistent to measurement results. The currents were assigned as zigzag currents determined by the Monte Carlo method.

  3-2

- **Simulation of Magnetic Field Error**
  A simulation code for evaluation of the magnetic field error due to remagnetization induced by imbalance current equalization was developed by the combination of the above two codes. In this code, the model is based on the LHC interaction region's quadrupole magnet with four layers coils. Three-dimensional computation and the Monte Carlo method were introduced to the code.

  3-3

Similar studies were carried out by M. Haverkamp[18], [19], [20], [21], [22]. In comparison with his work, this thesis has advance with the subject, e.g. numerical simulations. In this thesis, means of Monte Carlo method and three-dimensional computation are introduced into the simulation codes.

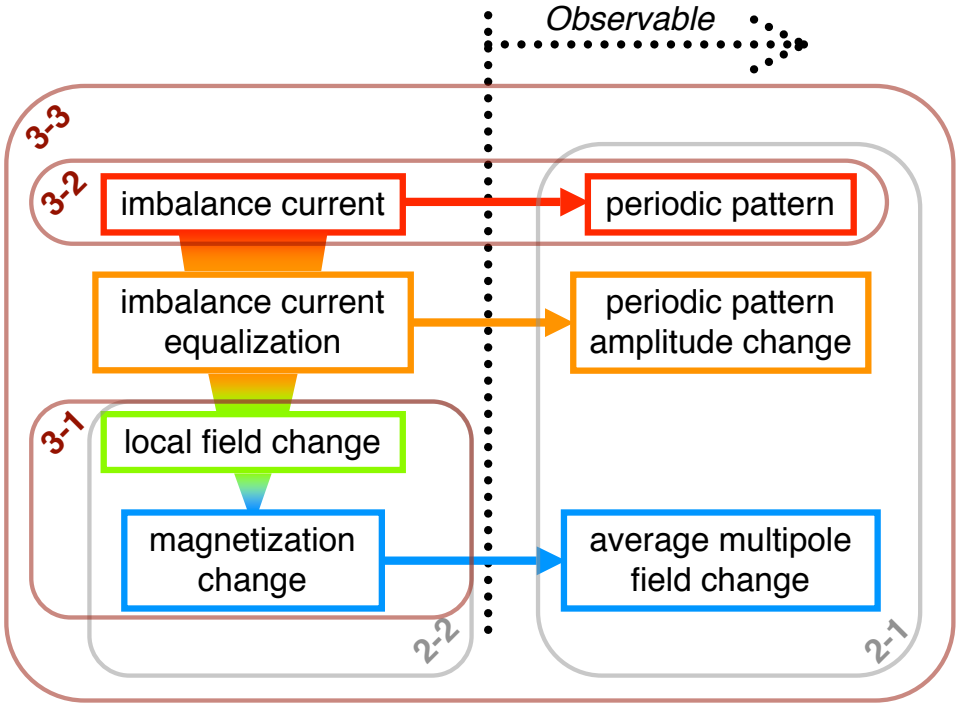

Figure 1.23: Conceptual plan of the mechanism of the time dependent field quality change. Right hand side is observable phenomena. The other side is supposed as mechanism inside the magnets. The frame with number means the Chapter-Section treating the subjects. The frames with the silver/brown line indicate experimental studies/numerical simulations, respectively.

Chapter 2

Experimental Studies of Magnetization in Superconducting Accelerator Magnets

Experimental studies were performed in particular about superconductor magnetization in magnets. At first, magnetic field measurements were carried out in order to confirm the correlation between drift of the average multipole field and behavior of periodic magnetic pattern. The systematic measurements were made on eighteen magnets of identical design to understand the statistical behavior of the magnets. Next, magnetization behavior in the magnets was understood by measurements on superconductors by using a Vibrating Sample Magnetometer (VSM).

2.1 Magnetic field measurement at injection field

2.1.1 Experimental setup

The superconducting quadrupole magnets for the CERN/LHC insertion regions had been developed by the KEK Cryogenics Science Center. The cross section of the magnet is shown in Fig. 2.1. The magnet to be used for final focussing at the beam interaction regions, induces the quadrupole field of 215 T/m in the bore over the magnetic length of 6.63 m. The essential parameters are shown in Table 2.1.

The four layers coils are wound with two types of Rutherford cables, and the parameters of which are shown in Table 2.2. The coils are wound with inner cable from the first to the middle of the second layer. The outer cable is used in remains of second layer, and third, fourth layer. Therefore, inside the each coil, the soldering connection

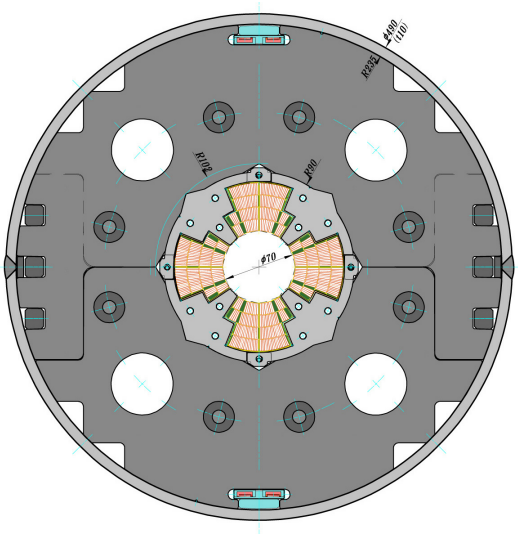

Figure 2.1: Cross sectional view of the superconducting quadrupole magnet for the LHC interaction regions.

Table 2.1: Design Parameters of Quadrupole Magnet for the LHC interaction regions

Field gradient [T/m]	215
Magnet current [A]	7149
Inductance [mH/m]	13.8
Effective magnetic length [m]	6.37
Coil inner radius [mm]	35
Outer radius [mm]	81.3
Stored energy [kJ]	2242

Table 2.2: Design Parameters of Superconducting Cables for the Magnets

	inner cable	outer cable
Width [mm]	11.00	11.00
Mid-thickness [mm]	1.470	1.337
Cable twist pitch [mm]	90	90
Number of strands	27	30
Diameter of strand [mm]	0.815	0.735
Number of filaments	3342	2058
Diameter of filament [μm]	10	10
Cu/NbTi ratio	1.2	1.9
Surface condition	Sn-5%Ag	Sn-5%Ag

exists between inner and outer cable. The coils are connected in series as following order.

current lead $\oplus$
▷ 4th, 3rd ▷ 2nd ► 2nd, 1st (in pole4)
▷ 2nd ► 2nd, 1st ▷ 4th, 3rd (in pole1)
▷ 4th, 3rd ▷ 2nd ► 2nd, 1st (in pole2)
▷ 2nd ► 2nd, 1st ▷ 4th, 3rd (in pole3)
▷ current lead $\ominus$

Here ► indicates the connection inside the coils, and ▷ indicates the connection outside the coils at lead end side. The layer expressed by blue/green letter is wound with inner/outer cable.

After electrical examination, the magnet is excited under the operation temperature of 1.9 K, which is achieved by superfluid helium in a vertical cryostat, as shown in Fig. 2.2.

The magnetic field measurements were performed by using a 25 mm long rotating coil set, which were scanned with 11.25 mm pitch as shown in Fig. 2.3. A measurement at each position takes 40 seconds which include the actual measurement, data transfer, and the movement of the rotating coil. The parameters of the rotating coil set are summarized in Table 2.3. To understand the correlation between periodic patterns and time varying field quality, it is important to measure higher order multipoles by harmonic coil set. Hall probe have been used for similar magnetic field measurement[20],[23], because the probe is suitable for fast measurement because of time resolution of it. However, harmonic coil set has an advantage to measure all the multipole field, because a Hall probe can not measure non-allowed multipole field. This measurement system of harmonic coil sets had been developed by N. Ohuchi. His works on the magnetic

field measurements were reported in [24], [25], [26], [27], [28], [29], [30], [31], [32]. The accuracy of the system is 10^{-6}, therefore, the order of 0.01 unit as magnetic field coefficient is credible.

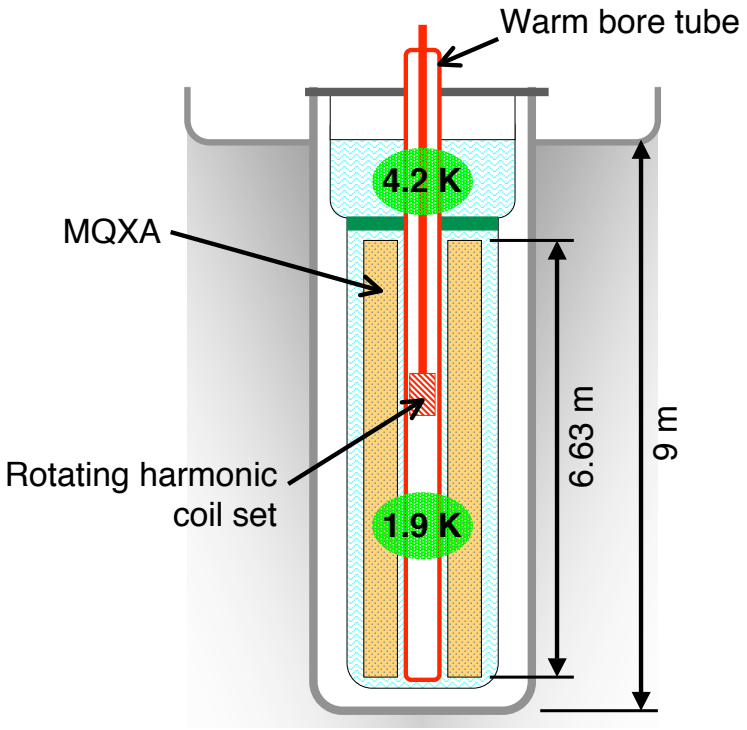

Figure 2.2: Schematic view of MQXA in a vertical cryostat and setting of a rotating harmonic coil set in a warm bore tube inserted into the magnet aperture.

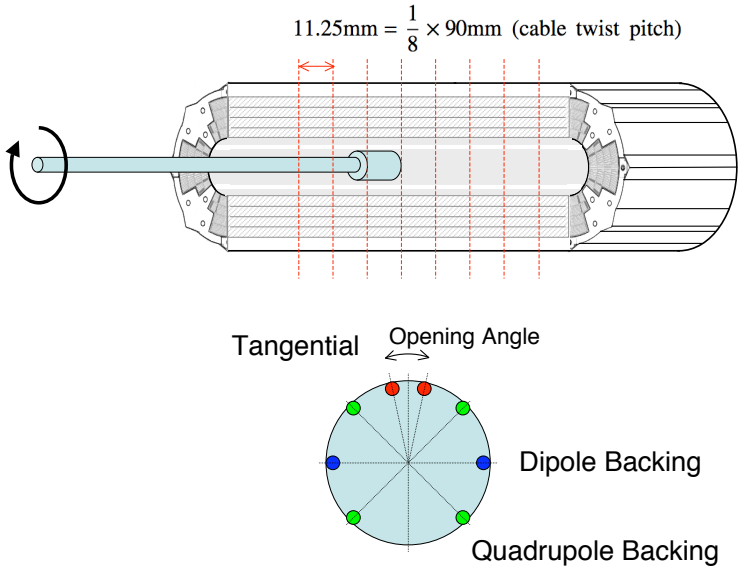

Figure 2.3: Schematic view of the harmonic coil set and the motion of the coil for the periodic pattern measurement.

Table 2.3: Dimensions of the Harmonic Coils

COIL NAME	Length [mm]	Radius [mm]	Opening Angle [degree]	Winding [turn]	Phase [degree]
Tangential	24.3	21	24.294	20	0
Dipole backing 0	25	21	179.686	2	0
Dipole backing 1	25	21	179.686	2	+35
Dipole backing 2	25	21	179.686	2	-35
Quadrupole backing 0	25	21	89.686	2	0
Quadrupole backing 1	25	21	89.686	2	+35
Quadrupole backing 2	25	21	89.686	2	-35

2.1.2 Results

Periodic magnetic pattern behavior

The magnetic field distribution measured along the magnet axis at the injection field after pre-cycling to 7 kA for 1 hour, is shown in Fig. 2.4. The data are a function both of time and of position. The lower horizontal axis indicates the longitudinal distance from the magnet center. The upper horizontal axis indicates the time spent for the measurement. The first measurement starts from a position of -3000 mm and the injection field starts time of 0 second. The second measurement starts again from a position of -3000 mm, but after 40000 seconds from the injection field start time. One scan of the measurement covers almost all the straight section of the magnet. The periodic pattern is observed in entire magnet length. In the first measurement, the periodic pattern amplitude shows the decrease, which is inferred as a decay with time, because a smaller amplitude than that of the first is obtained in the results of the second measurement. A center of the periodic pattern defined as the average over every twist pitch shows a slight distortion over the magnet length. The shape of the distortion appears to be reproducible between the first and the second measurement. Therefore, it is understood that the distortion is due to a geometric deviation of the magnet structure along the magnet axis.

Time behavior of the periodic pattern was measured for a short length at the magnet center. The results after 7 kA and 1 hour pre-excitation are shown in Fig. 2.5. The rotating coil was moved back and forth along the magnet axis for four cable twist pitch lengths. The periodic pattern amplitude decreased within a few hours. However, the amplitude hardly decreased after 4 or 5 hours. The results suggest that the periodic pattern is caused by several current loops of the imbalance current. A few hours of time constant of the periodic pattern amplitude change is consistent with results of the previous studies of time varying magnetic field.

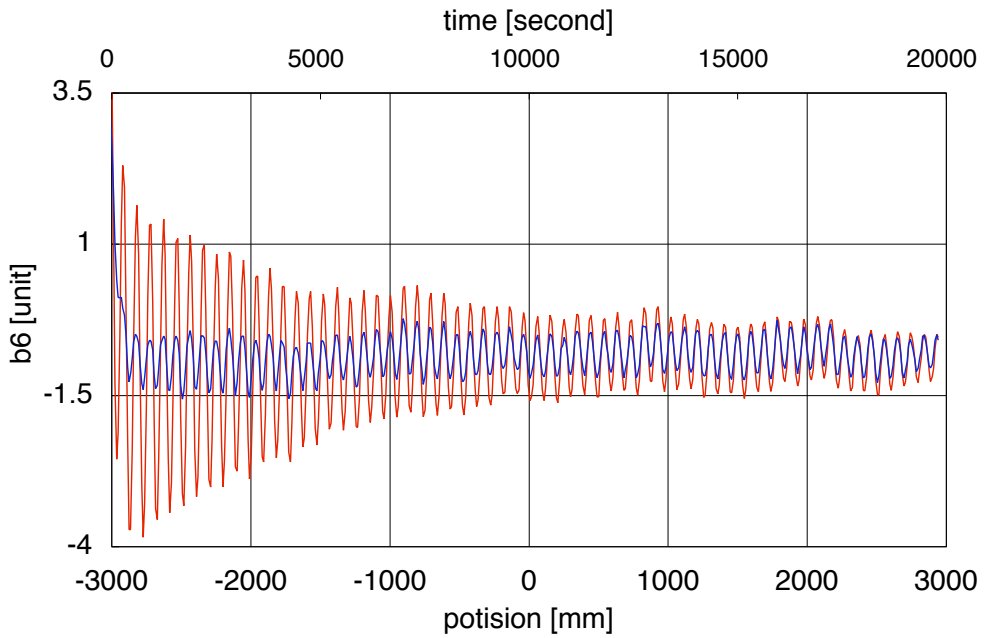

Figure 2.4: Magnetic field distribution in the magnet bore along the magnet axis. The red line is the initially measured results. The blue line is results after 40000 second from the start of the first measurement.

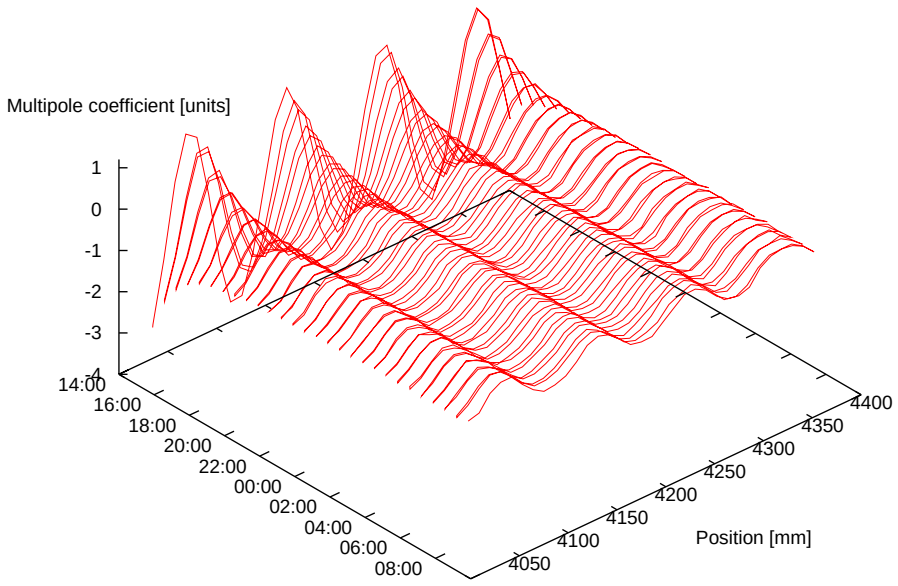

Figure 2.5: Time dependence of the periodic pattern for short length at the magnet center.

Systematic measurements with various pre-excitation

Measurements of pre-excitation effect were performed according to a procedure as seen in Fig. 2.6. At first, to clear the memory of the magnet due to eddy current etc, the magnet was quenched. The "quench" means that all superconductors in the magnet are changed to normal conductivity. After cooling to 1.9 K, the magnet was subjected to the pre-excitation cycle. As shown in Fig. 2.6, the flat top current and duration were changed as parameters for each measurement because behavior of the periodic pattern depends on excitation history. The current was then reduced to 50 A, and was increased to 390 A, which induced the beam injection field corresponding to the LHC operation. After that, a measurement was started. The rotating coil went back and forth for four cable twist pitch length around the center of magnet.

Figs. 2.7 indicate stability of the measurements. The stability of the current during the measurement for four hours measured by the DCCT[1] is shown in Fig 2.7(a). It is necessary to control the current, of which instability influences on magnetic field quality. Fig. 2.7(b) indicates the measured point on time-position plane. The moving system of the harmonic coil set is very well controlled during the measurement. By accurate measurement, the periodic pattern in the magnetic field were obtained, as shown in Fig. 2.8.

The data of function of time and position are sorted by the each their position, and fitted by a polynomial function. From the fitting curve, simultaneous periodic patterns are obtained. The process is shown in Fig 2.9.

Then, the simultaneous periodic patterns at $t = t_0$ are fitted by

$$b_n^{t_0}(z) = b_n^{amp,t_0} \sin\left(\frac{2\pi z}{\lambda} - \delta\right) + b_n^{ave,t_0} + b_n^{lin} \cdot z, \tag{2.1}$$

$$a_n^{t_0}(z) = a_n^{amp,t_0} \sin\left(\frac{2\pi z}{\lambda} - \delta\right) + a_n^{ave,t_0} + a_n^{lin} \cdot z. \tag{2.2}$$

Here t_0 is the time from measurement start, z is the longitudinal position, and b_n^{amp}, a_n^{amp}, λ and δ are the amplitude, the wave length and the phase of the periodic pattern, respectively. b_n^{ave} and a_n^{ave} are the average multipole field. b_n^{lin} and a_n^{lin} are coefficients of the multipole field that depends linearly on position.

The results of the example of the fitting are shown in Fig. 2.10. Figs. 2.10(a) and 2.10(b) indicate the development of the average, b_n^{ave}, and the amplitude of the periodic pattern, b_n^{amp}. The Figs. 2.10(c) are indicate the fitting parameters of b_n^{lin}, the wave length λ, and the phase δ. Generally, the measurement region is so short that the b_n^{lin}, a_n^{lin} are very small, and can be ignored, as shown in the Figure. The typical wave length, which is 95-98 mm, is comparable to the cable twist pitch design (90±10 mm). According to the cable documentation, the average twist pitch of the inner cable is 96-97 mm, and of

[1]Direct Current Current Transformer

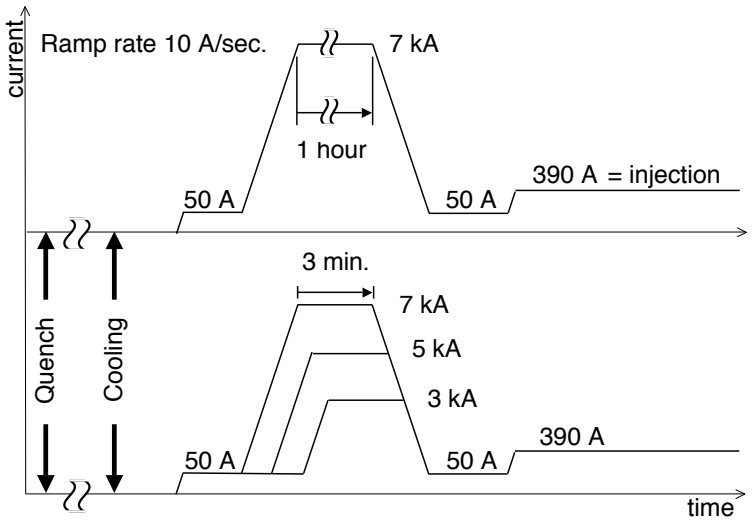

Figure 2.6: Procedure of measurement of flat top current dependence.

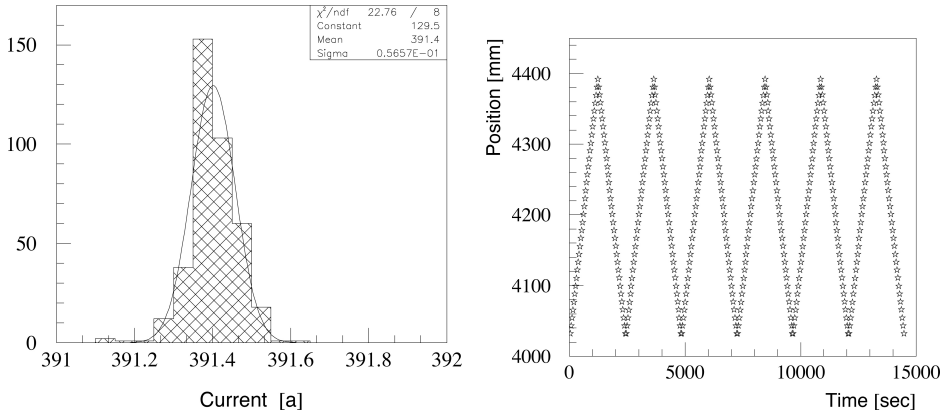

(a) (b)

Figure 2.7: Example of (a) histogram of the excitation current at each point, and (b) time vs. position, during measurement for four hours.

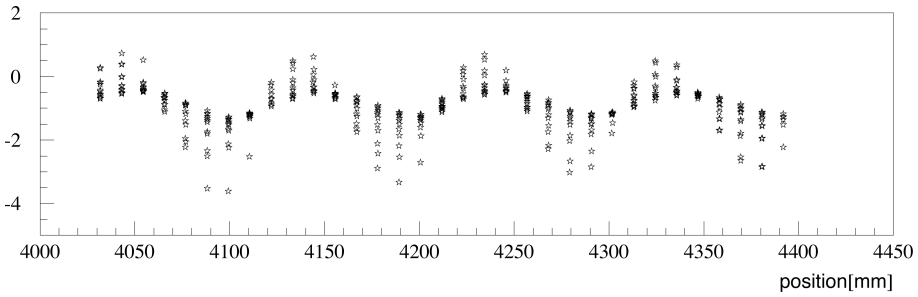

Figure 2.8: Example of measured periodic pattern of b_6. The vertical axis is b_6 coefficient in unit. The data of function of time and position during four hours plotted in the graph with the position axis.

the outer cable is 91-92 mm. From the results, it was verified that imbalance currents of the inner cable are the dominant source of periodic patterns.

The phase is stable especially in the measurement after 3, 5 kA pre-cycling. As extraordinary case, we observed the amplitude growth of the periodic pattern just after pre-cycling of 7 kA 1 hour. The amplitude growth is observed with obligatory phase shift in almost all the multipole fields in same measurement run.

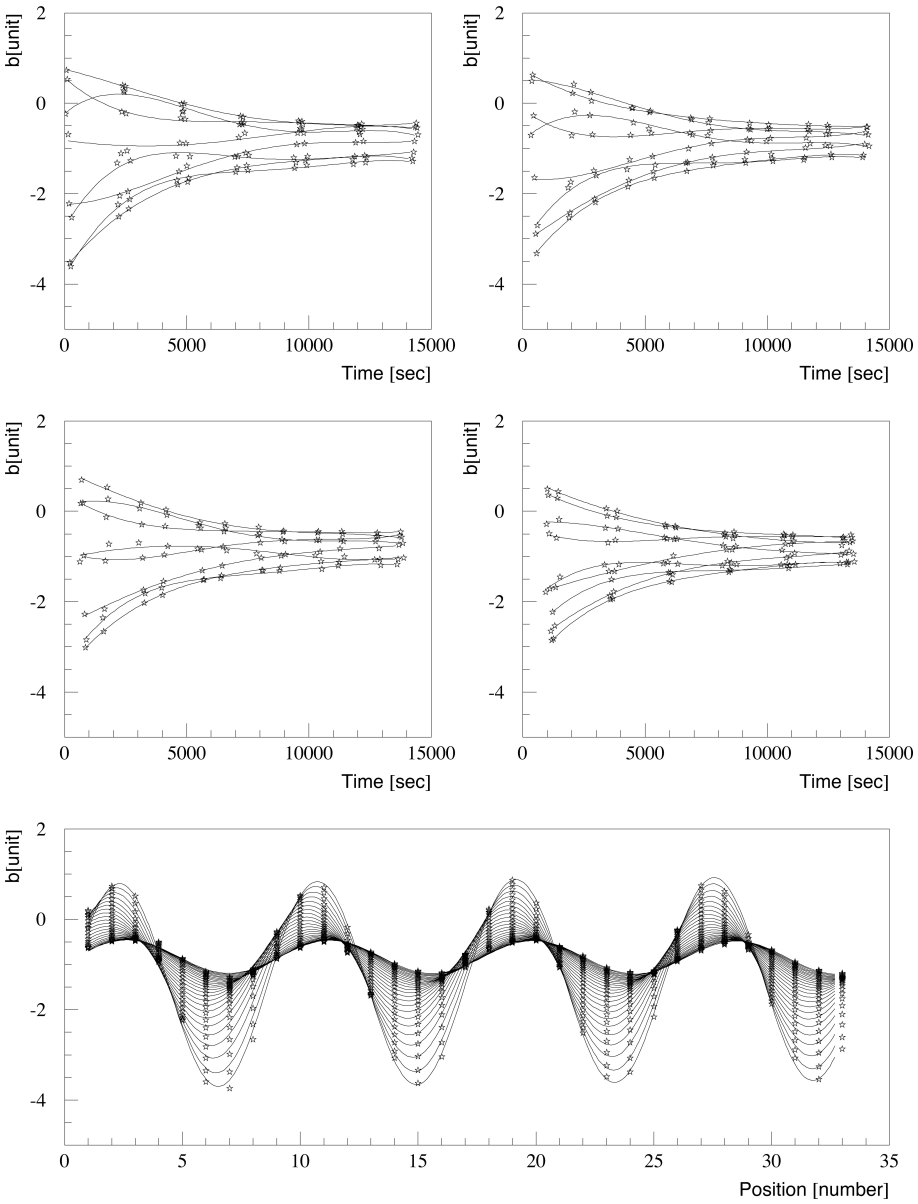

Figure 2.9: Example of the polynomial fittings (upper four graphs) and the simultaneous periodic pattern by the fitting.

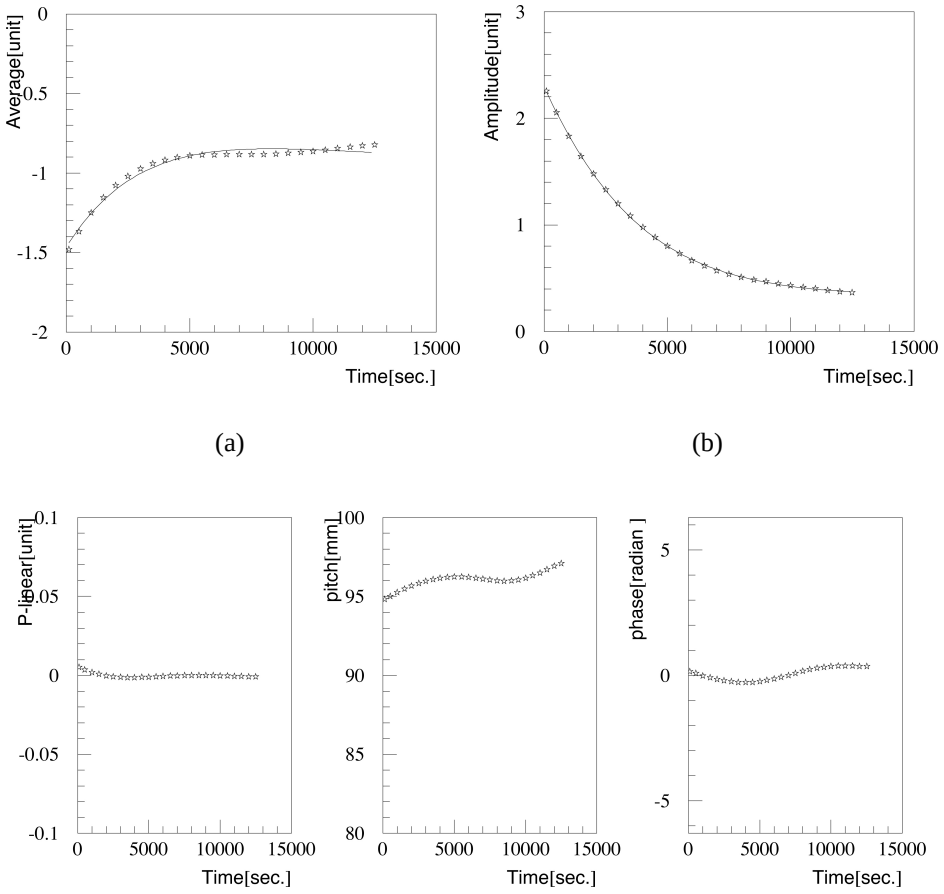

Figure 2.10: Example of fitting results of (a) average field b_n^{ave}, (b) amplitude of periodic pattern b_n^{amp}, and (c) parameters, the b_n^{lin}, the wave length λ (pitch), and the phase δ.

Fig. 2.11 is the typical b_n^{ave}, a_n^{ave} obtained by the fitting process. The difference of the multipole field at the initial and at the four hours later introduces the beam instability during the injection period. Primarily, the correlation of the decay time constants of the average and the amplitude have to be analyzed, in order to explain the origin of two phenomena. However, the fitting function could not be determined to one format, because of complicated behavior of the decay.

Therefore, the results of the fittings made at the time to measurement start and at time after four hours, were analyzed. The time variation during the 4 hours(14400 sec.) of average multipoles(Δb_n^{ave}, Δa_n^{ave}) and of amplitudes of periodic patterns(Δb_n^{amp}, Δa_n^{amp}) are obtained by the following equations, as shown in Fig. 2.12.

$$\Delta b_n^{ave} = b_n^{ave,0} - b_n^{ave,14400}, \qquad \Delta a_n^{ave} = a_n^{ave,0} - b_n^{ave,14400}, \tag{2.3}$$

$$\Delta b_n^{amp} = b_n^{amp,0} - b_n^{amp,14400}, \qquad \Delta a_n^{amp} = a_n^{amp,0} - a_n^{amp,14400} \tag{2.4}$$

Fig. 2.13 shows scatter plot of Δb_n^{ave}, Δa_n^{ave} vs. Δb_n^{amp}, Δa_n^{amp} of allowed multipole b_6 (normal 12-pole) of the magnets. Flat top current dependences are shown in Fig. 2.13(a). Almost all the magnet have same tendency that the average field change is increased with amplitude change, which is increased with the current of the flat top. The correlation with 7 kA 1 hour pre-cycling is different from the others, as shown in Fig. 2.13(b). In this case, it seems that the average decay is saturated, although the amplitude variation increases. The tendency is in almost all the magnet measurement. The other allowed and non-allowed multipoles also have the tendency that the results after 7 kA and 1 hour pre-cycling is different from the others. The scatter plot of a_6 (skew 12-pole) is shown in Fig. 2.14.

Major components of the b_n and a_n are; 1) a component due to the geometric errors of the magnet structure, 2) that due to the magnetization of the superconductor. The static errors in both allowed and non-allowed multipoles can be well understood by introducing the geometric errors. It is important to note that a time variation of the multipoles are observed in both allowed and non-allowed multipoles. The time variation of the multipoles is considered by introducing the time variation of the conductor magnetization. As stated previously, many studies were made to understand this mechanism. They have been, however, concentrated on the allowed multipoles, and have not been made to explain non-allowed multipoles time change.

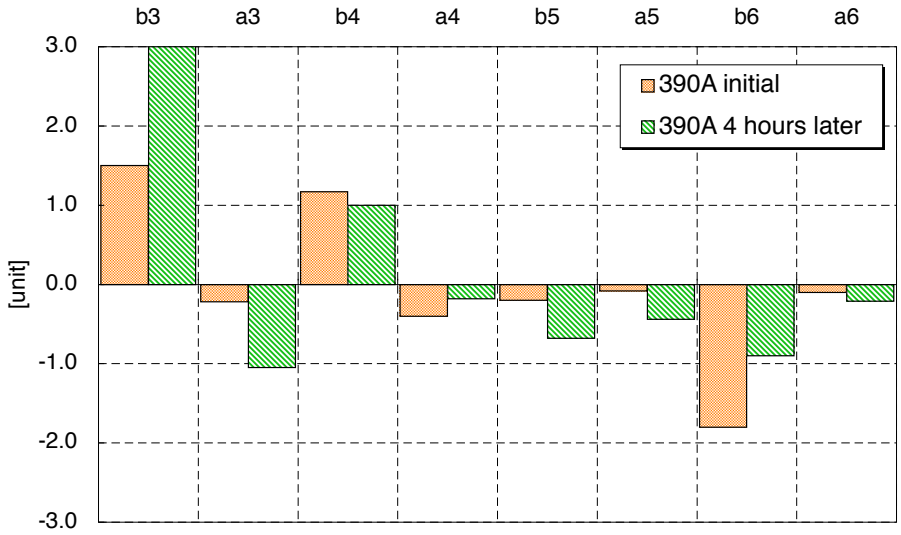

Figure 2.11: Typical results measured by using the 25 mm harmonic coil at the injection field.

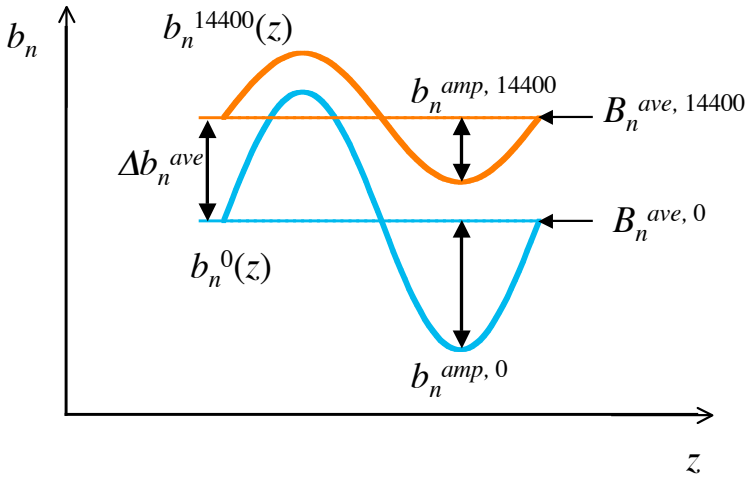

Figure 2.12: Schematics of definitions for analysis. The blue line indicates the curve $b_n^0(z)$, and the orange line indicates the curve $b_n^{14400}(z)$.

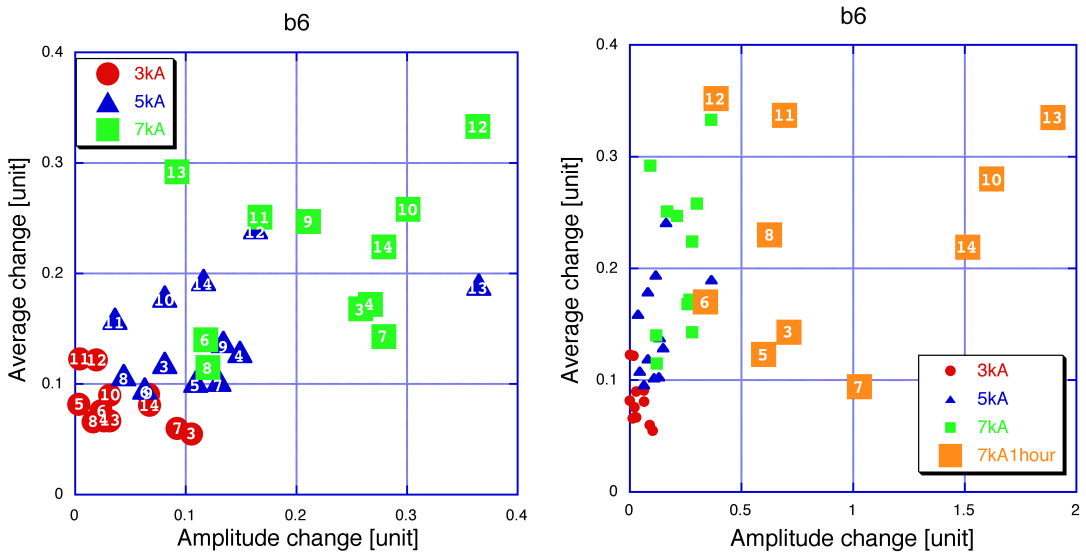

(a) (b)

Figure 2.13: Amplitude change vs. average change of b_6 coefficients. The number in the keys indicates the number of magnet. (a) depicted the results after 3, 5, 7 kA-3 min. pre-cycling. The results after 7 kA-1 hour pre-cycling are described in (b), of which horizontal axis from 0 to 0.4 is corresponding to (a).

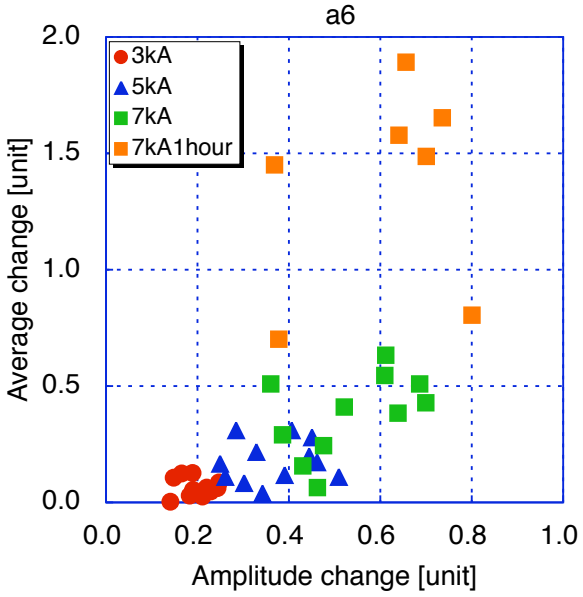

Figure 2.14: Amplitude change vs. average change of a_6 coefficients.

2.2 Measurement of superconductor magnetization

Superconductor filament magnetization in an excited magnet, which is cause of magnetic field error, is influenced by local magnetic field change due to current equalization. In order to understand the mechanism of time-varying multipole field, an magnetization curve is clarified when magnetized filaments are exposed in external field with arbitrary angles.

2.2.1 Experimental layout and procedure

Superconductor magnetization was measured by using a Vibrating Sample Magnetometer (VSM), which is in the National Institute of Material Science (NIMS), Japan. The VSM consists of a superconducting split coil, a sample holder, pick-up coils, and a cryostat, as shown in Fig. 2.15. The split coil induces the bias magnetic field in the horizontal direction. The sample attached to the holder vibrates along the z axis. Small magnetic field induced by sample magnetization is picked up by small coils around samples. The pick-up coils are arranged to cancel the background field. The magnetic moment is calculated automatically from induced voltage of coils.

The sample is a 4 mm long strand used in the quadrupole magnet for the LHC interaction regions as the inner cable, summarized in Table 2.2. Both ends of the sample were polished to avoid the connection between filaments which induces loop currents.

The measurements are performed according to the process, as shown in Fig. 2.16. The sample is warmed up beyond the critical temperature before every measurement to vanish a magnetization. After warm up, the sample is rotated to angle $-\alpha$ to the initial angle defined as zero, and is cooled down to 4.2 K for superconducting state. Then sample is exposed in a magnetic field excitation cycle induced by the split coil. After the excitation cycle, the superconductor filament is fully magnetized without external field. Then the sample rotated by angle α to measure at the angle of zero. After rotation, the second excitation cycle is started. α is selected 30, 60, 90, $\cdots$, 360 degrees as a parameter of the measurement.

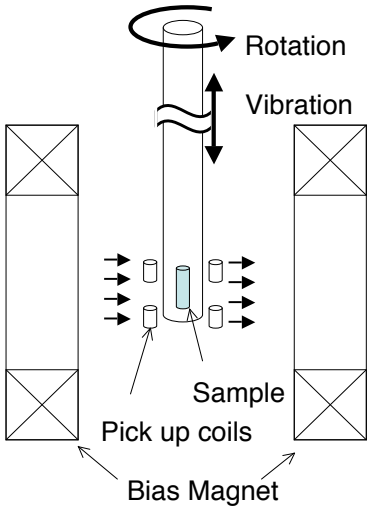

Figure 2.15: Schematic view of vibrating sample magnetometer. The sample can be rotated in plane surface parallel to the bias magnetic field.

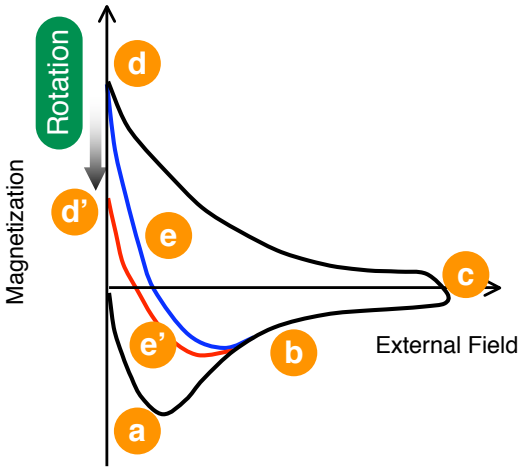

(a)

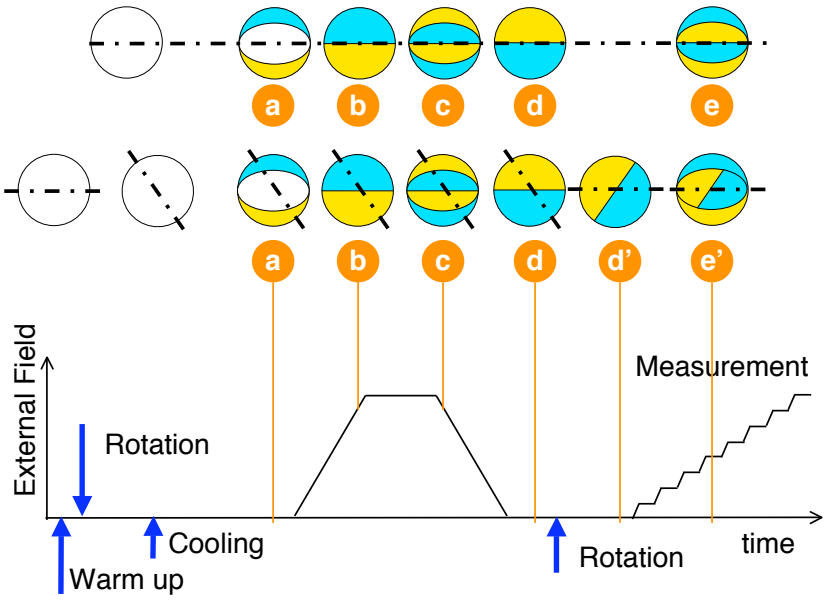

(b)

Figure 2.16: (a) Sketch of magnetization curve in measurement. (b) Procedure of VSM measurements.

2.2.2 Results

The result of measurement is shown in Fig. 2.17(a). After the complete change of magnetization direction, the magnetization curves indicate good agreement with each other. That means the measurement were performed in stably. The data with angle α and $-\alpha$ should indicate the same magnetization curve. However, a slight difference was observed. It is thought that the difference is caused by remanent magnetic field by the split coil. The effect is canceled by taking average of the data of α and $-\alpha$. Fig.2.17(b) is the curves after the cancellation. The experimental results are applied to the evaluation of the code that computes a superconductor magnetization behavior, in next Section.

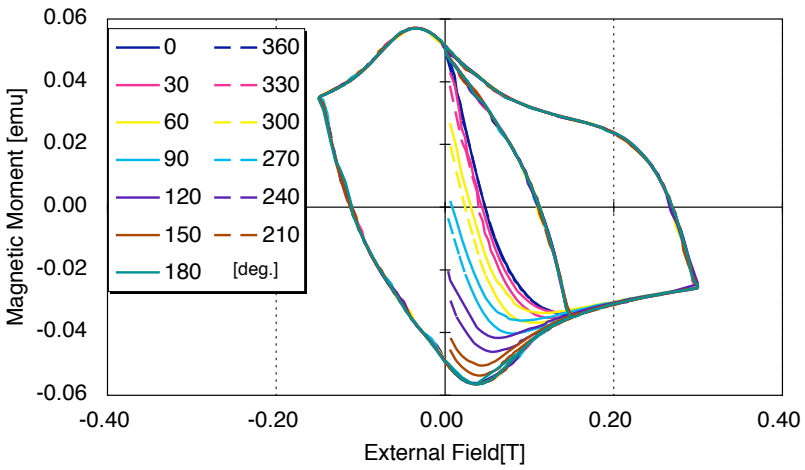

(a)

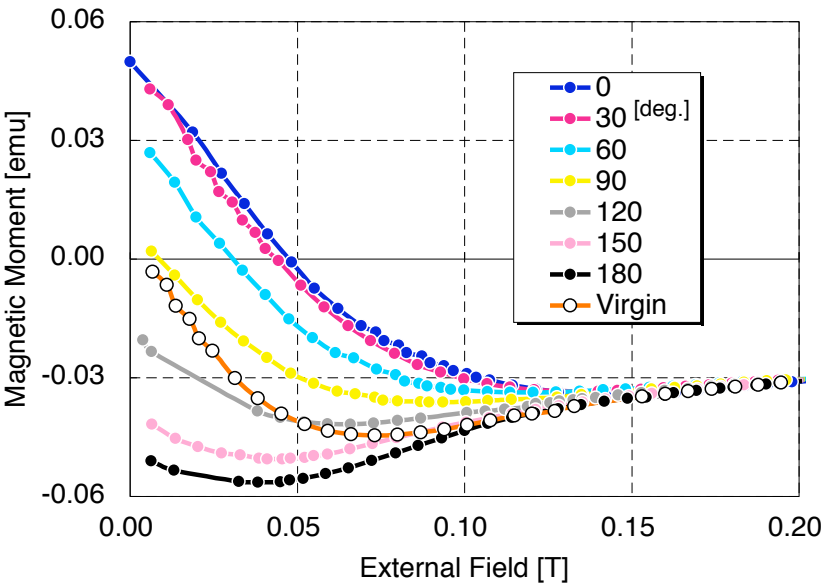

(b)

Figure 2.17: (a) Measured results of the magnetic moment with the various angle of the external field, and (b) angle dependence of the magnetic moment behavior after taking the average at low field range.

Chapter 3

Simulation of Superconductor Magnetization and Their Effect on Magnetic Field Quality

Numerical computation code for evaluations of the experimental studies was developed. The first code computes the superconductor magnetization by the model with the nested cosine theta current distribution. The second one evaluates correlation between imbalance currents and periodic magnetic pattern. Finally, these codes was extended into the simulation of magnetic field quality change due to re-magnetization induced by imbalance current equalization.

3.1 Superconductor magnetization

3.1.1 Nested cosine theta model

Type Ⅱ superconductor magnetization is usually computed by the Bean model[33]. The model for the cylindrical filament magnetization adopted the Bean model is described by M. N. Wilson[34]. In the model, a persistent current to screen a external magnetic field flows with critical current determined by the external magnetic field. M. Haverkamp adopted the Bean model to describe the behavior of filament magnetization induced by the external field change with arbitrary angle[19]. However, filament magnetization computed by a constant persistent current can not explain asymmetric magnetization behavior at low field range, as indicated by the VSM experimental results.

C. Völlinger developed a new magnetization computation model, the so-called "*nested ellipse model*"[35]. In this model, persistent current density is changed with

depth from a filament surface. The filament is divided into coaxial cylindrical shells. The persistent currents flow in two ellipses inside the shells. The persistent current determined by external field flows in a shell at filament surface, and the inner persistent current flows with a critical current determined by a magnetic field reduced by the persistent current in the outer shells. The critical current density of the inner ellipse is larger than that in the outer shells. The model reproduces the asymmetry of magnetization at the low magnetic field range. The model can also compute a filament magnetization behavior due to change of an external field with arbitrary direction. In the model, a persistent current flows inside the ellipse with the critical current density. The computation are good agreement with experimental results, although the effective current density is not the critical value, because current free regions remain between shells.

In order to simplify the computation, the "*nested cosine theta model*" was developed. In the model, the persistent current flows with cosine theta distribution in the coaxial cylinder shell dividing the filament into the number of N.

The magnetization computation starts from the virgin (non-magnetized) state as follows. Current density distribution of the most outer shell is determined by the external magnetic field, B_{ext}, and described as,

$$j = j_c(B_{ext}) \cos\theta. \tag{3.1}$$

Here j_c is the critical current density of the superconductor in the external magnetic field, B_{ext}. The current induces pure dipole field, $B[1]$ in the inner shells,

$$B[1] = -\frac{\mu_0 j_c(B_{ext})}{2} \Delta t, \tag{3.2}$$

where Δt is thickness of the shell.

The next shell is exposed to the external field and magnetic field by the first shell. The current distribution is

$$j = j_c(B_{ext} + B[1]) \cos\theta. \tag{3.3}$$

The current induces a pure dipole field in inner shells,

$$B[2] = -\frac{\mu_0 j_c(B_{ext} + B[1])}{2} \Delta t. \tag{3.4}$$

The n-th shell feels the magnetic field described as

$$B_n^{feel} = B_{ext} + \sum_{k=1}^{n-1} B[k]. \tag{3.5}$$

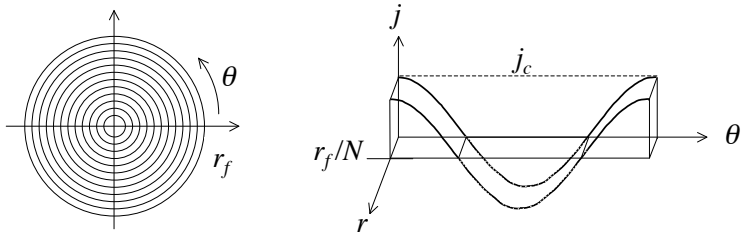

Figure 3.1: Schematic view of coaxial cylindrical shells in a filament and cosine theta current distribution.

The n-th shell current is described as

$$j = j_c(B_n^{feel}) \cos\theta. \tag{3.6}$$

The magnetic field induced by the n-th shell is

$$B[n] = -\frac{\mu_0 j_c(B_n^{feel})}{2} \Delta t. \tag{3.7}$$

This operation is repeated until the internal magnetic field is zero, $B_n^{feel} = 0$, or fully penetrated. Fig. 3.2 explains this formulae.

The magnetic moment of the n-th shell is

$$\begin{aligned} m_n = \int dm_n &= \int 2x \cdot l_f \cdot j \cdot dxdy \\ &= 2l_f \cdot j_c(B_n^{feel}) \cdot \int_{r_n}^{r_{n-1}} r^2 dr \cdot \int_{-\frac{\pi}{2}}^{\frac{\pi}{2}} \cos^2\theta d\theta \\ &= \pi \cdot j_c(B_n^{feel}) \cdot l_f \cdot \left(\frac{r_{n-1}^3 - r_n^3}{3} \right). \end{aligned} \tag{3.8}$$

Here $r_n = r_f - n\Delta t$ is the inner radius of the n-th shell, and l_f is the filament length. Total magnetic moment of the filament is,

$$m_f = \sum_{n=1}^{N} m_n. \tag{3.9}$$

Calculated magnetization behavior with the nested cosine theta model is shown in Fig. 3.3. Comparison of the magnetization curve between the Bean model and the nested cosine theta model is shown in Fig. 3.4. The right-left asymmetry of the curve were reproduced by the nested cosine theta model computation.

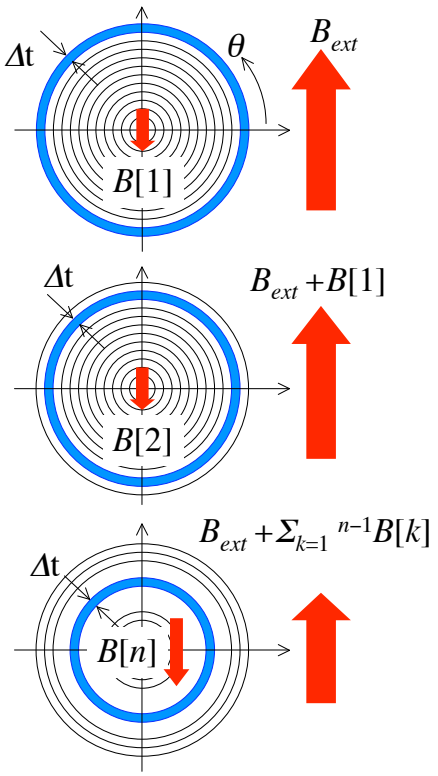

1st shell

$$j = j_c(B_{ext})\cos\theta$$
$$B[1] = -\mu_0 j_c(B_{ext})\ \Delta t/2$$

2nd shell

$$j = j_c(B_{ext}+B[1])\cos\theta$$
$$B[2] = -\mu_0 j_c(B_{ext}+B[1])\ \Delta t/2$$

n -th shell

$$j = j_c(B_{ext}+\Sigma_{k=1}{}^{n-1}B[k])\cos\theta$$
$$B[n] = -\mu_0 j_c(B_{ext}+\Sigma_{k=1}{}^{n-1}B[k])\ \Delta t/2$$

Figure 3.2: Schematic view of the nested cosine theta model.

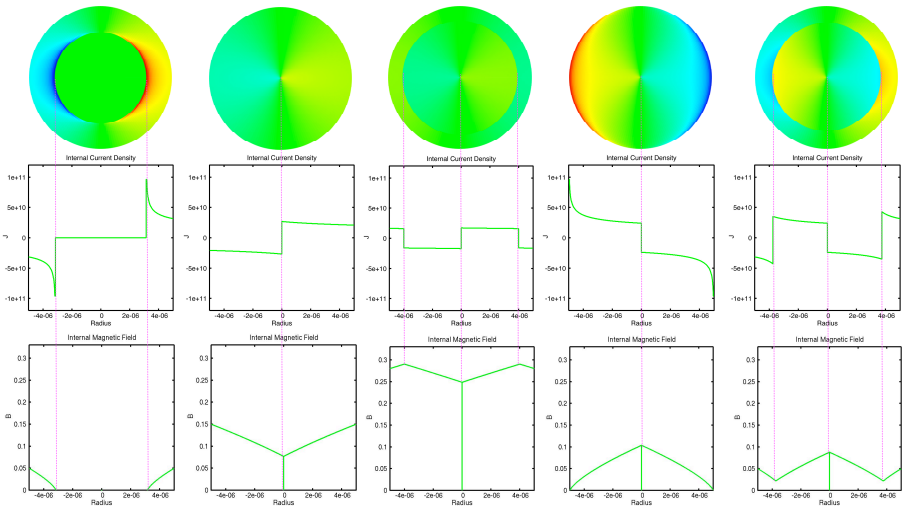

Figure 3.3: Magnetization behavior based on the nested cosine theta model.

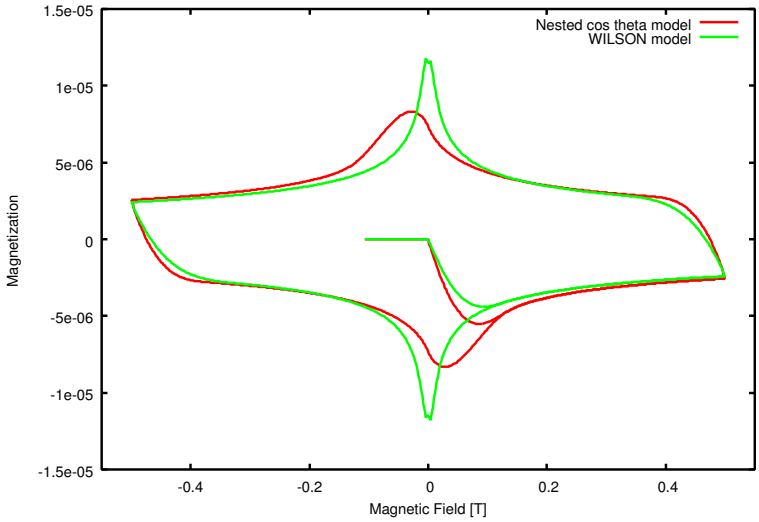

Figure 3.4: Comparison of magnetization curve between the Bean model and the nested cosine theta model.

3.1.2 Effect of field change with arbitrary direction

The above equations treat one dimensional external magnetic field. In order to compute the effect of the change of an external field with an arbitrary direction, the nested cosine theta model was expanded to two dimensional equations.

Initial external field with angle ψ is expressed as

$$\boldsymbol{B}_{ext}^{ini} = B_y + iB_x = B_{ext}(\sin\psi + i\cos\psi). \tag{3.10}$$

Similar to (3.1), the magnetic field is shielded by the current distribution described as

$$j = -j_c \sin(\theta + \psi). \tag{3.11}$$

In this computation coordinate, the angle zero is corresponding to the x-axis, therefore, the sine function were applied. The current distribution of the n-th shell induces dipole field described as

$$\boldsymbol{B}[n] = -\frac{\mu_0 j_c(B_n^{feel})}{2}\Delta t(\sin\psi + i\cos\psi). \tag{3.12}$$

The equation is corresponding to (3.7). Here,

$$B_n^{feel} = |\boldsymbol{B}_n^{feel}| \tag{3.13}$$

$$= \boldsymbol{B}_{ext} + \sum_{k=1}^{n-1} \boldsymbol{B}[k]. \tag{3.14}$$

This operation is repeated until the internal magnetic field is zero, $B_n^{feel} = 0$, or fully penetrated.

A magnetic moment of the shell is,

$$\boldsymbol{m}_n = (m_{xn}, m_{yn}) \tag{3.15}$$

$$= -\pi \cdot j_c(B_n^{feel}) \cdot l_f \cdot \left(\frac{r_{n-1}^3 - r_n^3}{3}\right)(\cos\psi, \sin\psi) \tag{3.16}$$

The total magnetic moment of the filament is,

$$\boldsymbol{m}_f = (m_x, m_y) = \sum_{n=1}^{N}(m_{xn}, m_{yn}), \tag{3.17}$$

which is corresponding to (3.9).

The above equations described the two dimensional magnetic field in virgin state. From here, the second cycle, which is re-magnetization process, is described.

The fully magnetized superconductor is re-magnetized by external field with an arbitrary direction. The initial/modified shielding magnetic fields induced by the shells are described with superscript "*ini*"/"*mod*", as $\boldsymbol{B}[n]^{ini}/\boldsymbol{B}[n]^{mod}$. The external field with modification is described as,

$$\boldsymbol{B}_{ext}^{mod} = \boldsymbol{B}_{ext}^{ini} + \Delta\boldsymbol{B}_{ext}. \tag{3.18}$$

Here, the amount of magnetic field change is described by using the angle δ_0 as,

$$\Delta\boldsymbol{B}_{ext} = \Delta B_{ext}(\sin\delta_0 + i\cos\delta_0). \tag{3.19}$$

In the first shell, current flows to shield $\Delta\boldsymbol{B}_{ext}$. The current distribution of the shell changes to

$$j = -j_c \sin(\theta + \delta_0), \tag{3.20}$$

from (3.11). The current in the first shell induces the magnetic field,

$$\boldsymbol{B}[1]^{mod} = -\frac{\mu_0 j_c(B_{ext}^{mod})}{2}\Delta t(\sin\delta_0 + i\cos\delta_0). \tag{3.21}$$

The second shell feels magnetic field superimposed of three origins; (a) the external magnetic field change, (b) magnetic field change due to disappearance of the initial

magnetic field of the first shell, (c) magnetic field induced by the first shell after the modification. Therefore, the second shell experiences magnetic field change described as

$$\boldsymbol{B}_2^{feel,mod} = \Delta\boldsymbol{B} - \boldsymbol{B}[1]^{ini} + \boldsymbol{B}[1]^{mod}. \tag{3.22}$$

In order to clarify the angle change dependence the equation is described as

$$\begin{aligned}\boldsymbol{B}_2^{feel,mod} =& \Delta B_{ext}(\sin\delta_0 + i\cos\delta_0) \\ &- [-\frac{\mu_0 j_c(B_{ext}^{ini})}{2}\Delta t(\sin\psi + i\cos\psi)] \\ &+ [-\frac{\mu_0 j_c(B_{ext}^{mod})}{2}\Delta t(\sin\delta_0 + i\cos\delta_0)].\end{aligned} \tag{3.23}$$

Fig. 3.5 describes the schematics of the explanation. This process is repeated until the field change is corrected completely or penetrates the filament fully. And then, the magnetization can be computed, similarly.

A example of the magnetization behavior by using this code is shown in Fig. 3.6. The pattern like whirlpool appears as current density distribution in the filament cross section. It appears from the rotation of the angle of peak of current distribution due to that the each shell feels the magnetic field of previous shells.

The angle dependence of the magnetization curve could be obtained by using the code, as shown in Fig. 3.7. The computations were performed in order to reproduce the VSM measurements. In consequence, the curves indicated good agreement with experimental results. Therefore, the code was evaluated, and it was judged that can be used in also the simulation of the magnetization behavior in background magnetic field such as magnet excitation.

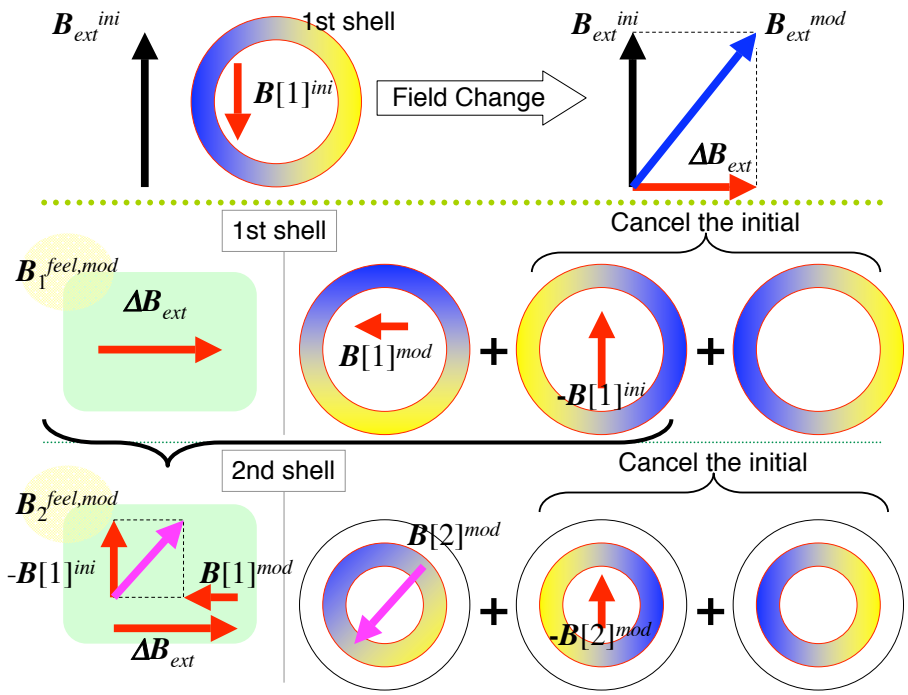

Figure 3.5: Schematic view of re-magnetization due to the external magnetic field change for first and second shells.

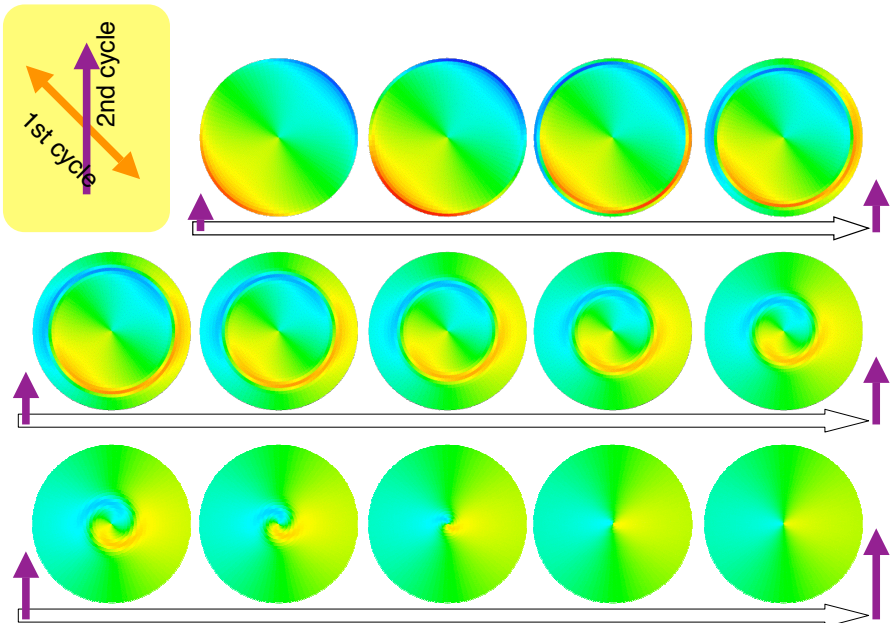

Figure 3.6: Re-magnetization behavior by using the nested cosine theta model. At first, the filament fully was magnetized with 45 degree to the vertical direction without background field. Then the magnetic field with vertical direction increases. The pictures are sorted from upper left to lower right. By increasing the magnetic field, the pattern like whirlpool moves toward center of filament.

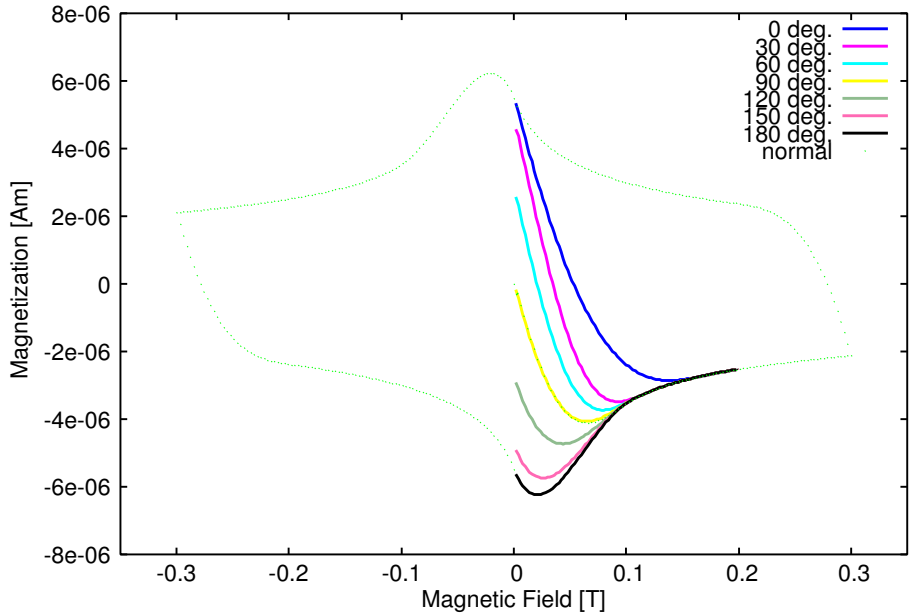

Figure 3.7: Computation results of the magnetization behavior with magnetic field change of several directions by using the nested cosine theta model.

3.2 Periodic magnetic pattern

It was postulated that imbalance currents in a Rutherford cable induce a periodic magnetic pattern. Imbalance currents are represented by zigzag currents, and the induced magnetic field was studied.

3.2.1 Pair zigzag current model

An imbalance current in a superconducting Rutherford cable is assigned as a zigzag current of which transposition length is equal to the twist pitch of the cable. First of all, the simplest model of a pair of zigzag currents which have half a twist pitch difference as shown in Fig. 3.8 is studied. The currents flow in opposite directions along the zigzag lines. The model is based on the cable dimension of the quadrupole magnet for the LHC interaction region, as shown in Table 3.1. A longitudinal distribution of transverse magnetic field on the z-axis induced, by the currents in parallel with the axis, is evaluated.

The magnetic field induced by a line current element is described as,

$$B = \frac{\mu_0 I}{4\pi h}(\cos\theta_1 + \cos\theta_2). \tag{3.24}$$

Here, I is line current, h is distance from line current to computation point, and θ_1 and θ_2 are angles, as shown in Fig. 3.9. The magnetic field at several positions on the z-axis is computed as the sum of the magnetic field of each current element.

The computed magnetic field distribution induced by a pair of currents of ±50 A with various distances are shown in Fig. 3.10. The shape of distribution produced by a pair of currents farther from the axis is closer to sinusoidal. The amplitude of the periodic pattern is depicted in Fig. 3.11 as a function of distance. The 5th power dependence of amplitude of sinusoidal shape distribution was obtained, as shown in Fig. 3.11.

The current dependence of the magnetic field is indicated in Fig. 3.12. In this calculation, the distance was set to 23.6 mm corresponding to the distance from the first layer to the reference radius of the LHC interaction regions quadrupoles. The amplitude has linear dependence of the current, as shown in Fig. 3.13. From comparison with the magnetic field measurement, the imbalance current was estimated to be of the order of a 100 A. The results means that the current in the several strands flows with opposite direction to the direction of the transport current, because the average of the transport current for one strand is 14.4A (= 390 A / 27 strands).

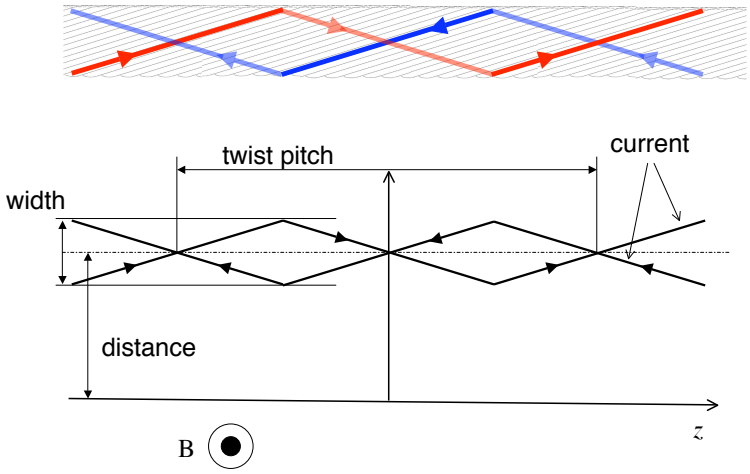

Figure 3.8: Sketch of the pair current model assigned as a pair of zigzag currents.

Table 3.1: Parameters of Two Strands Model of a Pair of Zigzag Currents

Twist pitch [mm]	90
Width [mm]	11.2
Length [pitch length]	20

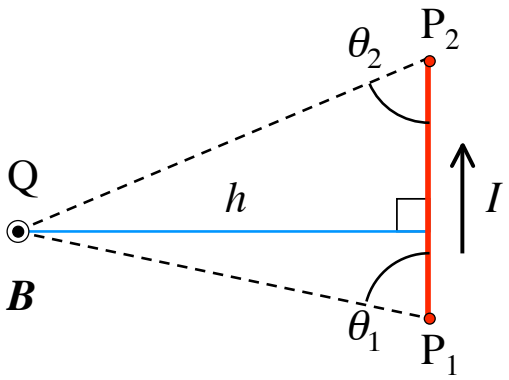

Figure 3.9: Schematic view of the computation of the magnetic field induced by a line current element. The current flows from P_1 to P_2, and their magnetic field is evaluated at Q. The parameters of θ_1, θ_2, and h needed to the computation is determined by three coordinates of P_1, P_2, and Q.

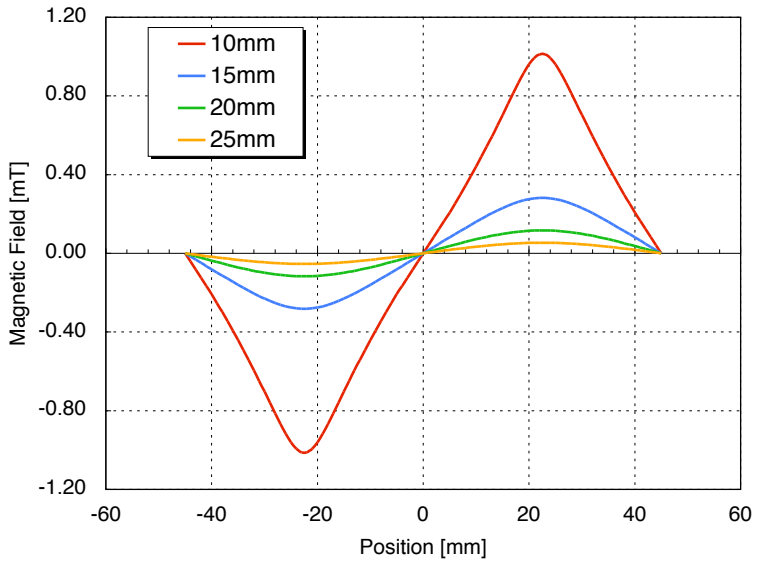

Figure 3.10: Magnetic field distribution induced by a pair of zigzag currents of ±50 A with the different distances from the *z*-axis.

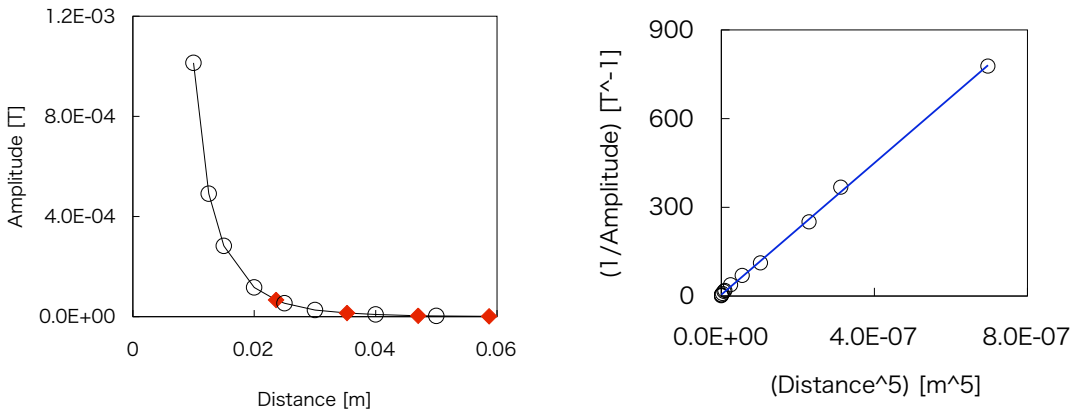

(a) (b)

Figure 3.11: Distance dependence of the periodic pattern amplitude; (a) linear plot (The red keys are corresponding to each layer of the LHC interaction quadrupole.) , and (b) $(\text{Distance})^5$ vs. $(\text{Amplitude})^{-1}$.

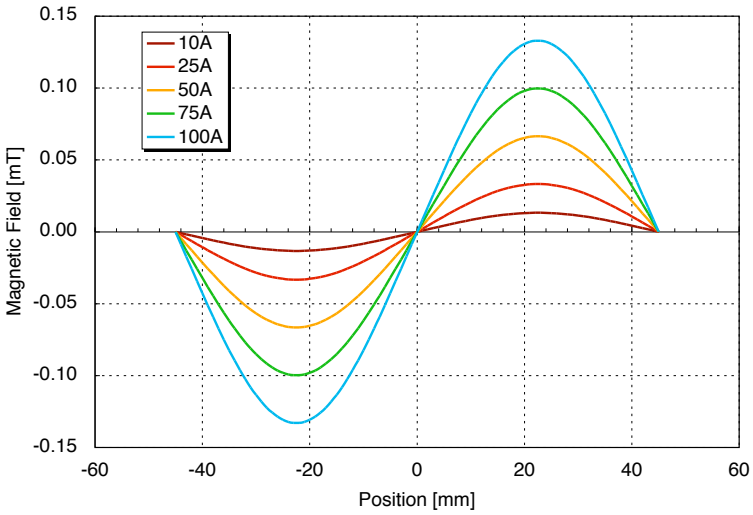

Figure 3.12: Magnetic field distribution induced by a pair of zigzag currents, for the different currents. The distance was set to 23.6 mm corresponding to the distance from the first layer to the reference radius of the LHC interaction region quadrupole.

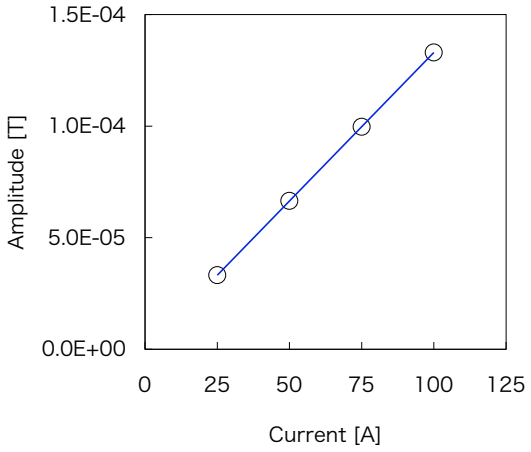

Figure 3.13: Current dependence of the periodic pattern amplitude.

3.2.2 Superconducting cable modeling

The superconducting cable model is composed of zigzag currents of number which is equal to the number of strands in the cable, as shown in Fig. 3.14. The model is based on the cable for the LHC interaction region's quadrupole magnet, as shown in Table 3.2. The calculation conditions are also shown in the table. The currents along the zigzag lines are assigned randomly within a limited current. And, in order to simulate the imbalance current, the total of the currents is zero.

The longitudinal magnetic field distribution by the computation is shown in Fig. 3.15. The sum of all the magnetic field distribution is indicated by the red line. The offset of the sum is absolutely zero, because the total of all the zigzag currents is assigned to be zero. The amplitude of the other periodic patterns with a larger offset is larger, because the pattern is caused by larger currents.

The amplitude of the sum of patterns is randomly distributed, if the computation is repeated. Fig. 3.16 shows histogram of amplitude by 10,000 computations. In the computation, the limited current is 100 A, and the peak of the histogram is 0.04 mT. From other computations with different limited currents, it was confirmed that the peak amplitude of the distribution is proportional to the limit current, and keeps the same distribution form e.g. the peak of histogram is 0.4 mT for the limited current of ±1000 A.

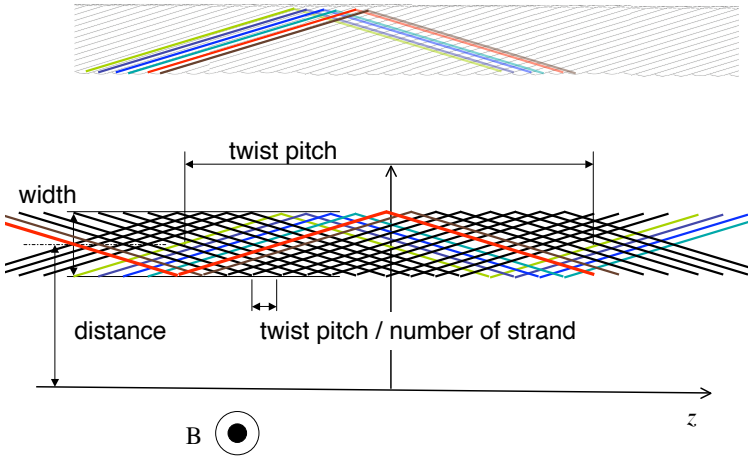

Figure 3.14: Sketch of the cable model assigned as zigzag currents.

Table 3.2: Parameters of Modeling by Zigzag Currents

Twist pitch [mm]	90
Width [mm]	11.0
Length [Pitch]	60
Number of currents	27
Distance [mm]	23.6
Limited current [A]	±100.0

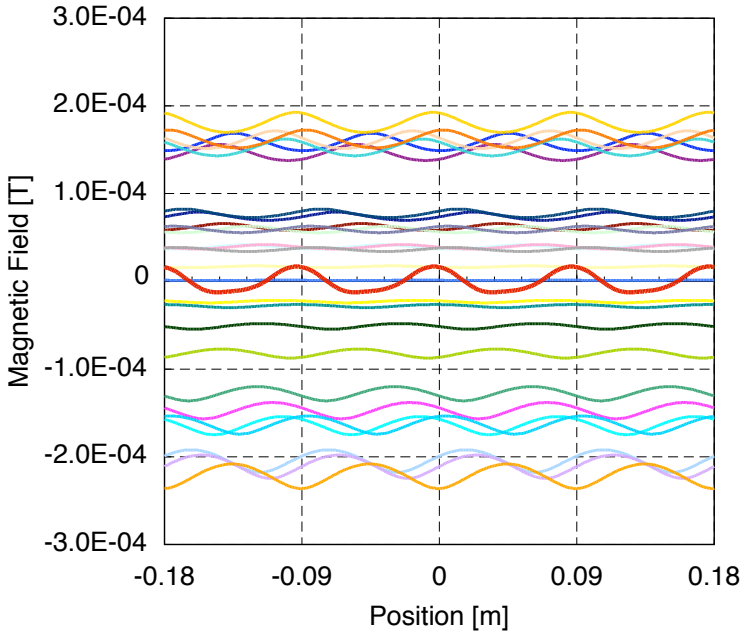

Figure 3.15: Typical distributions of magnetic field induced by zigzag currents. The colors of the lines indicates the magnetic field induced by each zigzag current. The red line indicates the sum of all the magnetic field.

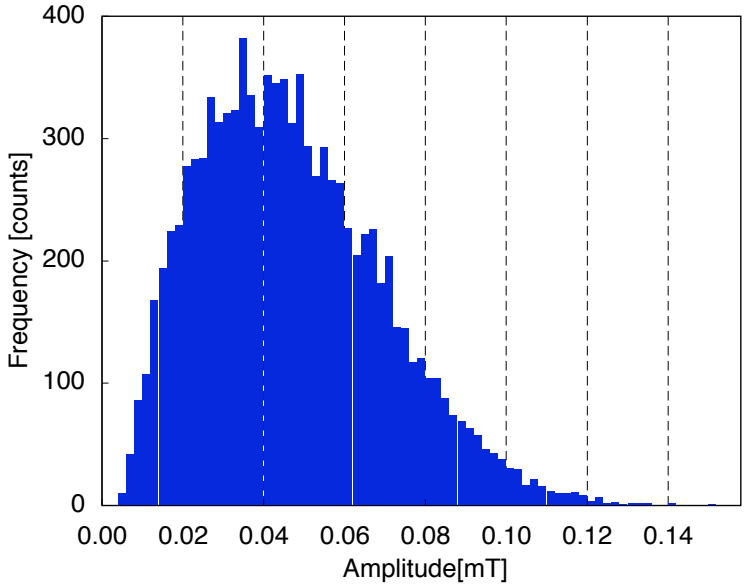

Figure 3.16: Histogram of periodic pattern amplitude obtained from 10,000 computations in case of the limited current of ±100 A.

3.2.3 Modeling of single layer magnet

A single layer magnet is modeled by a stack of the superconducting cable model described previously. The model is based on the first layer of the quadrupole magnet for LHC interaction regions, because the contribution to the periodic pattern of this layer seems the main component from measured periodic pattern and the evaluation results of the distance dependence of the periodic pattern amplitude. The model is composed of a stack of the 96 cable models on the position of the first layer cables, as shown in Fig. 3.17(a). The modeling parameters are given in Table 3.3.

The currents of zigzag lines in the cables are given randomly with the limited current of ±20 A instead of that of ±100 A in previous computation. According to the previous section, there is linear correlation between the limited current and amplitude of periodic pattern. Therefore, the limited current is not important in the case of study of the distribution shape of the magnetic field. The histogram of the current of a typical computation is shown in Fig. 3.17(b).

The magnetic field is computed by expansion to three dimension of line current element formula(3.24), as shown in Fig. 3.18. At first, the absolute magnetic field by an element is calculated. Then, it can be translated to magnetic vector components of (B_x, B_y, B_z) by the normal vector of the plane surface. In this model computation, the magnetic field on the reference radius was evaluated as multipole field, and its distribution shape was analyzed.

The magnetic field distribution on the reference radius was computed about three patterns of the current distribution, as shown in Fig. 3.19(a). Fig. 3.19(b) indicates the computation results with initial current distribution. The differences of the amplitudes or the phases between each multipole field is obtained, which is consistent with the observed periodic pattern. When each current in the strands decrease to the half of initial one, the computation result is shown in Fig. 3.19(c). Obviously the amplitude of any multipoles is the half of initial one.

Fig. 3.19(d) shows the computation results of the magnetic field distribution due to local imbalance current changes. In this case, only the currents at pole side block reduced to 20% of the initial ones, as shown in Fig. 3.19(a). Phase shifts and unsteady amplitude changes are indicated. From the calculation results, cause of the observed phase shift or amplitude growth can be thought as non-uniform imbalance current change.

Table 3.3: Parameters of Model of Single Layer Magnet

Number of cables	96
Length [pitch length]	30
Number of currents	27
Limited current [A]	±20.0
Reference radius [mm]	17

Almost all the periodic pattern with the property of static phase and amplitude loss in the measurements can be explained by the current equalization among the strands in the cable. Therefore, in the following section, the change of zigzag currents are assumed to keep the similarity of their distribution as simulation of the equalization.

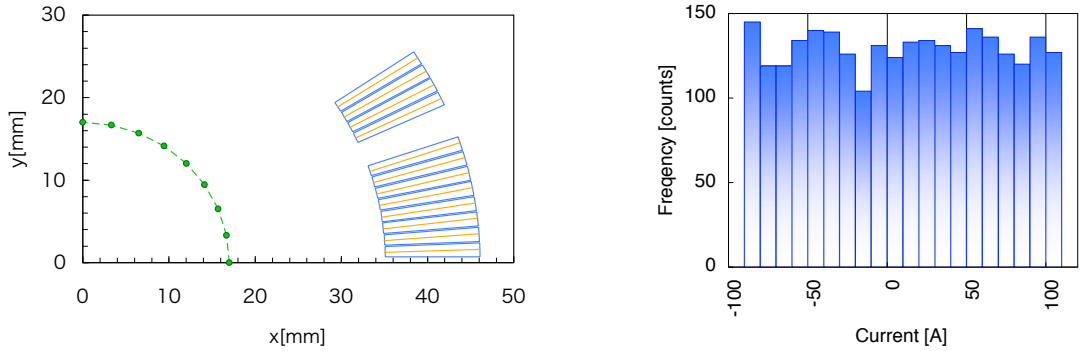

(a) (b)

Figure 3.17: Modeling of single layer magnet; (a) cross sectional view of the octant of the model, and (b) histogram of 2592 zigzag currents in 96 cables. The magnetic field induced by the zigzag currents of the cable model on each cable center expressed by the orange lines is evaluated as the multipole field on reference radius expressed by the green dashed line.

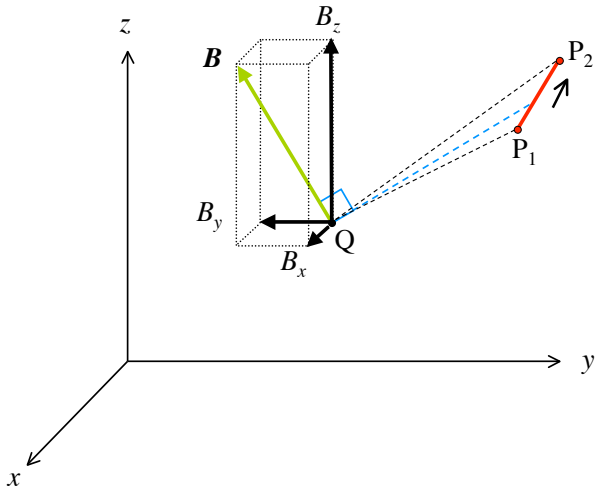

Figure 3.18: Schematics of three dimensional computation for magnetic field due to a line current element. The absolute magnetic field on Q due to line current element from P_1 to P_2 is computed by (3.24). The magnetic field vector component of (B_x, B_y, B_z) is introduced by the normal vector of plane surface determined by P_1, P_2, and Q.

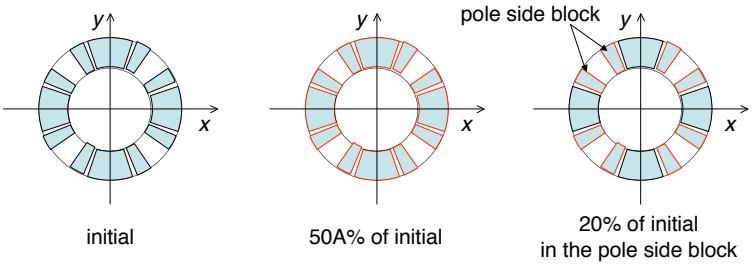

(a)

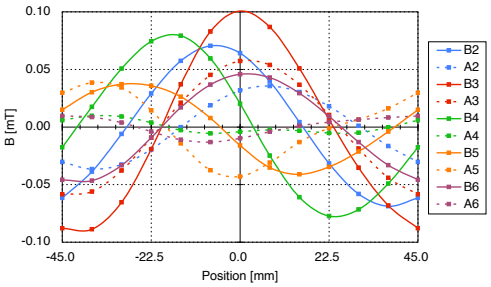

(b)

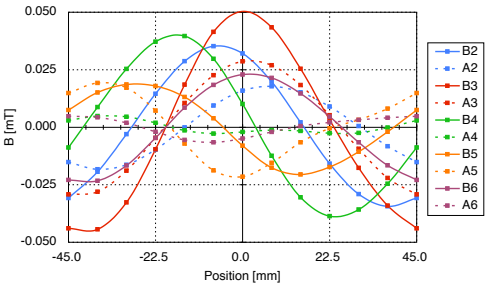

(c)

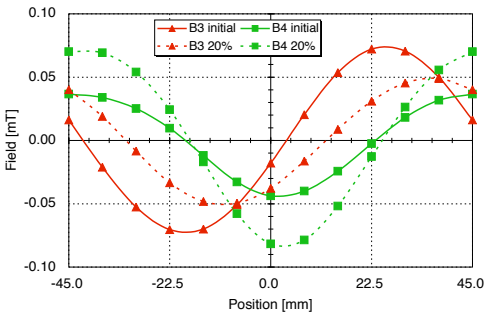

(d)

Figure 3.19: (a) Schematic view of current changes in the single layer magnet model computation. (b) Magnetic field distribution with limit of current of ±20 A. The colors of lines are corresponding to each multipoles. (c) Magnetic field distribution with the half of the currents of (a). (b) Comparison of magnetic field distribution of B_3 and B_4 between the initial currents distribution and 20% of it in the pole side block. The amplitude of the periodic pattern of $B4$ increased although that of $B3$ reduced.

3.3 Magnetic field error

The simulation code for evaluation of field quality was developed with the above computation codes. The magnetic field quality taking into account electromagnetic interactions inside the magnet can be computed by the developed model.

3.3.1 Simulation procedure

Conceptual plan of the simulation is described in Fig. 3.20. The computation performed on eight cross sections of the magnet model divided with one twist pitch, as shown in Fig. 3.21. The cross sectional view of the simulation model is shown in Fig. 3.22. The simulation can reproduce the electromagnetic interactions inside the magnet, according to the following steps.

1. The stack of the cable models reproduces the imbalance currents in the magnet. The cable model with 30 twist pitch lengths is arranged into the cable position in the magnet, as shown in Fig 3.22. The zigzag current distribution is assigned as same in each cable in same pole, and the longitudinal positions of the cables are randomized within one cable twist pitch. The assumption means that the imbalance currents are connected by the end of each pole. The initial current limitation is given as ±20 A.

2. By using formula of the magnetic field computation of the current element explained by Fig. 3.18, the magnetic field on the reference radius is computed, and evaluated as multipole components. The magnetic field is also computed with the half of the initial currents. The periodic pattern amplitude may be a half of initial one.

3. The local magnetic field on the strand positions is also computed by means of the current element method. The magnetization behavior is obtained by the nested cosine theta model described in previous section. In this computation, the magnetization is reproduced taking account of history of the magnet excitation, which is corresponding to the pre-cycling of 50, 7000, 50 kA. After the cycle, the magnetization with superimposed magnetic field of the initial local field and magnetic field at the injection of 390 A are computed. Then, the magnetization with superimposed magnetic field of the half of the initial local field and injection field is computed.

4. The magnetic field induced by the superconductor magnetizations on the reference radius is evaluated by equation(1.4) as multipole field components. The average multipole field is evaluated by the average of eight cross sections of the magnet.

The magnetic field is evaluated over one twist pitch taking into account contribution of the 30 twist pitch lengths of zigzag current. This zigzag model length is enough for computation of one twist pitch at the center of the model.

The initial current limitation of ±20 A is an appropriate value obtained from the previous computations, consistent to the experimental results. In the simulation, the final currents are reduced to a half of the initial value, uniformly. The reduction is an assumption for evaluation of the magnetization change. Therefore, the simulation results with this assumption imply magnetic field change induced by the zigzag current changes within ±10 A.

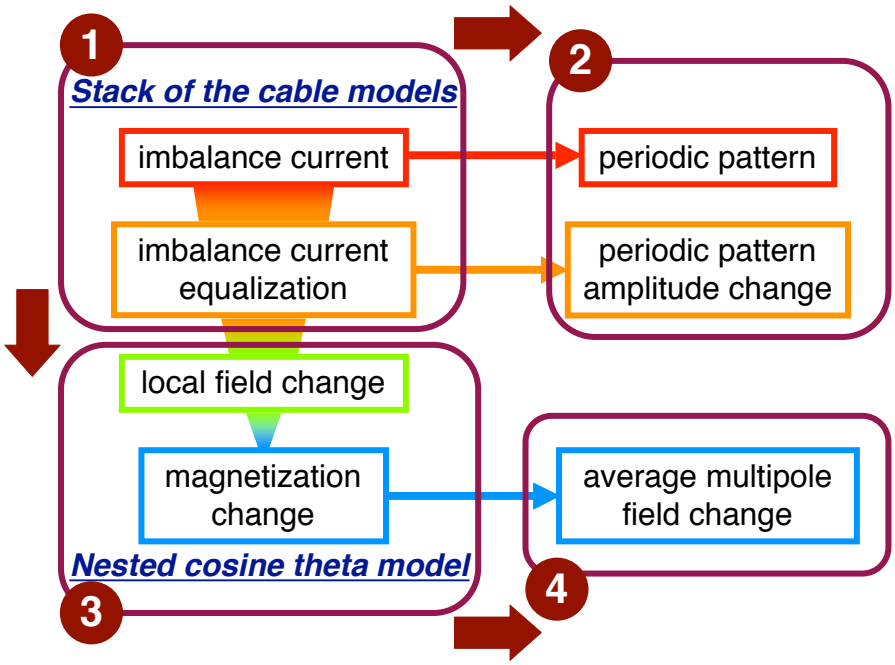

Figure 3.20: Conceptual plan of the simulation to reproduce the field quality change mechanism described in Fig. 1.23. The number is corresponding to the simulation procedure.

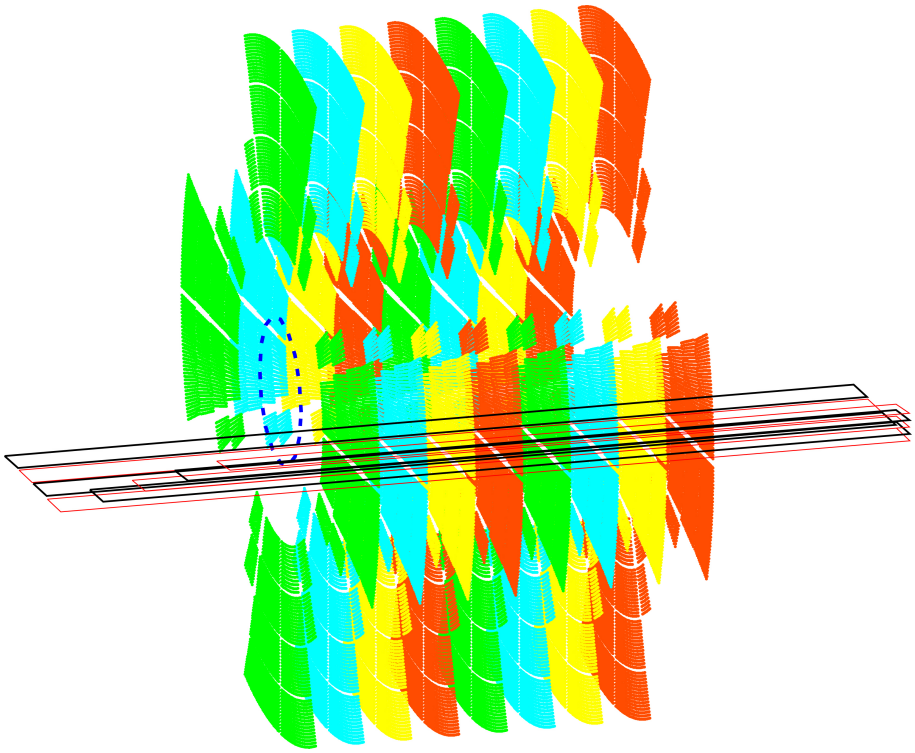

Figure 3.21: Schematic view of the simulation model. The rectangles by the red or the black lines express some of the position of the zigzag current models of which are 30 pitch length. The magnetic field is calculated on the strand position on the longitudinal eight points over one twist pitch at the center of the simulation model. The magnetic field is evaluated on the reference radius. Contribution of zigzag currents is reflected as periodic magnetic patterns. By taking the average of eight points, contribution of the magnetizations is evaluated as average multipole fields.

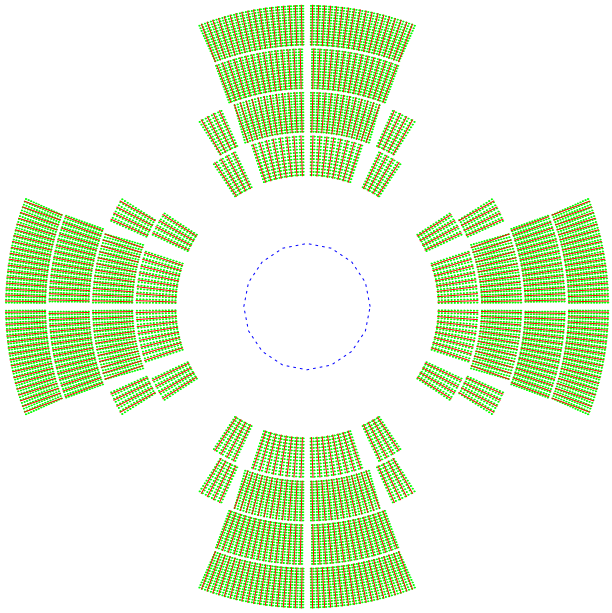

Figure 3.22: Cross sectional view of full coil model. The green dots indicate strand positions where the strand magnetization is computed by cosine theta model. The zigzag current models are arranged into the plane indicated by red lines. The blue dashed line in the bore is the reference radius in which field quality is evaluated.

3.3.2 Results

The result of the step 2, which computes magnetic field on the reference radius induced by the zigzag cable models, are shown in Fig. 3.23. The periodic magnetic patterns were obtained in each multipole. After the current change to a half of the initial one, their amplitudes were reduced by a half of the initial currents.

Next, the magnetizations on the strand position were computed taking account of the history of the excitation. The magnetic field distribution induced by the transport current of 390 A without zigzag currents is shown in Fig. 3.24. The magnetizations were computed with superimposed magnetic field of this field map and field map due to the zigzag currents. An example of the change of the local field distribution induced by zigzag currents within ±20 A to ±10 A is shown in Fig. 3.25. The distribution of random direction of local field change was obtained. Fig. 3.26 indicates the magnetic field vector on a cable at several longitudinal positions. The periodicity of the magnetic field vector can be in the figure.

Finally, the magnetic field is evaluated as multipole field coefficients. Fig. 3.27 indicates the results of the simulation. Generally, only allowed multipole fields, which are b_6 and b_{10} for quadrupole magnet, are induced by superconductor magnetization. However, in the simulation results of the initial multipole fields, non-allowed multipole fields were also induced. The reason is that the initial multipole fields were computed by taking account of the magnetic fields induced by the transport current of 390 A and the initial zigzag currents. Therefore, the magnetization is slightly disturbed by the local field, and induces small non-allowed multipole fields. After the zigzag currents change, any multipole field is induced, because the magnetization directions are rotated due to the local magnetization change. On the other hand, the allowed multipole field, which were induced due to homogeneous magnetization, decrease due to randomization of magnetization directions due to the change of the local magnetic fields.

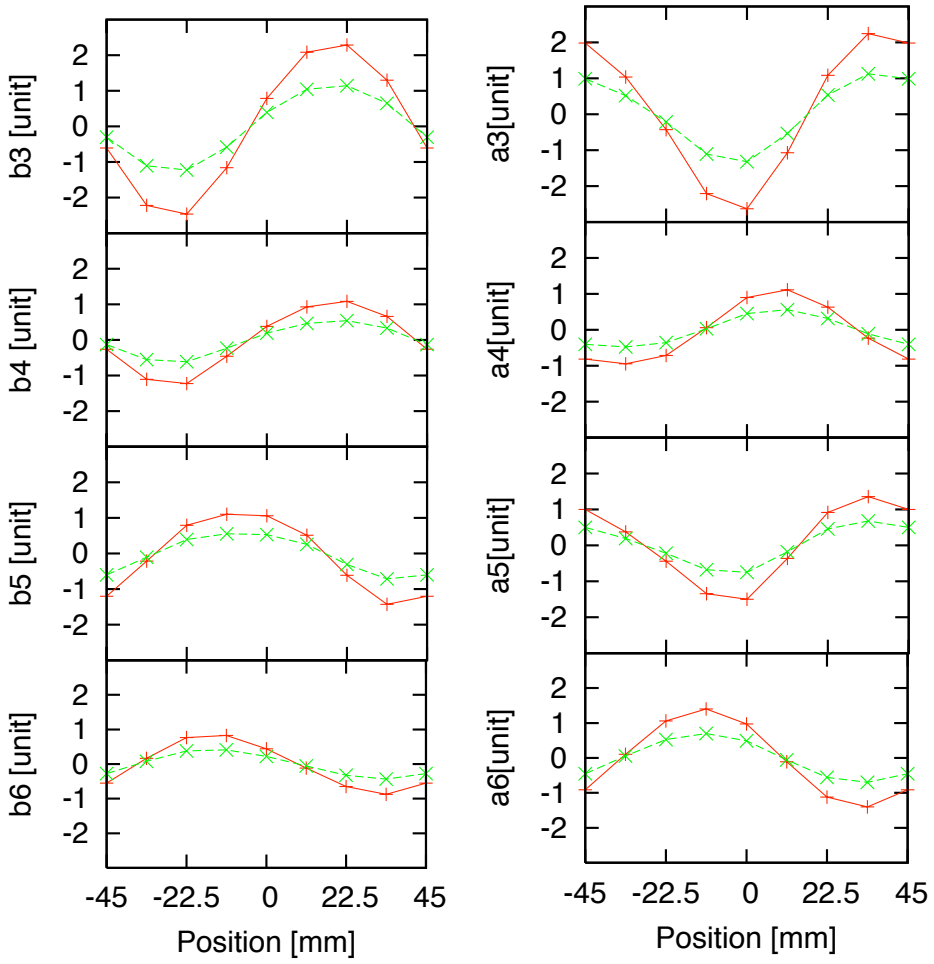

(a) (b)

Figure 3.23: Computed results of magnetic field distribution of (a) normal components, and (b) skew components. The magnetic field distributions induced by the initial currents within ±20 A is depicted by the red lines. The green lines indicate the magnetic field induced by a half of the initial currents.

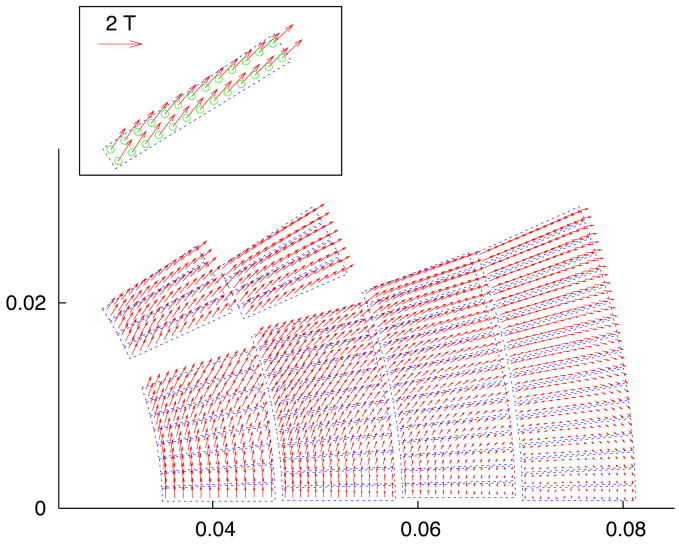

Figure 3.24: Magnetic field distribution induced by the transport current of 390 A without zigzag currents in one octant of the cross section. In the upper left rectangular, the most-pole-side first layer cable and their magnetic field vectors are indicated.

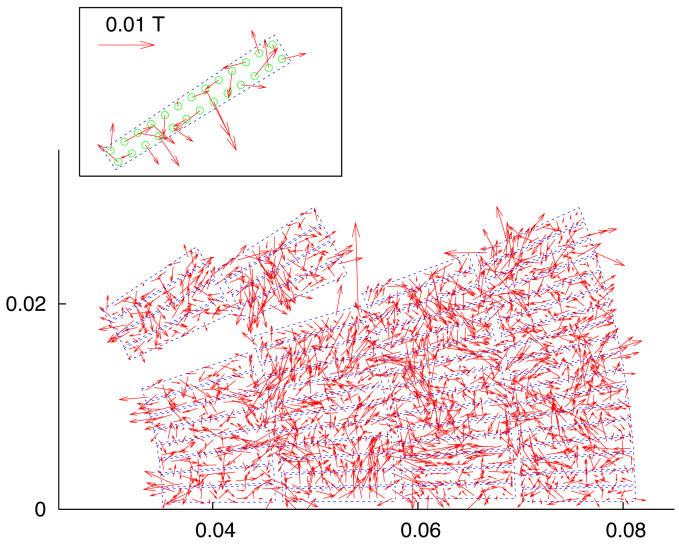

Figure 3.25: An example of local magnetic field change induced by zigzag currents within ±20 A to ±10 A in an octant cross section. In the upper left rectangular, the most-pole-side first layer cable and their magnetic field vectors are also indicated.

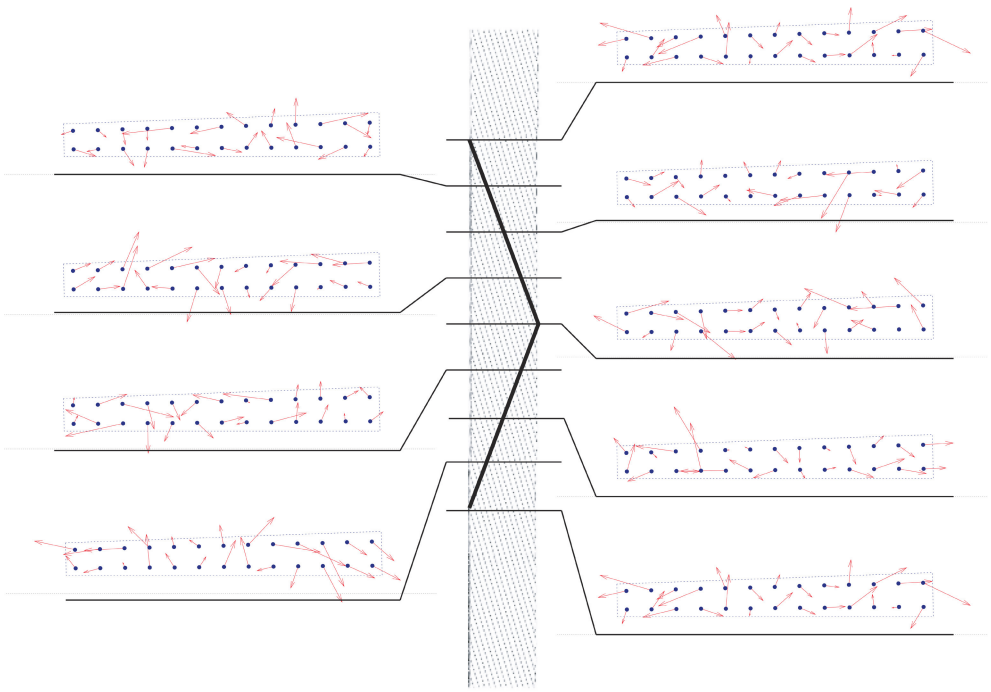

Figure 3.26: Calculation results of local field on the strand in a cable at several longitudinal positions. The highest and lowest positioned cable cross sections indicate almost the same vector distribution. It implies that the magnetic field distribution has periodicity equivalent to the cable twist pitch.

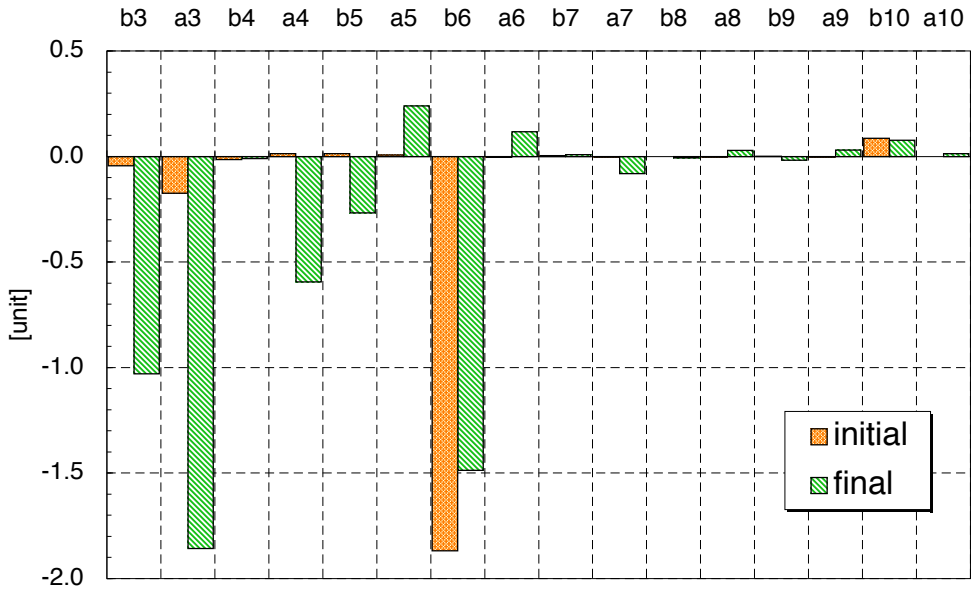

Figure 3.27: The simulated results of magnetic multipole field coefficients in the bore of the magnet.

Chapter 4

Discussions

The periodic magnetic field patterns along the magnet axis were observed in the field measurement of the LHC interaction region quadrupoles. The typical amplitude of these multipole fields is 0.02 to < 0.2 mT corresponding to 1 to < 10 unit at the reference radius of 17 mm, at the beam injection field. The time dependent behavior of the periodic pattern and of the average of multipole field, which is cause of the beam instability at injection, were observed. To evaluate these measured results, a systematic analysis was made with numerical modeling and simulations.

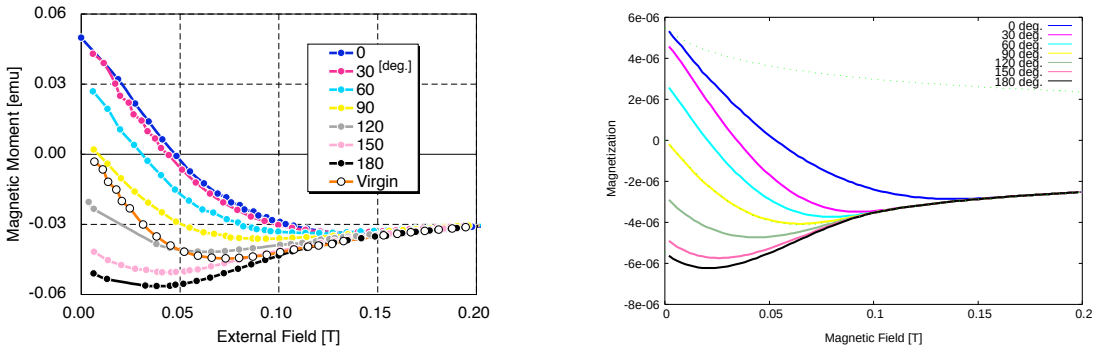

(a) (b)

Figure 4.1: Magnetization curve obtained by (a) the VSM measurement, and (b) the computation of the nested cosine theta model.

First, we discuss the superconductor magnetization in comparison of the measured results by using the VSM with the computation by using the nested cosine theta model originally developed. In the experiment, the superconductor magnetization is saturated by an external magnetic field of 70, 80 mT for the filament diameter of 10 μm. Twice large of the saturation field of 140 mT was needed to have complete change of magne-

Table 4.1: Comparison of Peak Amplitude of Periodic Pattern

	Limited current [A]	Amplitude [mT]	Comment
Experiment	—	0.02	typical value, 1 unit~0.02 mT@r_f
Pair zigzag model	75 (absolute)	0.1	
Cable model	100	0.04	peak of histogram
Single layer model	20	0.04	typical value
Full coil model	20	0.04	typical value

tization direction, as shown in Fig. 4.1(a). In the computation of which the parameters corresponding to the condition of the experiments, the results generally agree with the experimental result, as shown in Fig. 4.1(b).

Based on the understanding of the fundamental magnetization characteristics of the superconductor, we discuss the periodic pattern and their behavior, and average multipole field change by means of the numerical modeling and the simulation. The systematic analyses were made with four step of: (1) a pair of zigzag current model, (2) a cable model, (3) a single layer coil model, and (4) a full (four) layer model.

At first, measured periodic pattern was compared with the numerical calculations by pairs of zigzag currents, as shown in Figs. 4.2(a) and 4.2(b). The calculation generally agrees with the measured result in view of the sinusoidal shape and the pitch of the periodic pattern. It suggest the periodic pattern is caused by imbalance of the currents between strands in the superconducting cable.

The amplitude of the periodic pattern should strongly depend on the distance from the zigzag current, as shown in Fig. 3.11. In the experiment, the pitch of the periodic pattern is consistent with the twist pitch of the inner cable, in contrast with that of outer cable. Therefore, the major contribution of the imbalance currents in inner cable should be naturally understood. The zigzag current of 75 A induces a sinusoidal field with a peak amplitude of 0.1 mT at the reference radius.

As the second step, the superconducting Rutherford cable model was examined with random zigzag current by using Monte Carlo method. The result showed that the random imbalance zigzag current distribution within a range of ±100 A, may induce a magnetic field distribution with a peak of 0.04 mT, as shown in Fig. 3.16.

As the third step, the single layer magnet model was examined. It was verified that the zigzag current could induce periodic magnetic pattern in all multipole components, as shown in Fig. 4.2. The periodic pattern amplitude vary in each computation because of imbalance current randomly given. The comparison of periodic pattern amplitudes are summarized in Table 4.1.

As the last step, a simulation containing full coil configuration with four layer coils

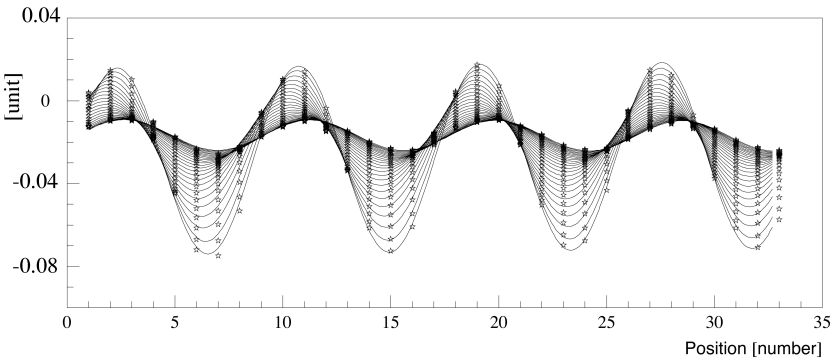

(a)

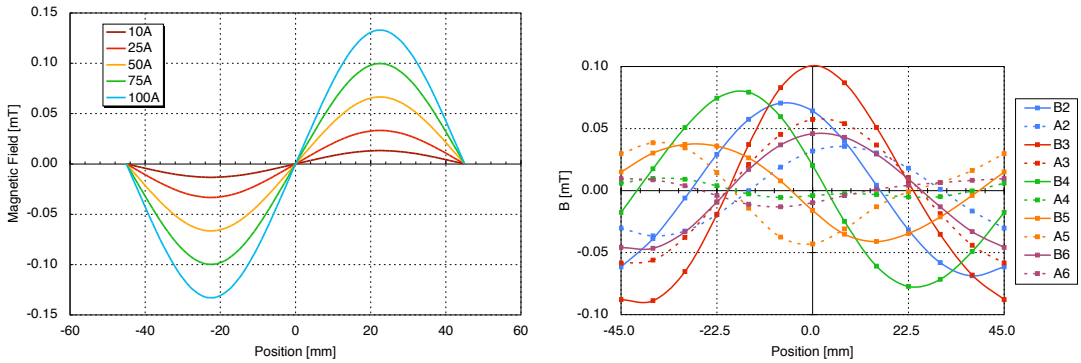

(b) (c)

Figure 4.2: (a) Measured periodic pattern of b_6 component with pre-excitation of 7 kA and 1 hour, (b) calculated periodic pattern by using the pair zigzag current model with various currents, (c) example of calculated periodic pattern by using single layer model. The currents are within ±20 A.

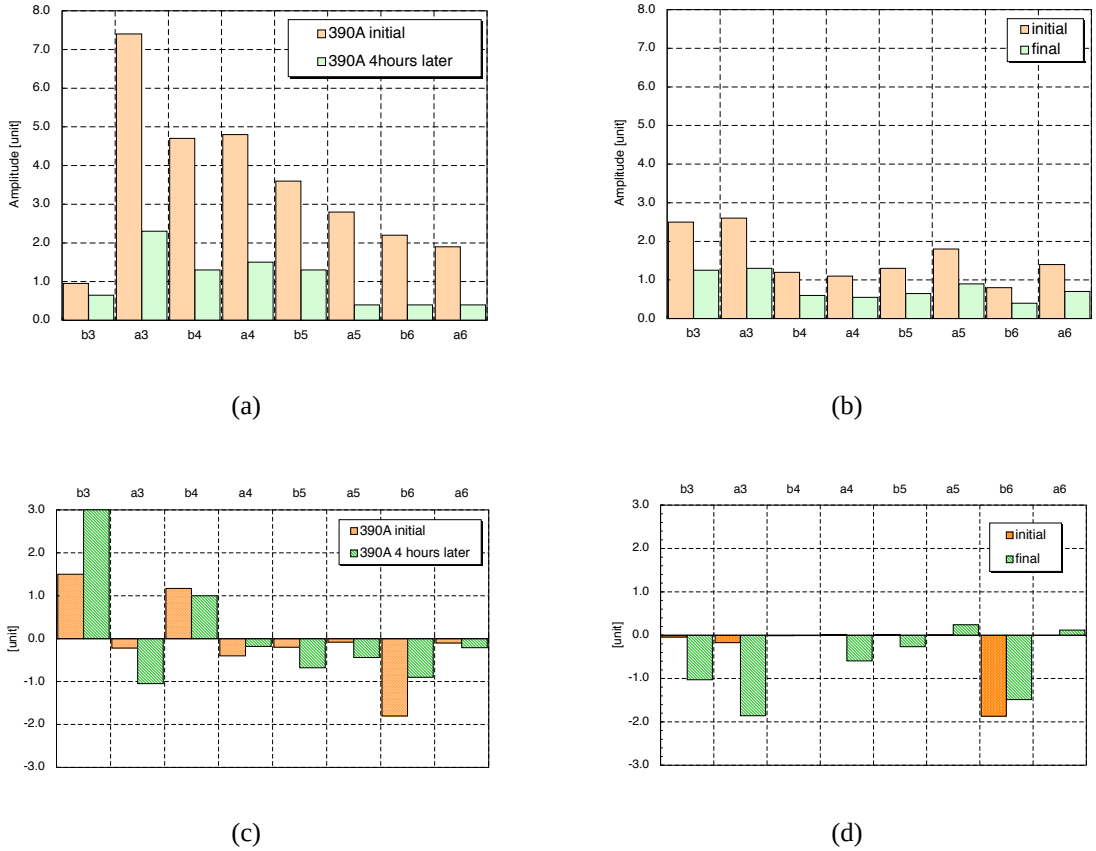

Figure 4.3: Example of amplitudes of periodic patterns obtained by (a) the magnetic field measurement and (b) the numerical simulation, and of average multipole coefficients by (c) the magnetic field measurement and (c) the numerical simulation.

was examined. In this simulation, the change of the superconductor magnetization due to the equalization of the imbalance currents was taken into account by applying nested cosine theta model.

Fig. 4.3(a) shows the measured amplitude of the periodic pattern compared with the full coil simulation of Fig. 4.3(b). The multipole field is also shown in Figs. 4.3(c), 4.3(d). The non-allowed multipoles in the measurement might be induced by random errors of the coil geometry and location. The allowed multipole b_6 could be induced by magnetization of superconductor in either case of the measurement and simulation. In the simulation result, the decrease of the allowed multipoles and the increase of the non-allowed multipoles are obtained after the zigzag current change. The decrease and the increase may be caused by magnetization changes due to local field changes. The simulation results appear in consistency with the measured results.

The different tendency of the 7 kA and 1 hour pre-cycling of correlation between

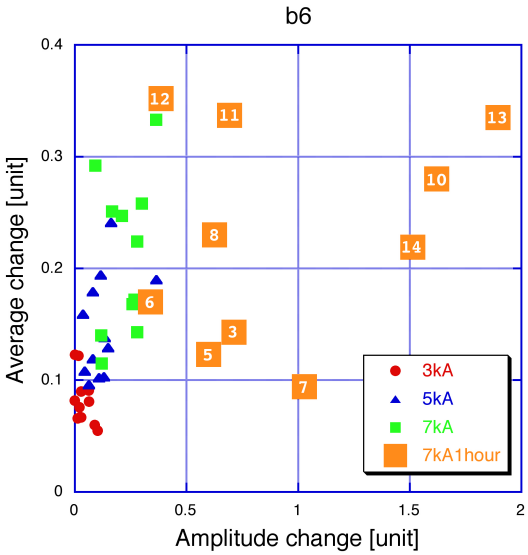

Figure 4.4: Scatter plot of time variations of multipole component and periodic pattern amplitude of b_6.

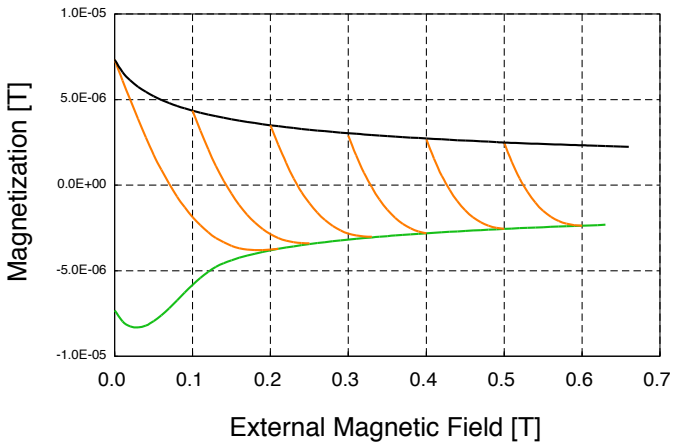

Figure 4.5: Magnetization curve of 10 μm diameter NbTi filament at 1.9 K. From analogy with Fig. 4.1, the vertical axis indicates the magnetization with the direction of external field change. At first, the magnetized superconductor exists between the orange line and green line at each background field. In re-magnetization process, the magnetization moves to the crossing point of the lines on original hysteresis curve of green line. The external magnetic field needed for complete re-magnetization is decreased with background field being increased.

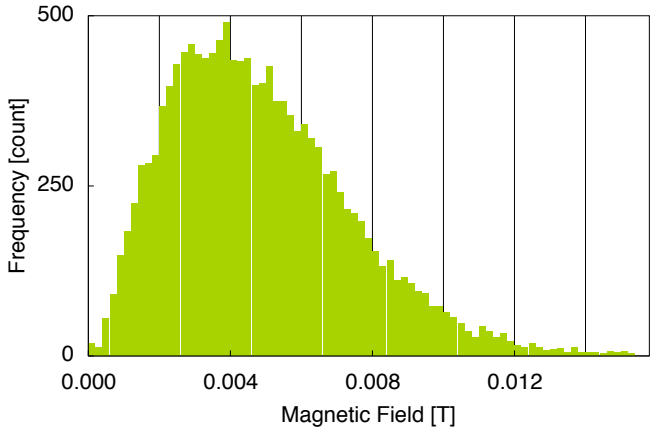

Figure 4.6: Histogram of absolute magnetic fields on strands induced by zigzag currents within ±20 A.

time variations of the multipole field and the periodic pattern was observed, as shown in Fig. 4.4. We discuss here the cause of the tendency based on the re-magnetization mechanism.

Re-magnetization with complete change of the direction is induced by certain external field change corresponding to 140 mT at 4.2 K evaluated by the VSM experiment and the nested cosine theta model. In practical magnet operated at 1.9 K, therefore, the external field change required for complete re-magnetization is 200 mT without background field, as shown in Fig. 4.5. At the beam injection, the magnet is excited by the transport current of 390 A, therefore the superconductor is experienced its own magnetic field e.g. a peak of 420 mT at the most inner pole side region of which contribution to the field quality may be dominant. At the background field, the complete re-magnetization is induced by the external field change of 100 mT, as shown in Fig. 4.5.

In the case of the imbalance current change as limited current change from 20 A to 10 A, the histogram of the absolute value of the local magnetic field change at the strand position is shown in Fig. 4.6. The local magnetic field change distributes with the peak of 4 mT. In order to obtain the change of the local magnetic field with a peak of 100 mT, the limited current change from 500 A to 250 A are estimated by analogy with liner correlation between the current limitation and the peak of histogram.

Therefore, it is thought that the change of the magnetic field is saturated because of the saturation of the re-magnetization due to the imbalance current change beyond the range of the change of the limitation current from 500 A to 250 A.

The simulation with various limited current was performed, and its results is shown in Fig. 4.7. The saturation of the magnetic field quality was clearly obtained. Fig. 4.8 shows conceptual plan of the above discussion about the saturation of average multipole field change. The deviation of the saturation curve above the limited current of 500 A might be due to the distribution of the local magnetic field change with certain width.

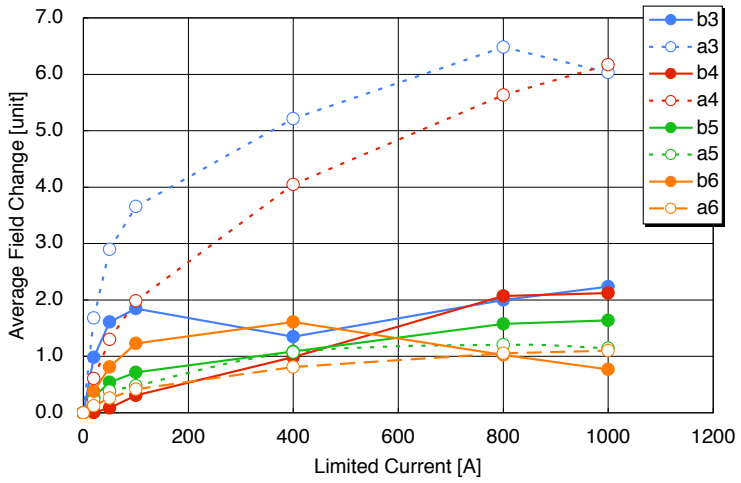

Figure 4.7: Calculated multipole field change vs. limit of initial imbalance current. The currents decrease to a half of the initial currents.

The change of a_3, a_4 components are larger than the other components. In this simulation based on the assumption of the connection of the zigzag current at each coil end, the imbalance current pattern is identical in the each pole. Therefore the behavior the a_3, a_4 might be caused by the assumption, which may cause the difference between poles of the re-magnetization inducing the non-allowed skew components. The time dependent change of the skew multipole field have been observed in the magnetic field measurements[31]. In order to clarify the cause of tendency, the simulation has to be performed statistical number with various condition of imbalance current.

The above discussion, the range of the change imbalance current from 500 A to 250 A was assumed for the saturation of the average multipole field change. It means that the imbalance current change of the range of 250 A is needed substantially. It might induce a few tens unit of the amplitude change of periodic magnetic pattern, however, such amplitude change was not observed. Such large amplitude might decay during the interval of 6, 7 minutes between the end of pre-cycling and the start of the measurement.

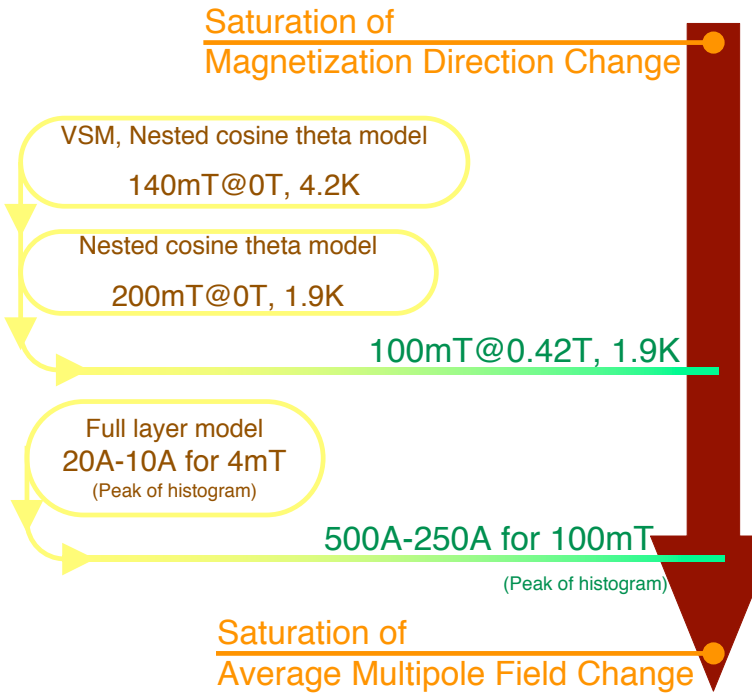

Figure 4.8: Schematic plan of the saturation of the average multipole field change

Chapter 5

Conclusion

The field quality change of superconducting accelerator magnets was investigated. It is a fundamental issue to be solved for beam stability during a beam injection period in the accelerator operation. In order to clarify the mechanism of the magnetic field change, experimental studies and their evaluations with numerical modeling and simulation were carried out.

As the first experiment, the multipole field changes were observed by the magnetic field measurement of superconducting magnets for the LHC beam interaction region quadrupoles developed at KEK. From the systematic measurements, the time-varying periodic pattern along the magnet axis were also observed, and the length of the periodic pattern was well consistent with the twist pitch of the inner coil. It suggested the imbalance of the current of strands in the superconducting cable. A correlation of the time variation was found between the periodic pattern amplitude and the average multipole field.

As the second experiment, the superconducting strand magnetization was measured by using the Vibrating Sample Magnetometer (VSM), in order to understand the fundamental characteristics of magnetization of superconductor filaments. By using the VSM, the re-magnetization was induced by sweeping the magnetic field at various angles to the direction of the sample strand. The results indicate a clear angular dependence.

In analysis of the above experiment, a numerical model for the magnetization of superconductor filament was developed. A nested cosine theta current distribution corresponding to the shielding current was introduced. The magnetization curves with the superconductor filament exposed in arbitrary angles have a good agreement with the results of VSM experiments.

The imbalance current was evaluated to be a level of ±100 A by comparing the measured periodic patterns with the calculated one by using the numerical model originally developed for this work.

The numerical computation was extended to the four layer coil. The magnetic field

induced by imbalance current was computed at reference radius and at each strand location in the coil. The periodic patterns were computed from the magnetic field at the reference radius. The average multipole field induced by magnetization was calculated by using the nested cosine theta model taking into account of the history of the local field during pre-cycling.

The following respects can be described from the experimental studies and their simulations.

1. Imbalance current among strands of a cable of a level of ±100 A is evaluated by numerical simulation comparing with measured periodic pattern.

2. Observed average multipole field change can be explained by re-magnetization due to imbalance current equalization.

3. Large imbalance current change beyond a level of 250 A induces complete re-magnetization which causes the saturation of the average multipole field change.

There is likelihood that the time-varying skew component observed in the measurement is explained by the difference of re-magnetization among poles. In order to verify, it is necessary to perform statistical number of the simulation developed for this work by applying the Monte Carlo method. In order to quantitatively understand the time dependence of the average multipole field change, the imbalance current estimated as a level of a 100 A and their decay time constant has to be verified by additional experimental study e.g. by using short cable sample. Especially for estimation of the time constant of the average multipole change, experimental studies of the soldering part and evaluations of the inductance for the loop of the imbalance currents will be necessary.

Acknowledgements

My studies for this thesis have been supported by many people giving a lot of advice for my work and my private life.

I express thanks to Akira Yamamoto who supervised my work at KEK since my master degree. At the start of my study, my knowledge about the superconducting magnet was built by the seminar at every saturday morning with him. Toru Ogitsu supervised and discussed my Ph.D work in detail. The discussion with him inspired me with many brilliant ideas based on his wealthy experiences and knowledge.

Norihito Ohuchi who developed magnetic field measurement system at KEK advised me to use the system for my work. His great effort for his study by using the system encouraged me to keep the motivation during long way of my Ph.D. Tatsushi Nakamoto supported my work and also my private life during my study at KEK over five years. if I had not been given his encouragement and advice, I could not finished my ph.D work. Takakazu Shintomi accepted my work at the KEK Cryogenics Science Center, and supported. He provided snug environment for my studies.

Technicians at KEK Cryogenics Science Center, Shigekatsu Sugawara, Iida Masahisa, Kenichi Tanaka, and Hirokatsu Ohata greatly supported my experiments of magnetic field measurements which were performed from midnight to early morning. Kiyosumi Tsuchiya and Nobuhiro Kimura are also with KEK Cryogenics Science Center support my studies. Especially on superconductor and cryogenics, I could obtain various knowledge by discussing with the specialists.

Akio Terashima, Norio Higashi, Yasuo Ajima and Hiroshi Kawamata who are with KEK Mechanical Engineering Center, also supported my studies by their specialty on mechanics. I could learn attitude toward construction of practical objects as well as a lot of technic of accelerator magnet building.

Hiroaki Kumakura who is with National Institute for Materials Science (NIMS) provided environment to perform VSM experiment. I express a lot of thanks for his regards.

I am grateful to Sayoko Tanaka, Chie Tanaka, Kazuko Nagai and Emiko Nishihama. They established circumstance for my studies and gave advice for my life during stay at KEK. Takeshi Saiki who is with KEK and the Graduate University for Advanced Studies care about the administration of my student life.

I enjoyed the activity during the student together with Yosuke Iwamoto who was with KEK, and students who are Tetsuhiro Obana, Naohito Fukasawa, Teruyuki Kumasawa, Kenji Matsumoto, Hiroyuki Ohnishi, Masakazu Nozawa, Hidenori Omiya, at KEK. They were necessary for me to continue my studies pleasantly.

I would like to thank Kozi Nakai who brought me to KEK at master degree and opened my studies possibility. Takashi Hashimoto and Shinji Okada, who spent the student life at KEK same as me, supported me. It was very important for me to encourage each other with them.

I express thanks to Thomas Taylor who help my english often and gave me interest of international collaboration.

Finally, I express thanks for many people who contributed to good time in private life. Many friends who have play music together with me gave me peaceful time. My family supported me all of my student life and made effort to provide continuous encouragement. Heartily, I am grateful to «ma moitie», Masako who gave me fruitful nice time and will give it continuously.

Appendix A

Formula for Magnetic Field Calculation

A.1 Equation for magnetic field calculations

Formulae for the magnetic field induced by a line current, as shown in Fig. A.1, are the basic of the computation of the two dimensional magnetic field, e.g. the magnetic field in the bore of the magnet at the straight section. The Maxwell equation for a magnetic field with static current flow in vacuum is

$$\nabla \times \boldsymbol{B} = \mu_0 \, \boldsymbol{j}. \tag{A.1}$$

In order to obtain a magnetic field,

$$\int_s \nabla \times \boldsymbol{B} \cdot \boldsymbol{n} \, ds = \int_s \mu_0 \, \boldsymbol{j} \cdot \boldsymbol{n} \, ds. \tag{A.2}$$

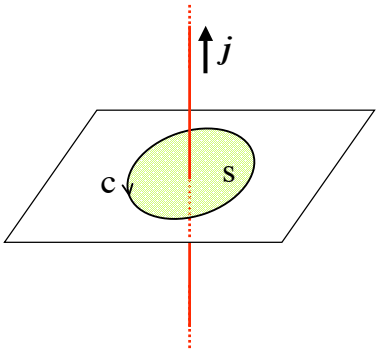

Figure A.1: Schematic view of a line current penetrating a plane surface.

Here, the Stokes theorem $\int_s \nabla \times \boldsymbol{A} \cdot \boldsymbol{n} ds = \oint_c \boldsymbol{A} \cdot d\boldsymbol{l}$ is adopted to left term of (A.2),

$$\oint_c \boldsymbol{B} \cdot d\boldsymbol{l} = \mu_0 \int_s \boldsymbol{j} \cdot \boldsymbol{n}\, ds. \tag{A.3}$$

Then, the integral curve is chosen as a circle with the radius of a, as shown in Fig. A.2(a). The magnetic field component of B_θ is obtained as a function of a and j

$$B_\theta = \frac{\mu_0\, j}{2\pi a} \tag{A.4}$$

In order to adopt to the magnetic field computation, the equation is re-written to complex coordinate system. (B_x, B_y) is described by using B_θ,

$$\begin{aligned} B_x &= -B_\theta \sin\theta, \\ B_y &= B_\theta \cos\theta, \end{aligned}$$

as shown in Fig. A.2(a). In complex coordinate, the magnetic field vector $\boldsymbol{B}$ described as $\boldsymbol{B} = B_y + iB_x$. Therefore,

$$\begin{aligned} \boldsymbol{B} &= B_\theta(\cos\theta - i\sin\theta) \\ &= \frac{\mu_0\, j}{2\pi a}(\cos\theta - i\sin\theta) = \frac{\mu_0\, j}{2\pi a}(\cos\theta + i\sin\theta)^{-1} \\ &= \frac{\mu_0\, j}{2\pi a(\cos\theta + i\sin\theta)} = \frac{\mu_0\, j}{2\pi \boldsymbol{a}}. \end{aligned} \tag{A.5}$$

Here, $\boldsymbol{a}$ is the position of field calculation in the complex coordinate system.

The magnetic field at the arbitrary point $\boldsymbol{z}$ is described as

$$\boldsymbol{B} = \frac{\mu_0 j}{2\pi(\boldsymbol{z} - \boldsymbol{r})}, \tag{A.6}$$

as shown in Fig. A.2(b). (A.6) is the basic formula for magnetic field computation.

The equation of the multipole expansion of a magnetic field due to a line current is introduced as follows.

$$\boldsymbol{B} = \frac{\mu_0 j}{2\pi(\boldsymbol{z} - \boldsymbol{r})} = \frac{\mu_0 j}{2\pi \boldsymbol{r}} \left(\frac{-1}{1 - \dfrac{\boldsymbol{z}}{\boldsymbol{r}}} \right) = -\frac{\mu_0 j}{2\pi \boldsymbol{r}} \sum_{n=1}^{\infty} \left(\frac{\boldsymbol{z}}{\boldsymbol{r}} \right)^{n-1} \tag{A.7}$$

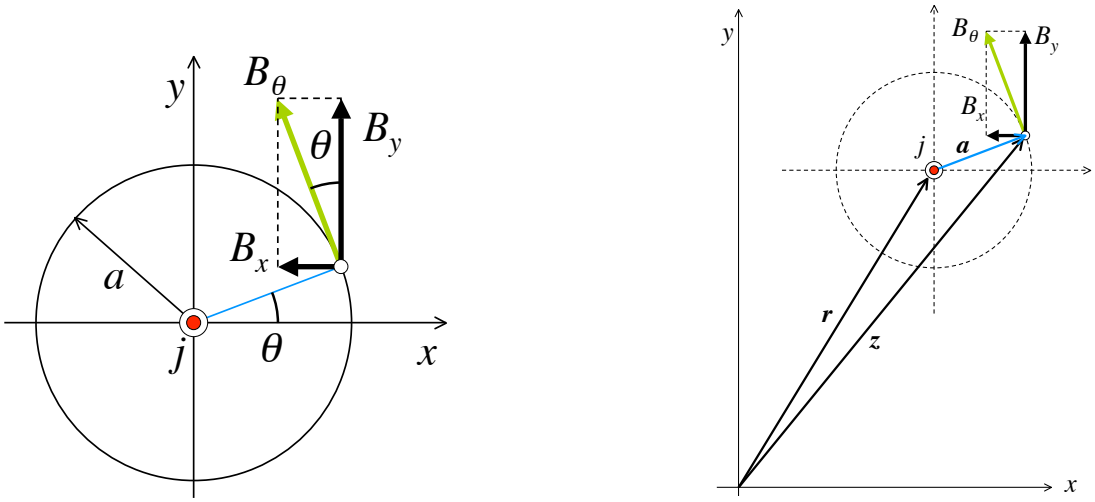

Figure A.2: Magnetic field induced by a line current penetrating at (a) the origin of coordinate, and (b) arbitrary position.

Here, for $x < 1$, $1/(1-a) = \Sigma_{n=1}^{\infty} x^{n-1}$. The multipole field is evaluated at the reference radius r_0 in the bore of the magnet, as shown in Fig. A.3(a).

$$\begin{aligned} \boldsymbol{B} &= -\frac{\mu_0 j}{2\pi \boldsymbol{r}} \sum_{n=1}^{\infty} \left(\frac{r_0}{\boldsymbol{r}}\right)^{n-1} \left(\frac{\boldsymbol{z}}{r_0}\right)^{n-1} = -\frac{\mu_0 j}{2\pi r_0} \sum_{n=1}^{\infty} \left(\frac{r_0}{\boldsymbol{r}}\right)^{n} \left(\frac{\boldsymbol{z}}{r_0}\right)^{n-1} \\ &= -\frac{\mu_0 j}{2\pi r_0} \sum_{n=1}^{\infty} \left(\frac{r_0}{r}\right)^{n} (\cos n\theta - i \sin n\theta) \left(\frac{x+iy}{r_0}\right)^{n-1} \end{aligned} \tag{A.8}$$

The multipole field component induced by the line current is obtained by comparison with,

$$\boldsymbol{B} = B_y + i\, B_x = \sum_{n=1}^{\infty} (B_n + i\, A_n) \left(\frac{x + i\, y}{r_0}\right)^{n-1} . \tag{A.9}$$

Thus, normal and skew component induced by a line current are,

$$\begin{aligned} B_n &= -\frac{\mu_0 j}{2\pi r_0} \left(\frac{r_0}{r}\right)^{n} \cos n\theta, \\ A_n &= \frac{\mu_0 j}{2\pi r_0} \left(\frac{r_0}{r}\right)^{n} \sin n\theta \end{aligned} \tag{A.10}$$

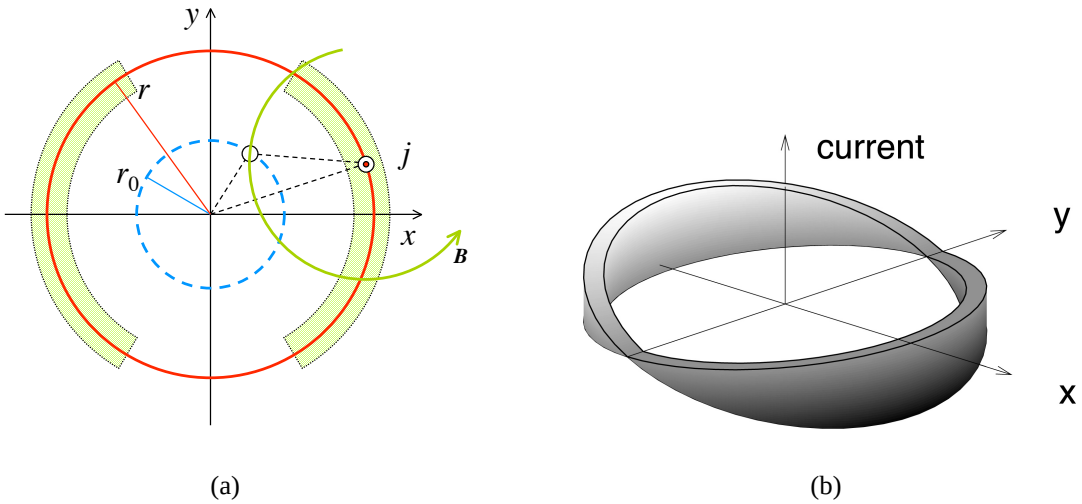

(a) (b)

Figure A.3: (a) Schematic view of the multipole field expansion. The blue dashed line is the reference radius. An example of the typical dipole coil cross section is described as green region with right-left symmetry. (b) Ideal current distribution for pure dipole magnetic field. The current distribution on the red line circle of (a) induces the pure dipole fields in the circle.

As an example of magnetic field calculation, the magnetic field due to ideal current distribution $j = -j_0 \cos\theta$ is described, as shown in Fig. A.3(b).

The current distribution substitute for (A.10).

$$B_n = \frac{\mu_0 j_0}{2\pi r_0}\left(\frac{r_0}{r}\right)^n \cos n\theta \cos\theta. \tag{A.11}$$

Thus, the magnetic field in side the circle of the current region is,

$$B_n = \frac{\mu_0 j_0}{2\pi r_0}\left(\frac{r_0}{r}\right)^n \int_0^{2\pi} \cos n\theta \cos\theta d\theta. \tag{A.12}$$

Here the integral except $n = 1$ is vanished. And also all of the A_n term is vanished. Therefore,

$$B_1 = \frac{\mu_0 j_0}{2\pi r_0}\left(\frac{r_0}{r}\right) \int_0^{2\pi} \cos^2\theta d\theta \tag{A.13}$$

$$= \frac{\mu_0 j_0}{2r}. \tag{A.14}$$

Pure dipole magnetic field is induced.

A.2 Magnetization calculation

The magnetic moment $\boldsymbol{m}$ of a pair line currents, as shown in Fig. A.4(a) is defined as,

$$\boldsymbol{m} = 2x \cdot I \cdot l_f. \tag{A.15}$$

Here $2x$ is distance between the current pair, I is current, and l_f is the line current length. The magnetic moment induced by an elementary area of the filament cross section, as shown in Fig. A.4(b), is

$$d\boldsymbol{m}_f = 2x \cdot j \cdot l_f \cdot dxdy. \tag{A.16}$$

Here j is the current density in the area.

The magnetic moment of a fully penetrated filament with the critical current density j_c, based on the Bean model and calculated using polar coordinate is,

$$\boldsymbol{m}_f = 2 \cdot j_c \cdot l_f \int_{-\frac{\pi}{2}}^{\frac{\pi}{2}} \int_0^{r_f} r^2 \cos\theta d\theta dr \tag{A.17}$$

$$= \frac{4}{3} {r_f}^3 \cdot j_c \cdot l_f. \tag{A.18}$$

Here r_f is filament radius. Total current is

$$I_f = \frac{\pi}{2} r_f^2 \cdot j_c. \tag{A.19}$$

The magnetic moment of the filament can be replaced by the magnetic moment of a current pair of same currents separated by an effective distance,

$$d_f = \frac{\frac{4}{3} r_f^3 \cdot j_c \cdot l_f}{\frac{\pi}{2} r_f^2 \cdot j_c \cdot l_f}$$

$$= \frac{8}{3\pi} r_f, \tag{A.20}$$

as shown in Fig. A.4. The magnetic moment induced by full penetrated of a filament is

$$\boldsymbol{m}_f = d_f \cdot I_f \cdot l_f. \tag{A.21}$$

This magnetization induces the magnetic field in the magnet bore. The magnetic field is calculated by using the line current pair. From (A.6), the line currents per unit length induce the magnetic field $\boldsymbol{B}$,

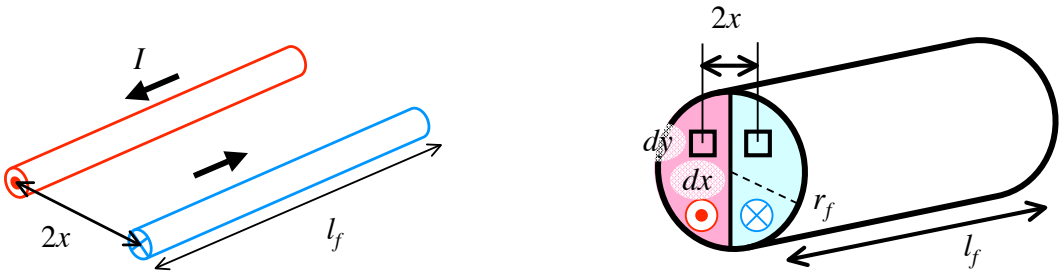

(a) (b)

Figure A.4: Schematic view of: (a) a current pair, (b) fully penetrated filament magnetization based on the Bean model.

$$\boldsymbol{B} = \frac{\mu_0 I_f}{2\pi\left(\boldsymbol{z} - \boldsymbol{r} + \frac{\boldsymbol{d}_f}{2}\right)} + \frac{-\mu_0 I_f}{2\pi\left(\boldsymbol{z} - \boldsymbol{r} - \frac{\boldsymbol{d}_f}{2}\right)}. \tag{A.22}$$

Here, $\boldsymbol{d}_f$ is the vector from the position of $-I$ to that of I, $\boldsymbol{r}$ is the center of the two currents lines. Then, $d_f \ll r$,

$$\begin{aligned}\boldsymbol{B} &= \frac{\mu_0 I_f}{2\pi}\sum_{n=1}^{\infty} n\frac{\boldsymbol{d}_f}{\boldsymbol{r}^{n+1}}\boldsymbol{z}^{n-1} \\ &= \frac{\mu_0}{2\pi}\sum_{n=1}^{\infty} n I_f \boldsymbol{d}_f \left(\frac{e^{-(n+1)i\theta}}{r^2}\right)\left(\frac{r_0}{r}\right)^{n-1}\left(\frac{x+iy}{r_0}\right)^{n-1}.\end{aligned} \tag{A.23}$$

Here the definition of the x and y components of the magnetization that is magnetic moment per unit volume are

$$\begin{aligned}\boldsymbol{M} &= (M_x, M_y) \\ &= \left(\mathrm{M}\cos\left(\alpha - \frac{\pi}{2}\right), \mathrm{M}\sin\left(\alpha - \frac{\pi}{2}\right)\right) \\ &= (\mathrm{M}\sin\alpha, -\mathrm{M}\cos\alpha)\,.\end{aligned} \tag{A.24}$$

Here, α is angle of the $\boldsymbol{d}_f$, as shown in Fig. A.5(b). Therefore, the $I_f\boldsymbol{d}_f$ is

$$I_f\boldsymbol{d}_f = \pi r_f^2 \mathrm{M}\,(\cos\alpha + i\sin\alpha) = \pi r_f^2(-M_y + iM_x). \tag{A.25}$$

Thus, (A.23) is

$$\boldsymbol{B} = \frac{\mu_0}{2\pi} \sum_{n=1}^{\infty} n\pi r_f^2 (-M_y + iM_x) \frac{e^{-(n+1)i\theta}}{r^2} \left(\frac{r_0}{r}\right)^{n-1} \left(\frac{x+iy}{r_0}\right)^{n-1}. \tag{A.26}$$

From the above equation and (A.9), the multipole field induced by magnetization (M_x, M_y) positioned at (r, θ) is

$$B_n = \frac{n\mu_0}{2\pi r^2} \cdot \pi r_f^2 (-M_y \cos(n+1)\theta + M_x \sin(n+1)\theta) \left(\frac{r_0}{r}\right)^{n-1}, \tag{A.27}$$

$$A_n = \frac{n\mu_0}{2\pi r^2} \cdot \pi r_f^2 (\, M_x \cos(n+1)\theta + M_y \sin(n+1)\theta) \left(\frac{r_0}{r}\right)^{n-1}. \tag{A.28}$$

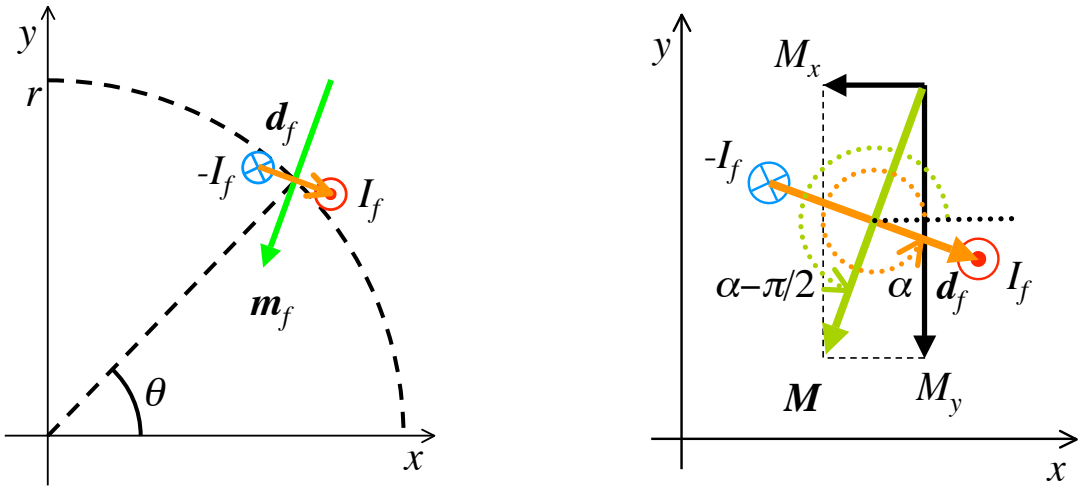

(a) (b)

Figure A.5: Schematic view of the magnetization Definition of x, and y components of magnetization.

Nomenclature

Roman Letters

a	radius component of polar coordinate	m
A_n	skew 2n-pole component	$T/m^{(n-1)}$
a_n	coefficient of skew magnetic field	unit
a_n^{amp}	amplitude of periodic pattern of skew component	unit
a_n^{ave}	average of periodic pattern of skew component	unit
a_n^{lin}	linear coefficient of skew component	unit
$\boldsymbol{B}$	magnetic field vector	T
B	magnetic field	T
B_{ext}	external magnetic field	T
$\boldsymbol{B}_{ext}^{ini}$	initial external field vector	T
$\boldsymbol{B}_{ext}^{mod}$	external magnetic field after change	T
B_k^{main}	main magnetic field of 2(n-1)-pole magnet	$T/m^{(n-1)}$
$B[n]$	absolute (shielding) internal magnetic field by n-th shell	T
B_n	normal 2n-pole component	$T/m^{(n-1)}$
b_n	coefficient of normal magnetic field	unit
$\boldsymbol{B}[n]$	(shielding) internal magnetic field by n-th shell	T
b_n^{amp}	amplitude of periodic pattern of normal component	unit
b_n^{ave}	average of periodic pattern of normal component	unit
B_n^{ini}	effective external magnetic field for n-th shell	T
$\boldsymbol{B}[n]^{ini}$	initial (shielding) internal magnetic field by n-th shell	T
b_n^{lin}	linear coefficient of normal component	unit

$\boldsymbol{B}[n]^{mod}$	modified (shielding) internal magnetic field by *n*-th shell	T
B_x	*x* component of magnetic field vector	T
B_y	*y* component of magnetic field vector	T
dB/dt	time change of magnetic field	T/s
$\boldsymbol{d}_f$	effective distance vector of two line currents assigned as magnetization	m
h	distance from current element to field computation point	m
I	current	A
i	imaginary unit	
j	current density	A/m^2
jc	critical current density	A/m^2
k	integer number	
l_f	filament length	m
$\boldsymbol{M}$	magnetization	T
$\boldsymbol{m}$	magnetic moment	Wb · m
m_f	absolute value magnetic moment of filament	Wb · m
m_n	absolute value to magnetic moment of *n*-th shell	Wb · m
M_x	*x* component of magnetization	T
m_{xn}	x-component of magnetic moment of *n*-th shell	Wb · m
M_y	*y* component of magnetization	T
m_{yn}	y-component of magnetic moment of *n*-th shell	Wb · m
N	number of division	
n	order of multipole field	
B_n^{feel}	magnetic field for *n*-th shell	T
r_0	reference radius	m
r_f	filament radius	m
r_n	inner radius of *n*-th shell	m
t	time	s
x	*x* component of position	m
y	*y* component of position	m
$\boldsymbol{r}$	position vector of line current	m
$\boldsymbol{z}$	position vector	m

Greek Letters

α	angle of $\boldsymbol{d}_f$	radian
δ	phase of periodic pattern	radian
δ_0	angle of change of external magnetic field	radian
Δa_n^{amp}	amplitude change of periodic pattern of skew component	unit
Δa_n^{ave}	average change of skew component	unit
ΔB_{ext}	absolute value of change of external magnetic field	T
$\boldsymbol{\Delta B}_{ext}$	change of external magnetic field	T
Δb_n^{amp}	amplitude change of periodic pattern of normal component	unit
Δb_n^{ave}	average change of normal component	unit
Δt	thickness of shell	m
λ	wave length of periodic pattern	m
μ_0	magnetic permeability of vacuum	H/m
π	circular constant	
φ	angle component of polar coordinate	radian
θ	angle	radian
ψ	angle of external field	radian

List of Figures

List of Tables

Bibliography

[1] K. H. Mess, P. Schmüser, and S. Wolff, *Superconducting accelerator magnets*. World Scientific Publishing Co. Pte. Ltd., 1996.

[2] K. Sugita, T. Ogitsu, T. Nakamoto, N. Ohuchi, H. Hirano, T. Shintomi, K. Tsuchiya, and A. Yamamoto, "Analytical calculation of field error due to radial coil distortions of the LHC low-beta quadrupole magnets," *IEEE Trans. Appl. Supercond.*, vol. 12, pp. 1693–1696, Mar. 2002. MT-17.

[3] L. Bottura, "A practical fit for the critical surface of NbTi," *IEEE Trans. Appl. Supercond.*, vol. 10, pp. 1054–1057, Mar 2000. MT-16.

[4] Y. B. Kim, C. F. Hempstead, and A. R. strnad, "Critical persistent currents in hard superconductors," *Phys. Rev. Letters*, vol. 9, pp. 306–309, Oct. 1962.

[5] P. W. Anderson, "Theory of flux creep in hard superconductors," *Phys. Rev. Letters*, vol. 9, pp. 309–311, Oct. 1962.

[6] D. A. Finley, D. A. Edwards, R. W. Hanft, R. Johnson, A. D. McInturff, and J. Strait, "Time dependent chromaticity changes in the tevatron," in *Proceedings of the 1987 IEEE particle accelerator conference*, vol. 1, pp. 151–153, Mar. 1987. PAC87.

[7] M. Halemeyer, P. Schmüser, H. Brück, D. Gall, J. Krzywinski, R. Meinke, and H. Preißner, "A new method for determining the magnetization of superconducting cables and its time dependence," *IEEE Trans. Appl. Supercond.*, vol. 3, pp. 168–171, MARCH 1993. ASC92.

[8] H. Brück, D. Gall, G. Knies, J. Krzywinski, R. Lange, R. Meinke, H. Preißner, P. Schmüser, and Y. Zhao, "Time dependence of persistent-current field distortions in the superconducting HERA magnets," in *Proceedings of 2nd European Particle Accelerator Conference*, no. 1, pp. 329–331, 1990. EPAC90.

[9] D. A. Herrup, M. J. Syphers, D. Johnson, R. P. Johnson, A. V. Tollestrup, R. W. Hanft, B. C. Brown, M. J. Lamm, M. Kuchnir, and A. D. McInturff,

"Time variations of fields in superconducting magnets and their effect on accelerators," *IEEE Tran. Mag.*, vol. 25, pp. 1643–1646, Mar. 1989. ASC88.

[10] A. Devred, J. DiMarco, J. Kuzminski, R. Stiening, J. Tompkins, Y. Yu, H. Zheng, T. Ogitsu, R. Hanft, P. Mazur, D. Orris, and T. Peterson, "Time decay measurement of the sextupole component of the magnetic field in a 4-cm aperture, 17-m-long SSC dipole magnet prototype," in *Conference record of the 1991 IEEE particle accelerator conference*, vol. 4, pp. 2480–2482, May 1991. PAC91.

[11] L. Bottura, L. Walckiers, and R. Wolf, "Field error decay and snap-back in LHC model dipoles," *IEEE Trans. Appl. Supercond.*, vol. 7, pp. 602–605, Jun. 1997. ASC96.

[12] R. W. Hanft, B. C. Brown, D. A. Herrup, M. J. Lamm, A. D. McInturff, and M. J. Syphers, "Studies of time dependence of fields in tevatron superconducting dipole magnets," *IEEE Tran. Mag.*, vol. 25, pp. 1647–1651, Mar 1989. ASC88.

[13] H. Brück, Z. Jiao, D. Gall, G. Knies, J. Krzywinski, R. Meinke, H. Preißner, and P. Schmüser, "Time dependence of persistent current effects in the superconducting HERA magnets," in *Proceedings of the 11th international conference on magnet technology*, vol. 1, pp. 329–331, 1989. MT-11.

[14] H. Brück, D. Gall, J. Krzywinski, R. Meinke, H. Preißner, M. Halemeyer, P. Schmüser, C. Stolzenburg, R. Stiening, D. ter Avest, and L. van de Klundert, "Observation of a periodic pattern in the persistent-current fields of the superconducting HERA magnets," in *Conference record of the 1991 IEEE particle accelerator conference*, vol. 4, pp. 2149–2151, May 1991. PAC91.

[15] A. P. Verweij, *Electrodynamics of superconducting cables in accelerator magnets*. PhD thesis, Twente University, 1995.

[16] R. Stiening, "A possible mechanism for enhanced persistent current sextupole decay in SSC dipoles," Tech. Rep. SSCL-359, SSC, Jan. 1991.

[17] R. Wolf, "The decay of the field integral in superconducting accelerator magnets wound with Rutherford cables," in *Proceedings of fifteenth international conference on magnet technology*, no. 1, pp. 238–241, 1998. MT-15.

[18] M. Haverkamp, A. Kuijper, A. den Ouden, B. ten Haken, L. Bottura, and H. H. ten Kate, "Interaction between current imbalance and magnetization in LHC cables," *IEEE Trans. Appl. Supercond.*, vol. 11, pp. 1609–1612, Mar. 2001. ASC2000.

[19] M. Haverkamp, B. ten Haken, L. Bottura, and H. ten Kate, "Penetration of an external field change with arbitrary angle into a saturated superconducting filament," *Physica C*, vol. 372-376, pp. 1356–1359, 2002. EUCAS01.

[20] M. Haverkamp, L. Bottura, E. Benedico, S. Sanfilippo, B. ten Haken, and H. H. J. ten Kate, "Field decay and snapback measurements using a fast hall plate detector," *IEEE Trans. Appl. Supercond.*, vol. 12, pp. 86–89, Mar. 2002. MT-17.

[21] M. Haverkamp, L. Bottura, and M. Schneider, "Studies of decay and snapback effect in LHC dipole magnets," in *EUCAS'99*, 1999. EUCAS99.

[22] M. Haverkamp, *Decay and snapback in superconducting accelerator magnets*. PhD thesis, Twente University, 2003.

[23] T. Pieloni, S. Sanfilippo, L. Bottura, M. Haverkamp, A. Tikhov, E. Effinger, E. Benedico, and N. Smirnov, "Field decay and snapback measurements using a fast hall probe sensor," *IEEE Trans. Appl. Supercond.*, vol. 14 to be published, 2004. MT-18.

[24] N. Ohuchi, K. Tsuchiya, T. Ogitsu, Y. Ajima, M. Qiu, A. Yamamoto, and T. Shintomi, "Magnetic field measurements of a 1-m long model quadrupole magnet for the LHC interaction region," *IEEE Trans. Appl. Supercond.*, vol. 9, pp. 451–454, Jun. 1999. ASC98.

[25] N. Ohuchi, Y. Ajima, M. Qiu, T. Nakamoto, T. Ogitsu, T. Shintomi, K. Tsuchiya, and A. Yamamoto, "Field quality of two 1-m model magnets for LHC low-β quadrupole magnets," *IEEE Trans. Appl. Supercond.*, vol. 10, pp. 139–142, Mar. 2000. MT-16.

[26] N. Ohuchi, Y. Ajima, T. Nakamoto, T. Ogitsu, M. Qiu, R. Ruber, T. Shintomi, K. Tsuchiya, and A. Yamamoto, "Field measurements of 1-m model quadrupole magnets for the LHC-IR," in *Proceedings of EPAC2000*, (`http://accelconf.web.cern.ch/accelconf/e00/PAPERS/MOP3B12.pdf`), pp. 373–375, Jun. 2000. EPAC2000.

[27] N. Ohuchi, Y. Ajima, H. Hirano, T. Nakamoto, T. Ogitsu, T. Shintomi, K. Tsuchiya, and A. Yamamoto, "Field quality of the LHC-IR 1-m model quadrupole magnets developed at KEK," in *Proceedings of the 18th International conference on high energy accelerators*, (`HEACC2001: http://conference.kek.jp/heacc2001/pdf/p2hc02.pdf`), p. non, 2001. HEACC2001.

[28] N. Ohuchi, H. Hirano, Y. Ajima, T. Nakamoto, T. Ogitsu, N. Kimura, T. Shintomi, K. Tsuchiya, and A. Yamamoto, "Magnetic field measurements of the prototype LHC-IR MQXA at 1.9 k," *IEEE Trans. Appl. Supercond.*, vol. 12, pp. 188–191, Mar. 2002. MT-17.

[29] N. Ohuchi, H. Hirano, Y. Ajima, T. Ogitsu, T. Nakamoto, N. Kimura, M. Iida, H. Ohhata, S. Sugawara, K. Tsuchiya, A. Yamamoto, and T. Shintomi, "Field quality of the low-beta quadrupole magnets, MQXA, for the LHC-IR," in *Proceedings of EPAC 2002*, (`http://epaper.kek.jp/e02/PAPERS/MOPLE010.pdf`), pp. 2418–2420, 2002. EPAC2002.

[30] N. Ohuchi *et al.*, "Status of LHC low-beta quadrupole magnets, MQXA, at KEK," in *Proceedings of the 2003 Particle Accelerator Conference*, (`http://epaper.kek.jp/p03/PAPERS/WPAE019.PDF`), pp. 1978–1980, 2003. PAC03.

[31] N. Ohuchi, Y. Ajima, T. Nakamoto, T. Ogitsu, T. Shintomi, K. Sugita, K. Tsuchiya, and A. Yamamoto, "Magnetic field characteristics of the low-beta quadrupole magnets, MQXA for LHC," *IEEE Trans. Appl. Supercond.*, vol. 14 to be published, 2004. MT-18.

[32] N. Ohuchi, Y. Ajima, T. Nakamoto, T. Ogitsu, T. Shintomi, K. Tsuchiya, and A. Yamamoto, "Magnetic field measurements of the LHC-IR MQXA magnets at room temperature," *IEEE Trans. Appl. Supercond.*, vol. 14 to be published, 2004. MT-18.

[33] C. P. Bean, "Magnetization of hard superconductors," *Phys. Rev. Letters*, vol. 8, pp. 250–253, Mar. 1962.

[34] M. N. Wilson, *Superconducting magnets*. Oxford Science Publications, 1983.

[35] C. Völlinger, *Superconductor magnetization modeling for the numerical calculation of field errors in accelerator magnets*. PhD thesis, Technical University of Berlin, 2002.

[36] S. Amet, L. Bottura, V. Granata, S. L. Naour, R. K. Mishra, L. Oberli, D. Richter, S. Sanfilippo, A. Verweij, L. Walckiers, and R. Wolf, "Persistent and coupling current effect in the LHC superconducting dipoles," *IEEE Trans. Appl. Supercond.*, vol. 13, pp. 1239–1242, Jun. 2003. ASC02.

[37] R. Bossert, J. S. Kerby, F. Nobrega, M. J. Lamm, J. Rife, S. Feher, W. Robotham, P. Schlabach, S. Yadav, and A. B. Zlobin, "Construction experience with MQXB quadrupole magnets built at Fermilab for the LHC interaction regions," *IEEE Trans. Appl. Supercond.*, vol. 13, pp. 1297–1300, Jun. 2003. ASC02.

[38] R. Bossert *et al.*, "Field measurement of Fermilab-built quadrupole magnets for the LHC interaction regions," *IEEE Trans. Appl. Supercond.*, vol. 13, pp. 1243–1245, Jun. 2003. ASC02.

[39] L. Bottura, L. Walckiers, and Z. Ang, "Experimental evidence of boundary induced coupling currents in LHC prototypes," *IEEE Trans. Appl. Supercond.*, vol. 7, pp. 801–804, Jun. 1997. ASC96.

[40] L. Bottura, L. Larsson, S. Schloss, M. Schneider, N. Smirnov, and M. Haverkamp, "A fast sextupole probe for snapback measurement in the LHC dipoles," *IEEE Trans. Appl. Supercond.*, vol. 10, pp. 1435–1438, Mar. 2000. MT-16.

[41] L. Bottura, M. Breschi, and M. Schneider, "Measurement of magnetic field pattern in a short LHC dipole model," *IEEE Trans. Appl. Supercond.*, vol. 11, pp. 1605–1608, Mar. 2001. ASC2000.

[42] J. Buckley, D. Richter, L. Walckiers, and R. Wolf, "Dynamic magnetic measurement of superconducting magnets for the LHC," *IEEE Trans. Appl. Supercond.*, vol. 5, pp. 1024–1027, Jun. 1995. ASC94.

[43] E. Burkhardt, A. Yamamoto, T. Nakamoto, T. Shintomi, and K. Tsuchiya, "Quench protection heater studies for the 1-m model magnets for the LHC low-β quadrupoles," *IEEE Trans. Appl. Supercond.*, vol. 10, pp. 681–684, Mar. 2000. MT-16.

[44] E. Burkhardt, A. Yamamoto, T. Nakamoto, T. Ogitsu, T. Shintomi, and K. Tsuchiya, "Quench protection heater studies of the 3rd 1-m model magnet for the KEK-LHC low-β quadrupoles," *IEEE Trans. Appl. Supercond.*, vol. 11, pp. 1621–1624, Mar. 2001. ASC2000.

[45] W. V. Delsolaro, L. Bottura, M. Haverkamp, and A. Kuijper, "Degaussing and decay reduction in the short superconducting dipole models for the LHC," *IEEE Trans. Appl. Supercond.*, vol. 12, pp. 291–294, Mar. 2002. MT-17.

[46] A. K. Ghosh, K. E. Robins, and W. B. Sampson, "The ramp rate dependence of the sextupole field in superconducting dipoles," *IEEE Tran. Mag.*, vol. 30, pp. 1718–1721, Jul. 1994. MT-13.

[47] J. S. Kerby, "Production status of the LHC inner triplet magnet system," *IEEE Trans. Appl. Supercond.*, vol. 13, pp. 1229–1232, Jun. 2003. ASC02.

[48] M. Lamm, M. bleadon, K. Coulter, S. Delchamps, R. Hanft, T. Jaffery, W. Kinney, W. Koska, J. Ozelis, J. Strait, M. Wake, and J. DiMarco, "Magnetic field measurements of 1.5 meter model SSC collider dipole magnets at Fermilab," *IEEE Tran. Mag.*, vol. 28, pp. 133–136, Jan. 1992. MT-12.

[49] S. L. Naour, L. Oberli, R. Wolf, R. Puzniak, A. Wisniewski, H. Fikis, M. Foitl, and H. Kirchmayr, "Magnetization measurement on LHC superconducting strands," *IEEE Trans. Appl. Supercond.*, vol. 9, pp. 1763–1766, Jun. 1999. ASC98.

[50] T. Nakamoto, K. Tanaka, A. Yamamoto, K. Tsuchiya, E. Burkhardt, N. Higashi, N. Kimura, T. Ogitsu, N. Ohuchi, K. Sasaki, T. Shintomi, A. Terashima, G. Kirby, R. Ostojic, and T. Taylor, "Quench and mechanical behavior of an LHC low-β quadrupole model," *IEEE Trans. Appl. Supercond.*, vol. 9, pp. 697–700, Jun. 1999. ASC98.

[51] T. Nakamoto, A. Yamamoto, K. Tsuchiya, Y. Ajima, E. Burkhardt, T. Haruyama, N. Higashi, M. Iida, N. Kimura, T. Ogitsu, H. Ohhata, N. Ohuchi, T. Shintomi, K. Tanaka, and A. Terashima, "Training characteristics of 1-m model magnets for the LHC low-β quadrupoles," *IEEE Trans. Appl. Supercond.*, vol. 10, pp. 143–146, Mar. 2000. MT-16.

[52] T. Nakamoto, A. Yamamoto, K. Tsuchiya, E. Burkhardt, N. Higashi, N. Kimura, T. Ogitsu, N. Ohuchi, T. Shintomi, and A. Terashima, "Quench performance and mechanical behavior of 1 m model magnet for the LHC low-beta quadrupoles at KEK," *IEEE Trans. Appl. Supercond.*, vol. 11, pp. 1637–1640, Mar. 2001. ASC2000.

[53] T. Nakamoto, E. Burkhardt, T. Ogitsu, A. Yamamoto, T. Shintomi, and K. Tsuchiya, "Quench protection study of a prototype for the LHC low-beta quadrupole magnets," *IEEE Trans. Appl. Supercond.*, vol. 12, pp. 170–173, Mar 2002. MT-17.

[54] T. Nakamoto *et al.*, "Fabrication and mechanical behavior of a prototype for the LHC low-beta quadrupole magnets," *IEEE Trans. Appl. Supercond.*, vol. 12, pp. 174–178, Mar 2002. MT-17.

[55] T. Nakamoto *et al.*, "Production and performance of the LHC interaction region quadrupoles at KEK," *IEEE Trans. Appl. Supercond.*, vol. 13, pp. 1321–1324, Jun. 2003. ASC02.

[56] T. Ogitsu and otners, "Status of the LHC low-beta insertion quadrupole magnet development at KEK," *IEEE Trans. Appl. Supercond.*, vol. 12, pp. 183–187, Mar. 2002. MT-17.

[57] P. Pugnat, T. Schreiner, and A. Siemko, "Investigation of the periodic magnetic field modulation in LHC superconducting dipoles," *IEEE Trans. Appl. Supercond.*, vol. 12, pp. 258–261, Mar. 2002. MT-17.

[58] M. Qiu, N. Ohuchi, K. Tsuchiya, T. Nakamoto, T. Shintomi, T. Ogitsu, Y. Ajima, and A. Yamamoto, "Magnetic field error analysis of a low-β quadrupole magnet," *IEEE Trans. Appl. Supercond.*, vol. 12, pp. 215–218, Mar 2002. MT-17.

[59] W. Sampson and A. Ghosh, "Induced axial oscillations in superconducting dipole windings," *IEEE Trans. Appl. Supercond.*, vol. 5, pp. 1036–1039, Jun. 1995. ASC94.

[60] T. Shintomi *et al.*, "Progress of LHC low-β quadrupole magnets at KEK," *IEEE Trans. Appl. Supercond.*, vol. 11, pp. 1562–1565, Mar. 2001. ASC2000.

[61] K. Sugita, T. Ogitsu, T. Nakamoto, N. Ohuchi, T. Shintomi, K. Tsuchiya, and A. Yamamoto, "Time dependence of magnetic periodic patterns measured on the MQXA magnets for the LHC-IR," *IEEE Trans. Appl. Supercond.*, vol. 13, pp. 1317–1320, Jun. 2003. ASC02.

[62] K. Sugita, T. Ogitsu, N. Ohuchi, T. Nakamoto, T. Shintomi, K. Tsuchiya, and A. Yamamoto, "Study of time dependent magnetic field variation due to current redistribution in Rutherford cable," *IEEE Trans. Appl. Supercond.*, vol. 14 to be published, 2004. MT-18.

[63] K. Tsuchiya, T. Nakamoto, A. Yamamoto, T. Ogitsu, N. Ohuchi, M. Qiu, and T. Shintomi, "Magnetic design of a low-β quadrupole magnet for the LHC interaction regions," *IEEE Trans. Appl. Supercond.*, vol. 10, pp. 135–138, Mar. 2000. MT-16.

[64] C. Völlinger, M. Aleksa, and S. Russenschuck, "Compensation of magnetization effects in superconducting accelerator magnets," *IEEE Trans. Appl. Supercond.*, vol. 12, pp. 1492–1495, Mar. 2002. MT-17.

[65] M. N. Wilson, "Superconducting magnets for accelerator: a review," *IEEE Trans. Appl. Supercond.*, vol. 7, pp. 727–732, Jun. 1997. ASC96.

[66] A. Yamamoto, K. Tsuchiya, N. Higashi, T. Nakamoto, T. Ogitsu, N. Ohuchi, T. Shintomi, A. Terashima, G. Kirby, R. Ostojic, and T. M. Taylor, "Design study of a superconducting insertion quadrupole magnet for the large hadron collider," *IEEE Trans. Appl. Supercond.*, vol. 7, pp. 747–750, Jun. 1997. ASC96.

[67] A. Yamamoto, T. Nakamoto, K. Tsuchiya, K. Tanaka, H. Yamaoka, A. Terashima, N. Higashi, T. Ogitsu, N. Ohuchi, and T. Shintomi, "Analysis of mechanical tolerances of a low-β quadrupole magnet for the LHC," *IEEE Trans. Appl. Supercond.*, vol. 10, pp. 131–134, Mar. 2000. MT-16.

[68] H. Brück, D. Gall, J. Krzywinski, R. Lange, R. Meinke, H. Preißner, P. Schmüser, and Y. Zhao, "Persistent current effects in the superconducting HERA magnets and correction coils," 1990?

[69] H. Hirano, Y. Ajima, T. Nakamoto, T. Ogitsu, N. Ohuchi, T. Shintomi, K. Tsuchiya, and A. Yamamoto, "Measurements of magnetic axis and twist of a low-beta quadrupole magnet for LHC by using a morgan coil," in *Proceedings of EPAC 2002*, (`http://epaper.kek.jp/e02/PAPERS/MOPLE011.pdf`), pp. 2400–2402, 2002. EPAC2002.

[70] G. Kirby *et al.*, "Mechanical design and characteristics of a superconducting insertion quadrupole model magnet for the large hadron collider," in *Proceedings of fifteenth international conference on magnet technology*, no. 1, pp. 63–66, 1998. MT-15.

[71] T. Nakamoto *et al.*, "Quench and mechanical performance of 1-m model magnets for the LHC low beta quadrupoles," in *Proceedings of the 18th International conference on high energy accelerators*, (`HEACC2001: http://conference.kek.jp/heacc2001/pdf/p2hc01.pdf`), p. non, 2001. HEACC2001.

[72] P. Pugnat, T. Schreiner, and A. Siemko, "Investigation of the periodic magnetic field modulation inside apertures of LHC superconducting dipole models," in *Proceedings of EPAC2000*, (`http://accelconf.web.cern.ch/accelconf/e00/PAPERS/THP2A03.pdf`), pp. 2151–2153, 2001. EPAC2000.

[73] W. B. Sampson, A. K. Ghosh, and K. E. Robins, "Axial oscillations in the magnetic field of superconducting accelerator magnets," in *Presentation of high field accelerator magnet workshop*, p. non, Mar. 1993. High field accelerator magnet workshop.

[74] K. Tsuchiya, R. J. M. Y. Ruber, T. Nakamoto, T. Ogitsu, N. Ohuchi, M. Qiu, T. Shintomi, A. Terashima, and A. Yamamoto, "Field analysis of LHC insertion quadrupole model magnets at KEK," in *Proceedings of EPAC2000*, (`http://accelconf.web.cern.ch/accelconf/e00/PAPERS/THP1A19.pdf`), pp. 2175–2177, Jun. 2000. EPAC2000.

[75] A. Yamamoto *et al.*, "Development and test results of a low-β quadrupole model for the large hadron collider," in *Proceedings of the 6th European Particle Accelerator Conference*, (`http://epaper.kek.jp/e98/PAPERS/TUP20G.PDF`), pp. 2047–2049, 1998. EPAC98.

[76] A. Yamamoto *et al.*, "Development of a superconducting insertion quadrupole model magnet for the large hadron collider," in *Proceedings of fifteenth international conference on magnet technology*, no. 1, pp. 59–62, 1998. MT-15.

[77] A. Yamamoto *et al.*, "Development of LHC low-β quadrupole magnets at KEK," in *Proceedings of the 2001 Particle Accelerator Conference*, vol. 5, pp. 3633–3635, Jun. 2001. PAC01.

[78] E. Badea, "Numerical calculation of the magnetic field produced by currents circulating though two opposite strands of a Rutherford-type cable," Tech. Rep. MD-TA-262, SSC, Aug. 1993.

[79] H. Brück, R. Meinke, F. Muller, and P. Schmüser, "Field distortions from persistent currents in the superconducting HERA magnets," Tech. Rep. DESY HERA 89-041, DESY, Mar. 1989.

[80] H. Brück, D. Gall, J. Krzywinski, R. Meinke, H. Preißner, A. Freter, M. Halemeyer, P. Schmüser, R. Stiening, D. ter Avest, and L. van de Klundert, "Observation of a periodic pattern in the persistent-current field of the superconducting HERA dipole magnets," Tech. Rep. DESY HERA 91-01, DESY, Jan. 1991.

[81] H. Brück, D. Gall, J. Krzywinski, R. Meinke, H. Preißner, M. Halemeyer, P. Schmüser, C. Stolzenburg, R. Stiening, D. ter Avest, and L. van de Klundert, "Observation of a periodic pattern in the persistent-current field of the superconducting HERA magnets," Tech. Rep. DESY HERA 91-11, DESY, Jul. 1991.

[82] M. Haverkamp, E. Benedico, L. Bottura, G. Deferne, M. Gateau, P. Pugnat, S. Sanfilippo, and T. Schreiner, "Fast sextupole measurement for chromaticity corrections in the LHC," Tech. Rep. LHC-MTA-IN-2001-161, CERN, May 2001.

[83] D. A. Herrup, "Compensation of time-dependent persistent current effect in the tevatron," Tech. Rep. FERMILAB-FN-602, Fermilab, Apr. 1993.

[84] R. Meinke and P. S. Y. Zhao, "Method of harmonics measurements in the superconducting HERA magnets and analysis of systematic errors," Tech. Rep. DESY HERA 91-13, DESY, Sep. 1991.

[85] G. Morgan, "A comparison of two analytic forms for the jc(b,t) surface," Tech. Rep. SSC-MD-218, SSC, Jan. 1989.

[86] M. Pekeler, P. Schmüser, C. Stolzenburg, Z. Yuping, H. Brück, P. D. Gall, and R. Meinke, "Coupled persistent-current effects in the HERA dipoles and beam pipe correction coils," Tech. Rep. DESY HERA 92-06, DESY, April 1992.

[87] M. Wake, T. Jaffery, and M. J. Lamm, "Periodic remnant field in SSC 50 mm dipole," Tech. Rep. TS-SSC-91-32, SSC, Feb. 1991.

[88] M. Wake, T. Jaffery, and M. J. Lamm, "Periodic field in SSC 40 mm dipole and its temperature gradient effect," Tech. Rep. TS-SSC-91-41, SSC, Mar. 1991.

[89] T. Ogitsu, *Influence of cable eddy currents on the magnetic field of superconducting particle accelerator magnets*. PhD thesis, Tsukuba University, 1990.